Dipl.-Ing. Indira Kopacic, BSc

New Lead-Free Germanium Halide Perovskite Materials for Solar Cells: Synthesis, Improved Performance and Stability

DOCTORAL THESIS

To achieve the university degree of

Doktor der technischen Wissenschaften

submitted to

Graz University of Technology

Supervisor

Univ.-Prof. Dipl.-Ing. Dr.techn. Gregor Trimmel

Institute for Chemistry and Technology of Materials

Graz, December 2020

AFFIDATIV / EIDESSTATTLICHE ERKLÄRUNG

I declare that I have authored this thesis independently, that I have not used other than the declared sources/resources, and that I have explicitly indicated all material which has been quoted either literally or by content from the sources used. The text document uploaded to TUGRAZonline is identical to the present doctoral thesis.

Ich erkläre an Eides statt, dass ich die vorliegende Arbeit selbstständig verfasst, andere als die angegebenen Quellen/Hilfsmittel nicht benutzt, und die den benutzten Quellen wörtlich und inhaltlich entnommenen Stellen als solche kenntlich gemacht habe. Das in TUGRAZonline hochgeladene Textdokument ist mit der vorliegenden Dissertation identisch.

_____ _____

Date / Datum Signature / Unterschrift

To my Family

(Picture from: http://green4uproject.eu/de/glossar/)

Remember to look up at the stars and not down at your feet.

Try to make sense to what you see and wonder about what makes the universe exist.

Be curious. And however difficult life may seem, there is always something you can do and succeed at.

It matters that you don't just give up!

(Stephen Hawking)

ACKNOWLEDGEMENTS

Mein größter Dank gilt meiner Familie, die mir die Möglichkeit gab, ein Chemiestudium zu beginnen - insbesondere meinen Eltern und Schwestern, die immer die richtigen Worte fanden und stets an meinen Erfolg glaubten.

Zuletzt möchte ich mich bei meinem Ehemann Samir für all die Liebe und Fürsorge, die er mir gegeben hat, bedanken. Du warst in den gesamten vergangenen zehn Jahren für mich da, halfst mir, mich zu entwickeln und begleitetes mich durch viele verrückte Wege und Ideen. Auch unserem kleinen Sonnenschein Sara ein großes Dankeschön. Mit deinen zwei Jahren zeigst du Mama und Papa jeden Tag aufs Neue, wie relativ die Sorgen des Laboralltags doch sind. Sara, ich liebe dich wie nichts anderes auf der Welt.

ABSTRACT

Perovskite solar cells have received increased attention in recent years. In addition to being easily and cheaply manufactured, they also show extremely good power conversion efficiencies. Germanium-based perovskite materials have good optoelectronic properties and are structurally very similar to the best-known lead- and tin-based perovskite materials. The slight oxidation of Ge^{2+} to Ge^{4+} is a major disadvantage and enormously affects reproducibility. So far, only low efficiencies (<1%) of germanium perovskite solar cells have been achieved, which is significantly lower compared to lead (>22%) and tin-based (>10%). Nevertheless, germanium has great potential to replace the toxic lead in perovskite solar cells. Therefore, this work deals with the production of new germanium perovskite solar cells as well as their optimization and stabilization in order to improve their performance. The solar cells were built in a p-i-n architecture (glass/indium tin oxide/poly(3,4-ethylenedioxythiophene):poly(styrenesulfonate) (PEDOT:PSS)/germanium -based perovskite/[6,6]-phenyl-C_{71}-butyric acid methyl ester ($PC_{70}BM$))/Ag), whereby PEDOT: PSS were used as hole and $PC_{70}BM$ as electron transport layers. The biggest challenge to overcome was the quick and easy oxidation of germanium, as well as the thermal degradation of germanium perovskite, which negatively affects the performance of the solar cell. In addition, a solvent had to be found in which GeI_2 dissolves well and the perovskite forms best using the "antisolvent" method. Pure N, N-dimethylformamide (DMF) best dissolved the GeI_2 and the methylammonium iodide (MAI) and also formed the most homogeneous layers. Germanium perovskites have not only disadvantages with regard to easy oxidation, they are also highly sensitive to water, which makes reproducibility of the manufacturing process of germanium perovskite solar cells significantly more difficult. The germanium perovskite forms through a very rapid crystallization, but this had to be stabilized in order not to disintegrate in the glovebox after a few hours. Therefore, by modifying the chemical composition of the germanium perovskite by introducing bromide ions into the methylammonium germanium iodide perovskite ($MAGeI_3$), the solar cell performance was significantly improved, as was the stability of the germanium perovskite. By replacing 10% of the iodide with bromide, performance efficiencies of up to 0.57% were achieved in $MAGeI_{2.7}Br_{0.3}$-based solar cells. In addition, it was found that the PEA^+-cation had a positive influence on the germanium perovskite. The newly manufactured, low-dimensional germanium halide perovskite with

mixed cation PEAxMA$_{(1-x)}$GeI$_2$Br, showed very good solar cell performance with good stability and a lifespan of over 20 days from a PEAI concentration of 40 - 50%. In addition, the use of an LED lamp confirmed that germanium perovskites (MAGeI$_2$Br) are very sensitive to temperature and light.

KURZFASSUNG

Perowskit-Solarzellen haben in den vergangenen Jahren immer mehr an Aufmerksamkeit gewonnen. Neben ihrer günstigen und leichten Herstellung zeigen sie äußerst gute Wirkungsgrade. Germanium-basierte Perowskitmaterialien besitzen gute optoelektronische Eigenschaften und ähneln strukturell sehr den bekanntesten blei- und zinnbasierten Perowskitmaterialien. Die leichte Oxidation von Ge^{2+} zu Ge^{4+} stellt einen großen Nachteil dar und beeinträchtigt die Reproduzierbarkeit enorm. Daher konnten bis jetzt nur geringe Effizienzen (<1%) von Germanium-Perowskit-Solarzellen erreicht werden, was im Vergleich zu blei- (>22%) und zinnbasierten (>10%) deutlich niedriger ist. Trotzdem besitzt Germanium großes Potential, das giftige Blei in Perowskitsolarzellen zu ersetzen. Daher beschäftigt sich diese Arbeit mit der Herstellung neuer Germanium-Perowskit-Solarzellen und mit deren Optimierung und Stabilisierung, um diese auch in ihrer Leistung zu verbessern. Die Solarzellen wurden in einer p-i-n Architektur (Glas/ Indiumzinnoxid/ Poly(3,4-ethylenedioxythiophen):Poly(styrenesulfonat) (PEDOT:PSS) / Germanium-basierter Perowskit/ [6,6]-Phenyl-C71-butansäuremethylester($PC_{70}BM$)/ Ag) gebaut, wobei PEDOT:PSS als Loch- und $PC_{70}BM$ als Elektronentransportleiter verwendet wurden. Die größte Herausforderung stellte die schnelle und einfache Oxidation von Germanium dar, ebenso wie die thermische Degradation von Germanium-Perowskiten, wodurch die Leistung der Solarzelle negativ beeinträchtigt wurde. Zudem musste ein Lösungsmittel gefunden werden, in dem sich GeI_2 gut löst und sich der Perowskit durch die Anti-Lösungsmitteln Methode am besten bildet. N,N-Dimethylformamid (DMF) löste das GeI_2 und das Methylammoniumiodid (MAI) am besten und bildete auch die homogensten Schichten. Germanium-Perowskite zeigen nicht nur Nachteile in der leichten Oxidation, sie besitzen auch eine hohe Empfindlichkeit gegenüber Wasser, wodurch eine Reproduzierbarkeit des Herstellungsprozesses von Germanium-Perowskit-Solarzellen deutlich erschwert wird. Der Germanium-Perowskit bildete sich durch eine sehr rasche Kristallisation aus, jedoch musste dieser stabilisiert werden, um nicht gleich nach einigen Stunden in der Glovebox zu zerfallen. Das Modifizieren der chemischen Zusammensetzung des Germanium-Perowskits und das Einführen von Bromidionen in den Methylammoniumgermaniumiodid-Perowskit ($MAGeI_3$) führten zu einer signifikanten Verbesserung der Solarzellenleistung sowie zu einer Verbesserung der Stabilität des Germanium-Perowskits. Durch Ersetzen von 10% des Iodids durch Bromid wurden Wirkungsgrade von bis zu 0.57% in Solarzellen auf $MAGeI_{2.7}Br_{0.3}$-

Basis erzielt. Darüber hinaus wurde festgestellt, dass das PEA$^+$-Kation einen positiven Einfluss auf den Germanium-Perowskiten hat. Das neu hergestellte, niedrigdimensionale Germaniumhalogenid-Perowskit mit gemischtem Kation PEA$_x$MA$_{(1-x)}$GeI$_2$Br, zeigte ab einer PEA$^+$-Konzentration von 40 - 50% sehr gute Solarzellenleistung mit guter Stabilität und einer Lebensdauer von über zwanzig Tagen. Darüber hinaus bestätigte die Verwendung einer LED-Lampe, dass Germaniumperowskite (MAGeI$_2$Br) sehr sensitiv gegenüber Temperatur und Licht sind.

ABBREVIATIONS

AS   anti-solvent

CB   chlorobenzene

DMF   N, N – dimethyl fromamide

DMSO   dimethyl sulfoxide

DSSC   dye sensitized solar cell

Eg   band gap energy

ETL   electron transport layer

EQE   external quantum efficiency

FAI   formamidinium iodide

FF   fill factor

FIB   focused ion beam

FTO   fluorine doped tin oxide

GBL γ-butyrolactone

HOMO   highest occupied molecular orbital

HP   heating plate

HTL   hole transport layer

I_{MPP} current at maximum power point

I_{SC} short circuit current

ITO   indium doped tin oxide

IV   current-voltage

J_{MPP} current density at maximum power point

J_{SC} short circuit current density

JV	current density-voltage
LUMO	lowest unoccupied molecular orbital
MAI	methyl ammonium iodide
MPP	maximum power point
PC60BM	[6,6]-phenyl-C61-butyric acid methyl ester
PC70BM	[6,6]-Phenyl-C71-butyric acid methyl ester
PCE	power conversion efficiency
PEAI	phenylethyl ammonium iodide
PEDOT:PSS	Poly(3,4-ethylenedioxythiophene)-poly(styrenesulfonate)
PMMA	poly(methyl methacrylate)
P_{max}	maximum power output
PSC	perovskite solar cell
PV	photovoltaic
RT	room temperature
SC	spin coating
SEM	scanning electron microscope
Spiro-MeOTAD	2,2',7,7'-Tetrakis[N,N-di(4-methoxyphenyl)amino]-9,9'-spirobifluorene
Vmpp	voltage at maximum power point
VB	valence band
V_{OC}	open circuit voltage
XRD	X-ray diffracti

CONTENTS

1 INTRODUCTION

Water, heat and electricity are basic needs and as such should be available to every consumer. Although these are basic needs, their price is rising rapidly, causing poorer people in particular to suffer. Therefore, resources are conserved wherever possible, not only because of the costs, but also to care for the environment. Nevertheless, electricity consumption can not be minimized. One of the main reasons for this is digitization. Nowadays everybody wants to use a smartphone, laptop, tablet or television, and want to be connected to the internet anytime and anywhere. It is also common electrical household appliances (electric toothbrush, kitchen appliances, iron, vacuum cleaner...) that make everyday life easier for a modern person and are therefore indispensable. Forecasts show that in the near future there will be more and more of these devices (e.g. Alexa, digital refrigerators, smart homes etc...) that easily slip into our lives and that in the long term greatly increase electricity consumption. The switch to electric vehicles goes hand in hand with an increased demand for electricity. However, due to their higher degree of efficiency, these are significantly more energy-efficient than vehicles with internal combustion engines. As a prerequisite for e-mobility to be climate-friendly, the electricity required for it should come from green electricity systems. (e.g. photovoltaics). Fossil fuel is the main source of electrical energy today and it consumes a lot of carbon dioxide, which exacerbates global warming. The sun is the most important and most natural source of energy on earth. It offers inexhaustible energy to humans. Using solar cells, devices that directly convert solar energy into electricity, would therefore most likely stop the energy crisis and global warming. Perovskite solar cells are the greatest hope today in photovoltaics. They are considered a promising alternative to replace the silicon solar cells most used in photovoltaic systems.

Therefore, this chapter describes the great importance of renewable energies, specifically photovoltaics and their latest innovations, perovskite solar cells. In particular, the basics of perovskite solar cells, as well as their structure and functionality are discussed. In addition, the importance of lead-free perovskite solar cells is explained, which constitutes the motivation and importance of this work.

1.1 Motivation

1.1.1 Global Warming Challenge

Global warming describes the increase in the average temperature of the near-earth atmosphere and seas since the beginning of industrialization. This has been systematically measured and recorded since 1880 (see *Figure 1*).
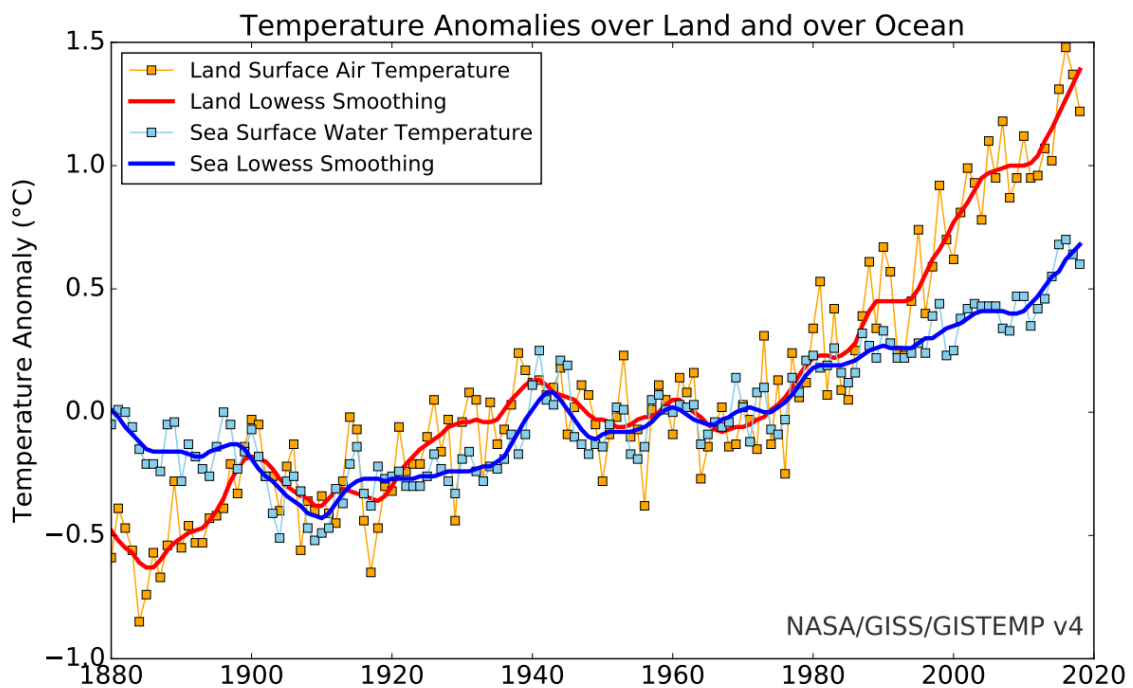
Figure 1. Change in global surface temperature over land (red line) and sea surface temperature (blue line) 1880-2019.[1] Copyright (2020)

This average has increased by 0.74 degrees since the end of the 19th century. According to scientific forecasts, this value should increase by a further 1.8 to 4 degrees by the year 2100. Such an increase would lead to rapid and great transformation, with the climate changing more than in the past 10 000 years. [2,3] The reasons for such rapid climate change are primarily industrialization, ever increasing amounts of oil, gas and coal being burned, deforestation, and the negative affects on the climate caused by agriculture. Our behavior releases and enriches more and more greenhouse gases, especially carbon dioxide (CO_2), methane and nitrous oxide in the earth's atmosphere. Such gases absorb part of the infrared heat radiation emitted by the ground and thus prevent it from escaping into space. Human activities amplify these gases, especially carbon dioxide, and thus destabilize the

natural equilibrium. There is also a clear correlation between global warming and carbon dioxide emissions (see *Figure 2*).[4,56]
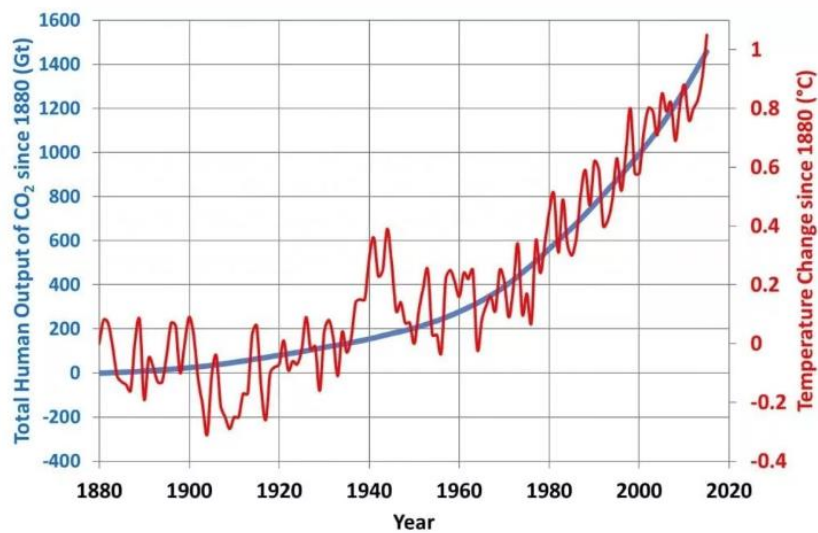
Figure 2. Blue curve: Total emissions of carbon dioxide since 1880 (source, Oak Ridge Laboratory) Red curve: Temperature change since 1880 (source, NASA).[7] Copyright (2019)

To stop global warming, each of us would have to fundamentally change our lifestyle. Therefore, in December 2015, at the United Nations Climate Change Conference, almost all countries in the world decided that the average temperature should not rise by more than 1.5 to 2 °C. To reach the target of 1.5 °C, greenhouse gases worldwide would have to be reduced to zero by 2060. At the same time, part of the previously emitted carbon dioxide would also have to be removed from the earth's atmosphere through carbon dioxide removal. The direct emission of carbon dioxide, in particular by AFOLU (Agriculture, Forestry and Other Land Use), transport, industry, and electricaly and heat production (see *Figure 3*) must be reduced urgently. In order to achieve the goal, each country must make its own contribution. It would also be of great importance to switch to more renewable energies, such as photovoltaics, wind and hydropower.[6]
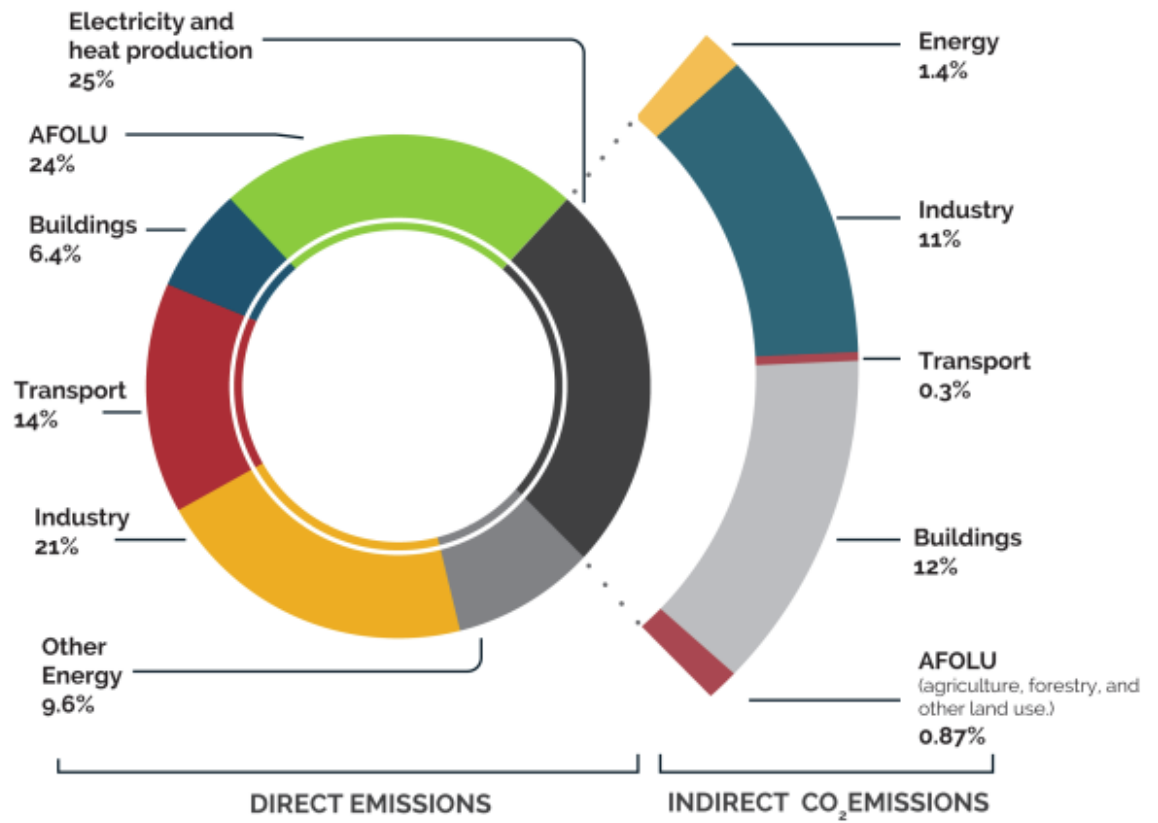
Figure 3. Direct and indirect CO_2 emissions.[8] Copyright (2020)

1.1.2 Global Energy Demand and Renewable Resources

In the 19th century, global energy demand rose rapidly due to the second industrial revolution. At the same time, natural resources are being exploited more and more. Fossil fuels are highly efficient, can be extracted relatively cheaply and converted into energy, which makes them particularly attractive. However, fossil fuels will be exhausted within the next 200 years and they also pollute the environment. The energy demand, on the other hand, is steadily increasing due to globalization, advancing industrialization and the growth of the world population. Global energy production more than doubled in the period from 1971 to 2009 (see **Figure *4***).
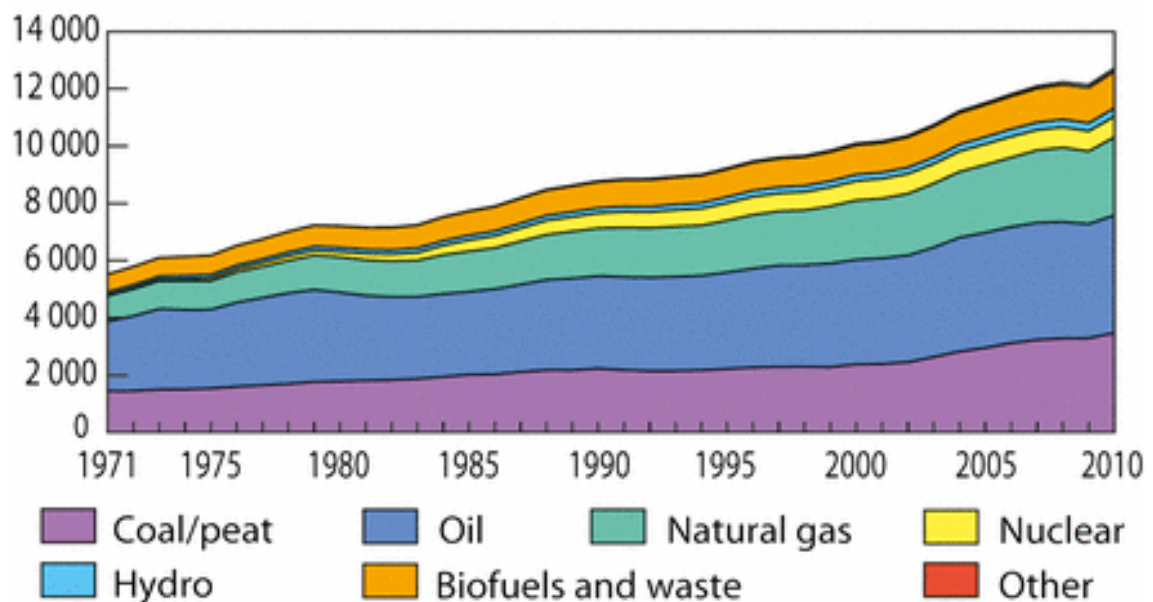
Figure 4. World's total energy consumption from 1971 to 2010 subdivided by type. Key World Energy Statistics ©OECD/IEA, 2012. Copyright (2020)

More than 80% of current primary energy consumption comes from fossil fuels, but these will be consumed in the next century. The contribution of solar energy is very small. The International Energy Agency predicts a better future for photovoltaics in 2011. According to their speculations, photovoltaic systems could account for more than a third of the total energy demand in 2060 (see **Figure *5***).[9]

In contrast to fossil fuels such as coal and oil, solar energy is inexhaustible and is therefore one of the renewable or regenerative energies. Furthermore, it is clean, emission-free (no CO_2, soot, or fine dust) and available free of charge.
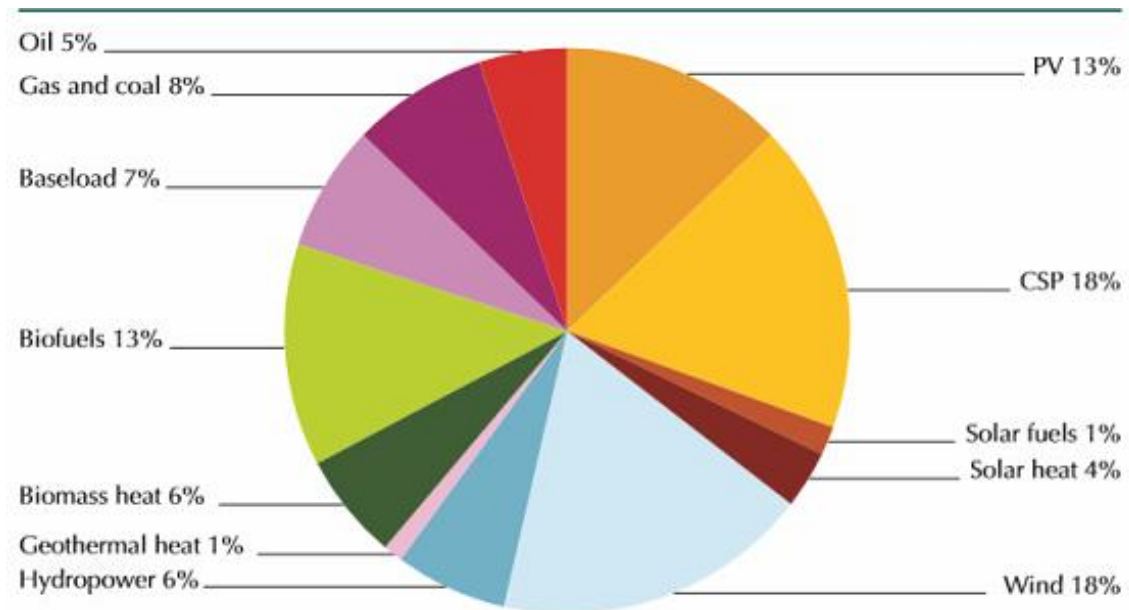
Figure 5. Estimation of total energy demand in 2060, subdivided by providing sources (PV: photovoltaics; CSP: concentrated solar power); Solar Energy Perspectives ©OECD/IEA, 2011.[9] Copyright (2020)

According to the International Energy Agency (IEA), the need for more and more energy will increase, especially in the next two decades, due to the great demand. Forecasts predict that global energy demand could even increase by a quarter by 2040. The IEA warns that if energy-efficient technologies are not used, these values could increase twofold. The biggest reason for this increase is the constant growth of the world's population.[10]

More than 80% of current primary energy consumption is derived from fossil fuels, but these will be used up in the next century. One of the greatest social challenges in the coming years will be to transform to alternative energy sources.

To stop global warming, fossil fuels such as coal (27%), natural gas (22%) and oil (32%) are to be replaced primarily by renewable energies and carbon-neutral fuel.[11] Of the greenhouse gases, CO_2 is most responsible for global warming. Most CO_2 emissions still

come from the combustion of fossil fuels. Smaller emissions are due to industrial processes (production of cement and other building materials) and agriculture. In addition to CO_2, two other gases are of great importance. CH_4 and NO_2 are much less human-made but are much more effective in terms of greenhouse gas effects than CO_2. They mainly arise as a by-product in animal husbandry, agriculture, or industry.

Strategies are primarily developed to combat global warming by eliminating the root causes of greenhouse gas generation. Humans cause three important emissions from their activities, including electricity and heat generation, transport, industrial production, and agriculture. Electricity generation, heating, transport, and industrial needs are the main responsibility for the largest share of emissions. Despite the reduction and sustainable use of renewable energies, worldwide energy continues to be supplied by burning fossil fuels (80%, see **Figure 6**).[12] A promising strategy to combat global warming would be to use climate-neutral sources (such as hydro, wind, geothermal energy, nuclear power, and the sun) instead of fossil fuels.
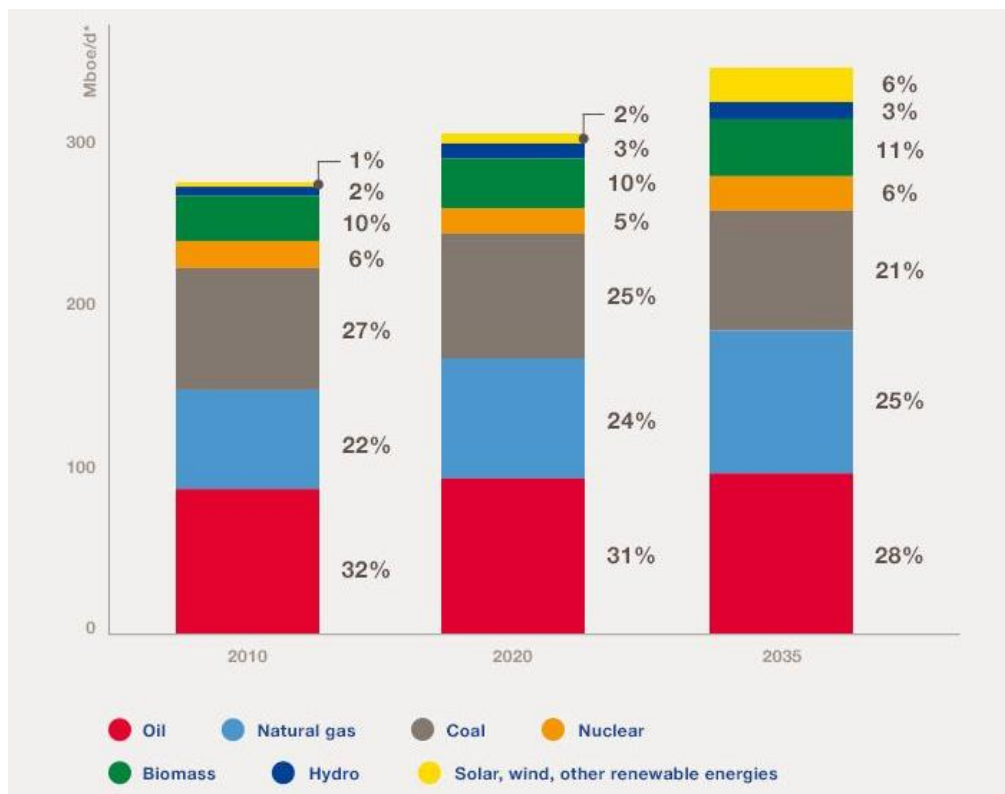
Figure 6. World primary energy mix (2010, 2020 and 2035 forecast).[12] Copyright (2020)

1.1.3 Potential of Renewable Energies

The Levelized Cost of Electricity (LCOE) refers to the cost of converting energy from another form of energy into electricity. These costs are usually quoted in euros or dollars per kilo- or megawatt hour (kWh, MWh). They include all lifetime costs of a power-generating system, such as initial capital investment, discount rate, as well as the costs of continuous operation, fuel (if any), and maintenance. Therefore, the LCOE represents the average minimum price at which electricity must be sold in order to achieve a balanced performance over the life of the project. Such a calculated value often helps in many policy issues, as well as in research, to make decisions. The average cost of solar cells has fallen from $76.67/watt (**Figure 7b**) in 1977 to just $0.13/watt in May 2019 for crystalline silicon solar cells and the module price has fallen to $0.23 per watt. While the price of solar components in the last years has dropped, LCOE has also dropped consequently (**Figure 7a**).[13,14] The cost of solar and renewable energy is steadily declining and it has been predicted that the cost will drop by 66% by 2040.[15,16]
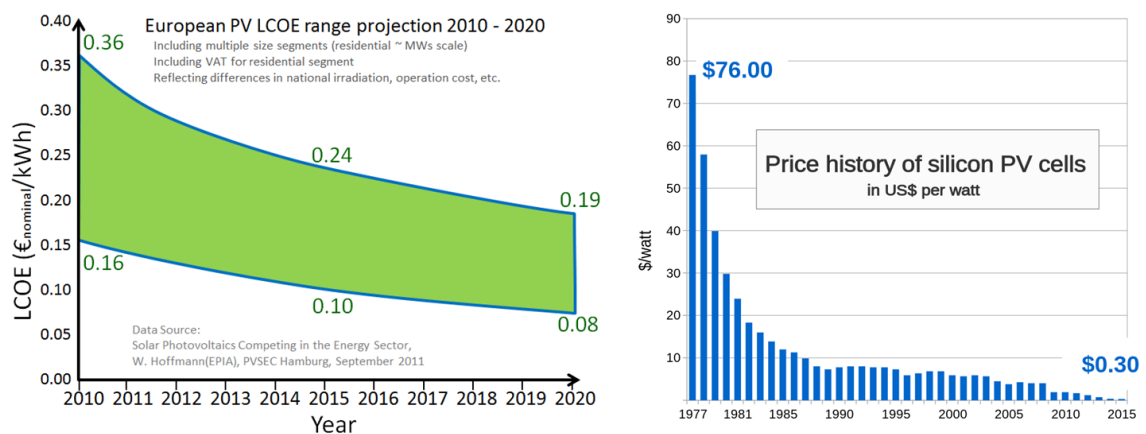
Figure 7. a) European PV LCOE range projection 2010-2020 (graphic left)[17] Copyright (2011) European Photovoltaic Industry Association and b) price history of silicon photovoltaic cells (graphic right)[18] Copyright (2020)

In principle, several materials are suitable for producing solar cells. However, 95 percent of all solar cells consist of silicon (monocrystalline and polycrystalline), the rest is made

up of thin-film technologies such as CdTe, CIGS and amorphous silicon (see *Figure 8*). Silicon is, after oxygen, the second most abundant element of the earth. Although the prices of these established technologies are rapidly falling, grid parity has not been fully achieved. That's why researchers are interested in new photovoltaic technologies that can be produced more cheaply. It is particularly important to use low-cost starting materials and simple production techniques. In addition, the cost of installing the new solar cells is to be reduced, but the efficiency and service life of the established photovoltaic technologies are to be increased. One of the most promising photovoltaic technologies in recent years are the perovskite solar cells (PCSs). In addition to the simple solution-based manufacturing technology and its thin layers, they are particularly cost-effective. Furthermore, no high-purity materials and no high temperatures are used in the production. In addition, compared to silicon solar cells, perovskite solar cells are more adaptable and can be made in many colors, which makes them particularly remarkable.
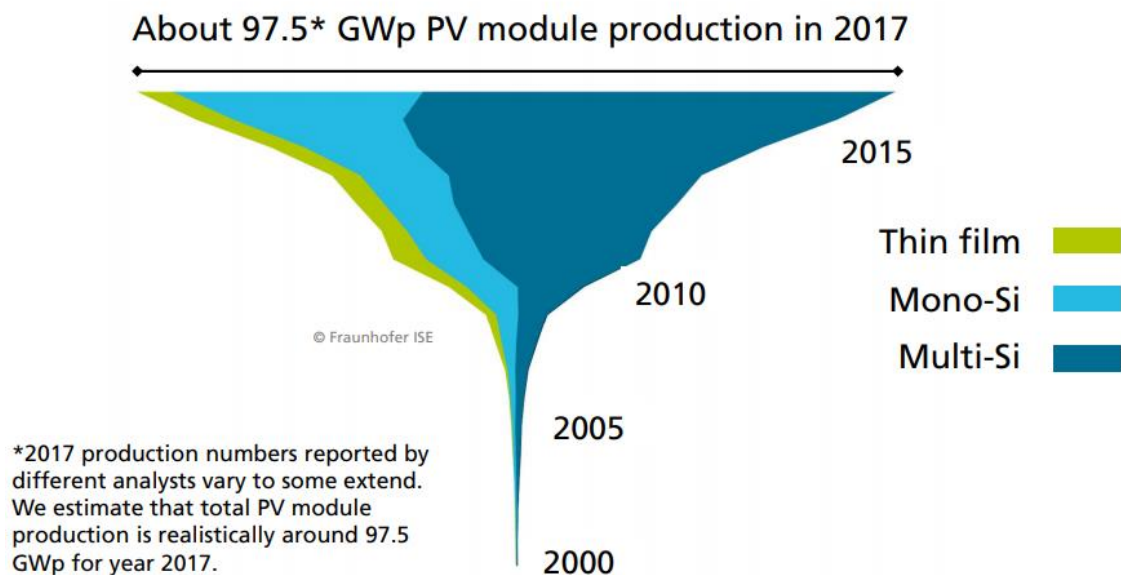
Figure 8. Worldwide annual PV production by technology (in GWp).[19] Copyright (2020)

2 THEORETICAL BACKGROUND

2.1 Perovskite Solar Cells (PSCs)

2.1.1 Structural Considerations of Perovskites

Perovskites are crystalline materials with an ABX_3 structure. Depending on the anion (X) used, a distinction is made between oxidic and non-oxide metal perovskites. Non-oxide perovskites contain chalcogenides (S^{2-}, Se^{2-}, Te^{2-}) or halides (Cl^-, Br^-, I^-) in their metal perovskite structure. Larger molecular anions (such as SCN-, HCOO-) can also be incorporated as anionic species (X).[20,21] In the ABX_3 structure A is occupied by a small monovalent organic (e.g. $CH_3NH_3^+$, $CH(NH_2)_2^+$, $(NH_2)_3C^+$) or an inorganic (e.g. Cs^+, K^+, Rb^+) cation, B is a divalent metal ion such as Pb^{2+}, Sn^{2+}, Ge^{2+}, Mg^{2+}, Ca^{2+}, Sr^{2+}, Ba^{2+}, Fe^{2+}, Pd^{2+}, Eu^{2+} or Cu^{2+} and X is a halide (I^-, Br^- or Cl^-). Figure 9 shows the three-dimensional structure of ABX_3, where A occupies the center of the cubic cell, whereas B occupies the corners of the cell and X lays in the mid-points of the edges. In this ideal case, the perovskite has a cubic symmetry where the BX_6 octahedra are connected via the corners and the cuboctahedral voids are occupied by the A-cations (see **Figure 9**).

A-site cations: $[CH_3NH_3]^+$, $[(NH_2)_2CH]^+$, Cs^+

B-site cations: Pb^{2+}, Sn^{2+}, Ge^{2+}, Cu^{2+}, Mn^{2+}

X-halogen anion: I^-, Br^-, Cl^-
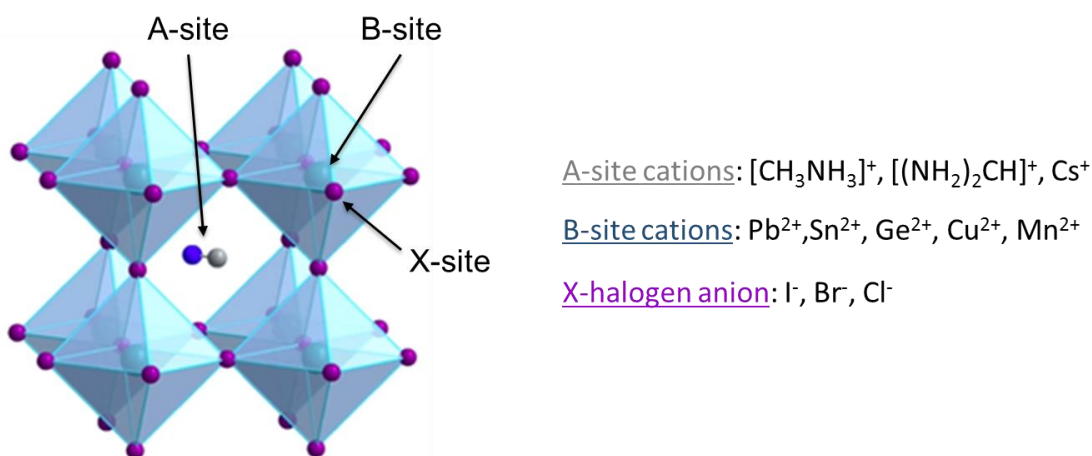
Figure 9. Crystal structure of ABX_3-type metal halide perovskite used for solar cells.[22] Copyright (2017) American Chemical Society

To form a stable perovskite, the octahedral factor μ, which represents the ratio of the radii of the B-cation (r_B) and the halide-ion (r_X) (see Equation 1), must be in the range $0.442 < \mu > 0.895$.

In 1926, Goldschmidt discovered that complete isomorphism (different solids appearing in the same crystal form) is only possible if their ionic radius (r_A, r_B and r_X) does not differ by more than 10-15%.[23] This was referred to as the Goldschmidt tolerance factor (t), which is calculated according to Equation 1. Such a parameter is used to determine the possible perovskite structures. Based on this calculation, ABX_3 perovskites can be formed if the tolerance factor t is in the following range $0.8 \leq t \leq 1.0$.

$$\mu = \frac{r_B}{r_X} \qquad\qquad t = \frac{r_A + r_X}{\sqrt{2}(r_B + r_X)}$$

(Equation 1)

When we change the A-site and the B-site with a smaller A- or larger B-ion, then the structure can be changed to an orthorhombic, rhombohedral or tetragonal, this is because the Goldschmidt tolerance factor t gets smaller than 1. Moreover, the size of the A-site has an influence on the dimensionality (D), so the perovskite with a large A-ion has a 2D structure or a one dimensionality chain material (see *Figure 10*).[24,25,26]
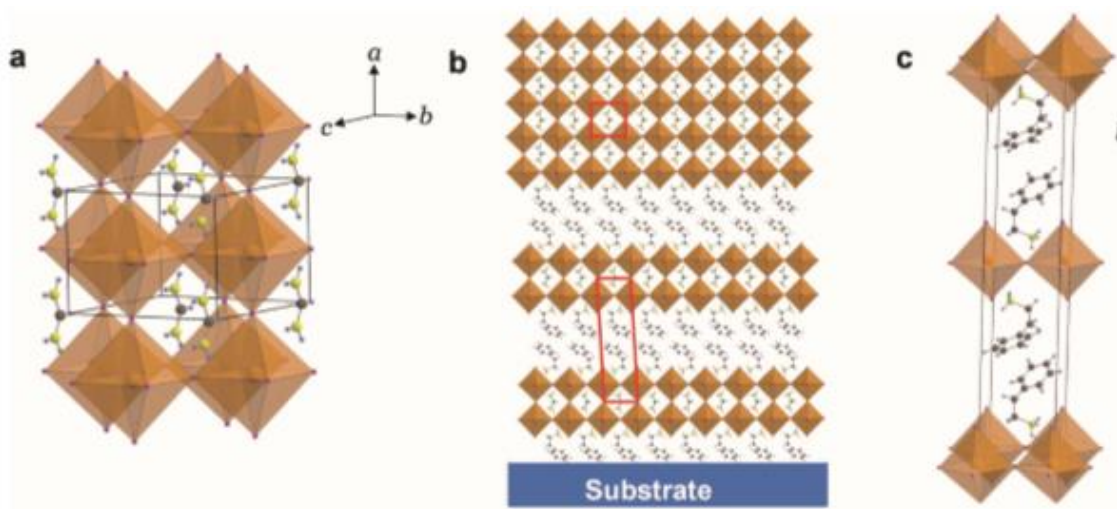
Figure 10. Crystal structure of a) 3D reference $FASnI_3$, b) 2D/3D mixture (2D 0.08 m), with the unit cells of each component outlined in red, and c) 2D PEA_2SnI_4.[27] Copyright (2018) Adv. Energy Mater

Methyl ammonium lead iodide ($CH_3NH_3PbI_3$) was the first perovskite to excite the PV research field and one of the most extensively investigated for use in solar cells. The first PSCs-work was published in 2009 by Kojima[28], where the solar cells were prepared in a dye-sensitized solar cell (DSSC) architecture with $CH_3NH_3PbI_3$ as a perovskite. This material shows very good optoelectronic properties and was prepared in a low-temperature solution-based processing route. The bandgap of this material was characterized by 1.6 eV[29], which is close to the range of the optimal band gap (1.1 - 1.4 eV)[30,31] for efficient solar cells. The efficiency limit for this bandgap is about 31% under an AM1.5G solar spectrum at 1000 W/m².[32] An important feature of perovskites is that they have a diffusion length for both holes and electrons over one micrometer.[33,34] Such a material can efficiently diffuse the charge to the electrodes before a recombination takes place. This means that these materials can work effectively in a thin film (approximately 500 nm) architecture. In addition, they have a high absorption coefficient, which allows them, despite having thinner layers, to absorb the entire visible solar spectrum. These characteristics lead to the possibility of achieving low cost, high efficiency, thin, lightweight and flexible solar cells.

2.1.2 Device Architecture of the Pscs

Solar cells work by converting the energy of incident photons directly to electricity. PSCs are the most rapidly developing PV technology. In 2009 the first perovskite solar cells were discovered by Kojima et al.[28] and were based on the dye-sensitized solar cells (DSSC) architecture with a mesoporouse TiO   Layer (thickness of 8 - 12 µm). $CH_3NH_3PbI_3$ and $CH_3NH_3PbBr_3$ was used as a sensitizer in a liquid electrolyte based DSSC. This solar cell achieved a power conversion efficiency (PCE) of 3.81 (for x = I) and 3.13% (for x = Br).[35] Such perovskites, which are in a liquid electrolyte, show stability problems and dissolve quickly. 2012 Kim et al.[36] replaced the liquid electrolyte with the solid hole conductor and developed a solid-state, highly efficient (PCE 9.7%) and stable perovskite solar cell. Since then, PSCs have been intensively researched and have achieved efficiencies of over 25% in the shortest possible time.[37] Typically, PSCs are built on ITO (indium-doped tin oxide) or FTO (fluorine-doped tin oxide) glass and have a 300-500 nm perovskite layer surrounded with electron and hole charge transport layers (ETL and HTL). Au, Ag and Al are the most used metal electrodes. Depending on

which transport material (ETL or HTL) is present on the exterior portion of the solar cell and so first incident light, PSCs can be classified as normal (n-i-p) and inverted (p-i-n) structures. These structures can be further divided into two categories: mesoporous and planar (*Figure 11*).
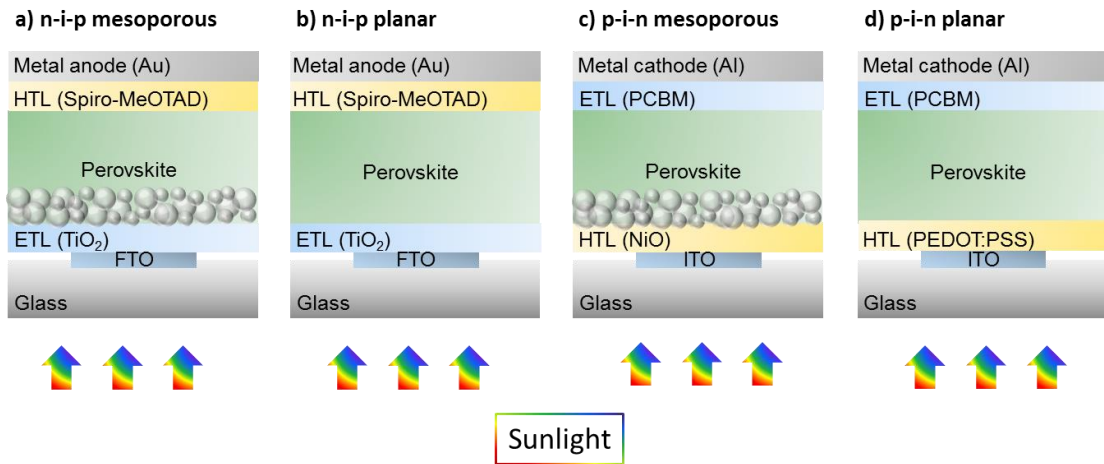
Figure 11. Device architecture of perovskite solar cells: a) n-i-p mesoporous, b) n-i-p planar, c) p-i-n mesoporous and d) p-i-n planar; self-designed based on references.

2.1.3 Working Principle of the PSCs
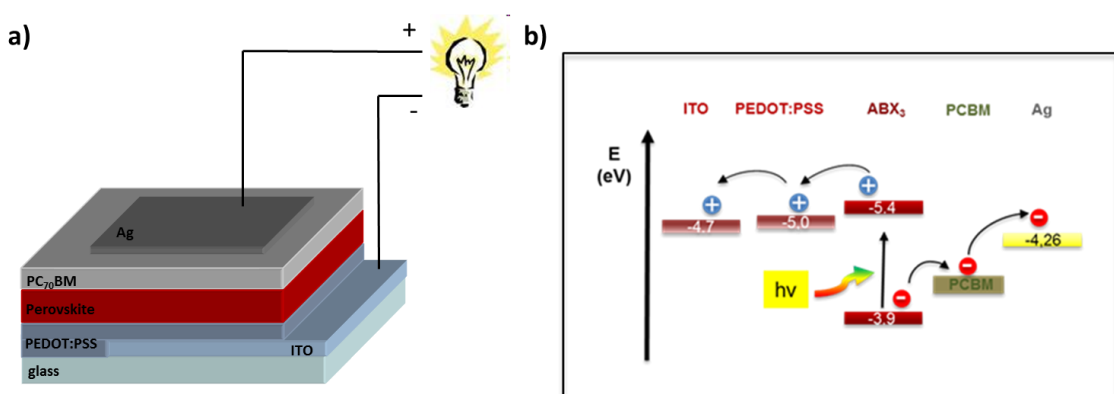
Figure 12. (a) Schematic illustration of a PSC with a planar p-i-n architecture using PEDOT:PSS as hole and $PC_{70}BM$ as electron transport layer and (b) energy level diagram of the planar PSC showing collection and separation of photo-generated electrons.

A schematic representation of the functional principle of a perovskite solar cell is shown in *Figure 12*. A perovskite-structured material is used as a light absorber for the photovoltaic activity. As soon as sunlight falls on a PSC, the perovskite material absorbs light, creating so-called excitons. Now, the exciton must overcome the binding energy and dissolve into electrons and holes with free charges. Perovskites are characterized by relatively high charge mobility and long charge diffusion lengths. They efficiently transport both holes and electrons. As soon as the electron is separated from the hole and injected into the electron-transporting layer (ETL), it can migrate to the anode. The hole is injected into the hole transport layer (HTL) and then migrates to the cathode.[38] An electrical field builds up where a current circuit is formed over the metal contacts.[39]

Figure 13 shows a planar p-i-n architecture. ETL consists of a continuous $PC_{70}BM$ layer. In this case, HTL is PEDOT: PSS. Both layers were deposited by spin coating. The electrode is thermally vaporized and consists of silver.
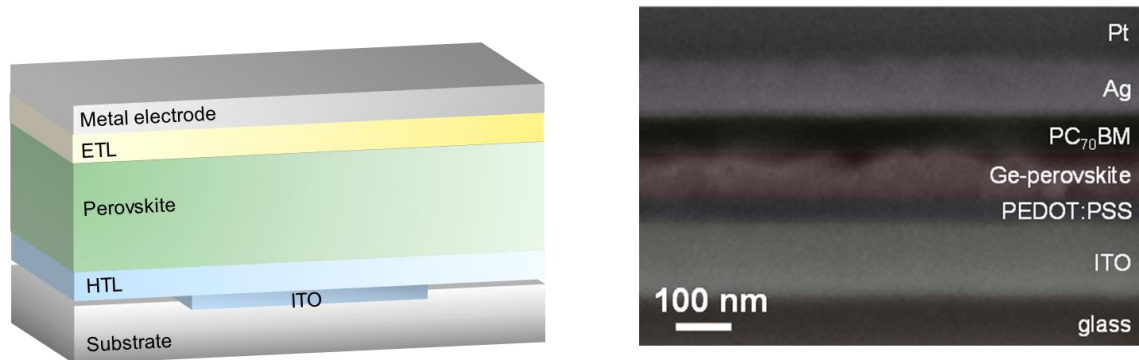
Figure 13. Perovskite solar cell architecture with PEDOT:PSS (HTL) and $PC_{70}BM$ (ETL) (left) and SEM image of a FIB processed cross-section (right).

2.1.4 Characteristic Solar Cell Parameters

A current–voltage characteristic or I–V curve (current–voltage curve), as a chart or graph, are used for describing the performance of solar cells. To get such a graph, typically a solar simulator unit with a standard light source can be used. In this case, the voltage is varied during the measurement and the corresponding current is read. All solar cells are measured at standard test conditions in the dark and under illumination. At standard conditions the solar cells are tested under the global (G) air mass (AM) of 1.5 G condition, at a temperature of 25 °C, and with an intensity of $1000 W/m^2$ ($100 mW/cm^2$). The IV-curves give information about the ability of the solar cell to convert sunlight into electricity. The curves obtained show a diode-like shape and they give information about the performance of the solar cell. *Figure 14* shows a typical IV characteristic with a curve (red line), which crosses the voltage at the x-axis at the point V_{OC} (open circuit voltage; voltage at zero current) and the y-axis at the point I_{SC} (short circuit current; current density at zero voltage). P_{max} (maximum power output) is defined at the maximum power point (MPP) and the product of I_{MPP} and V_{MPP}. The fill factor (FF) is the quotient of the P_{max} of a solar cell at the MPP and the product of V_{OC} and I_{SC}. In the present diagram (*Figure 14*), the fill factor is considered to be the ratio of the blue to the green area. The fill factor is dimensionless and serves as a measure of the quality of the solar cell.
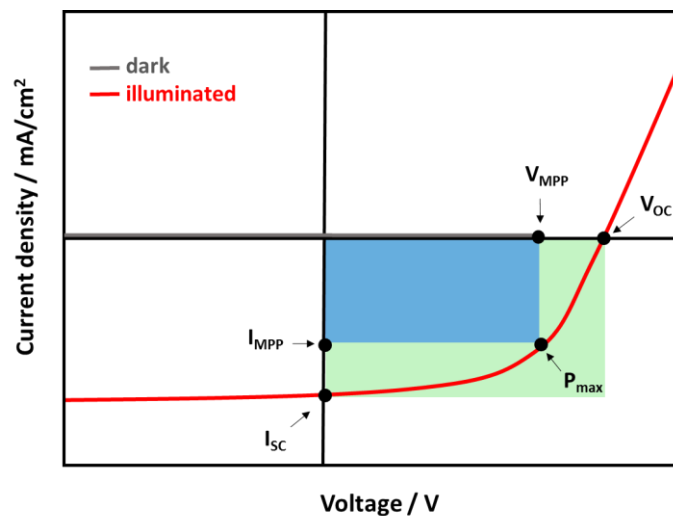
Figure 14. Current–voltage characteristic of a solar cell with corresponding parameters like the I_{SC}, V_{OC}, I_{MPP}, V_{MPP}.

$$PCE = \frac{P_{max}}{P_{in}} = \frac{V_{MPP} * I_{MPP}}{P_{in}} = FF * \frac{I_{SC} * V_{OC}}{P i_n} \qquad FF = \frac{P_{max}}{I_{SC} * V_{OC}} = \frac{V_{MPP} * I_{MPP}}{I_{SC} * V_{OC}}$$

(Equation 2)

2.1.5 Challenges with PSCs

Hysteresis

An I-V hysteresis effect is a phenomenon, whereby scanning the voltage on its terminals, the forward scanning (FS) I-V curve is different from the reverse scanning (RS). According to the shape of the IV curves, perovskite solar cells are divided into three categories of hysteresis: normal, free, and inverted, see *Figure 15*. If the photocurrent and the fill factor or the open circuit voltage of the reverse scan (RS) are higher than those of the forward scan (FS), then one speaks of normal hysteresis. In the case of an inverted hysteresis, the two parameters or the open circuit voltage in the FS are increased compared to those in the RS.[40,41] If both normal and inverted hysteresis are present in the IV curves, then one speaks of a mixed hysteresis. The type of hysteresis in PSC depends on both the sampling rate and the perovskite material.[41]
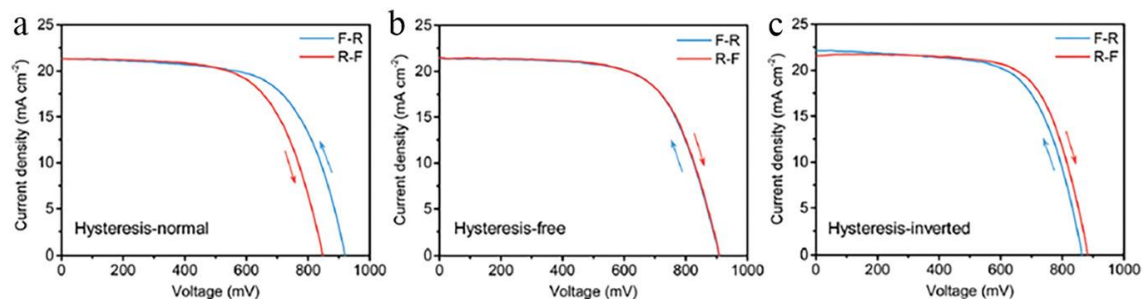
Figure 15. Different types of hysteresis in PSCs. Copyright 2017, Royal Society of Chemistry.

Such behavior in solar cells can be caused by different reasons: ion migration, device architecture, scanning rate and scanning direction, light soaking, and defects.[42,43,44] Such a hysteresis effect could also be observed in other types of solar cells that have high

internal capacities (for example in CIGS, CdTe, silicon solar cells). Studies on CdTe devices show that the hysteresis can be related to the accumulation of charge carriers and the defect states.[45] In PSC, a larger hysteresis effect can lead to instability of the solar cells.[46] Snaith et al. first reported abnormal hysteresis in PSC in 2014.[47] It was observed that the hysteresis mainly resulted from the presence of the perovskite absorber and depended on the contact materials.

Many research groups have investigated and described the causes of hysteresis extensively. The solar cell architecture must also be carefully selected in order to be able to eliminate the hysteresis effect. For example, hysteresis can be observed for a lot of device architectures (on compact and mesoporous TiO_2, Al_2O_3, with and without HTL). Inverted planar PSCs, typically using PCBM or C_{60} as the ETL material and PEDOT: PSS or nickel oxide as the HTL material, show a reduced hysteresis compared to the regular planar heterojunction structures based on TiO_2.[48] PSCs based on Al_2O_3 show a more severe hysteresis compared to mp-TiO_2 PSCs.[49]

Kang et al investigated the hysteresis behavior of PSCs as a function of the perovskite composition with normal mesoscopic and planar structure.[50] They found out that the capacitive current is responsible for the hysteresis. The ion migration and the non-radiative recombination near the interface play an important role. Bulk and interface defect engineering could eliminate the hysteresis in PCSs. Regardless of the perovskite composition, KI-doping turned out to be a good approach for hysteresis-free PSCs.

2.2 Lead-Free Based Perovskite Solar Cells

Consideration of lead-based perovskite solar cells shows that these solar cells have undergone rapid development in recent years and, with their latest efficiency of 23.7% [51], have surpassed commercial solar cells. Although the lead perovskite absorber serves as the ideal material for PSCs, it shows two major disadvantages. On the one hand, poor stability and on the other hand, the known high toxicity of lead. [52] The stability of such PSCs can be significantly improved by low-dimensional (such as 2D perovskite) or mixed low-dimensional Perovskite (mixed 2D / 3D perovskite), by improved device development, and with the help of encapsulation. [53,54] In comparison, toxicity is a much bigger problem. Lead is also carcinogenic, bioavailable and water-soluble, which could contaminate the soil and water supply. [55,56,57] In terms of the commercialization of solar cells, non-toxic and less reactive materials are preferred. Such materials should, however, have similar or better photovoltaic properties than lead, and should have a higher stability. So far, there are many theoretical and experimental studies that discuss possible alternative elements for the replacement of lead in perovskites.

Table 1 shows the ion radii and electronic configurations of various metal cations that are suitable for perovskite solar cells. Lead has an ion radius of 1.19 Å and can be replaced with metals with a similar ion radius.

Table 1. Ionic radii and electronic configurations of metal cations for perovskite solar cells. [58] Copyright (2019) Materials Chemistry Frontiers.

Metal cations	Ionic radius (Å)	Electronic configuration
Pb^{2+}	1.19	$6s^2$
Sn^{2+}	1.02	$5s^2$
Ge^{2+}	0.73	$4s^2$
Bi^{3+}	1.03	$6s^2$
Sb^{3+}	0.76	$5s^2$
Sn^{4+}	0.69	$4d^{10}$
Ti^{4+}	0.53	$3p^6$
Cu^{2+}	0.73	$3d^9$

Tin-based perovskites proved to be extremely promising, as they show the best efficiency in energy conversion. Germanium, copper, bismuth, antimony and other elements show promising properties in the research community. In this work, perovskite materials based on tin, bismuth and antimony for solar cells are briefly discussed, while perovskite solar cells based on germanium, the focus of this work, are considered in more detail.[59,60]

2.2.1 Tin Based Perovskite Solar Cells

Tin-based perovskite materials are characterized by very good optoelectric properties, which are very similar to lead-based perovskites.[61] Tin is in the same group as lead and is one of the most promising alternatives for lead-based perovskite materials. In comparison to other lead and lead-free alternatives, the tin perovskite has a significantly smaller band gap of 1.3 eV.[62,63] This value is very close to the ideal value for the band gap of 1.34 eV to achieve the maximum calculated efficiency of 33% for AM1.5 solar spectrum.[64,32] Despite the good properties of tin, it also has a major disadvantage compared to lead. Due to the reduced inert pair effect, it is not stable as Sn^{2+} and easily oxidizes to Sn^{4+}.[65] Therefore, many research groups in the perovskite community are trying to improve the stability of tin perovskite. The photovoltaic properties of tin perovskites can be significantly influenced by a targeted selection of the cation at the A-site and the halides used.[59,66] In order to obtain more efficient solar cells, different optimization of the manufacturing process is also carried out.[67,68] In addition, the addition of additives suppresses the oxidation of SnI_2.[69,70] All inorganic $CsSnI_3$ was shown to be a thermoelectric material, which showed good properties as a hole transport conductor in dye-sensitized solar cells. Excess Sn in $CsSnI_3$ (addition of 20% SnF_2 in the precursor solution) reduced Sn vacancies and improved solar cell performance, resulting in PCE values of 2.02% with photovoltaic parameters: $J_{SC} = 22.7$ mA cm^{-2}, $V_{OC} = 0.2$ V, and FF $= 0.37$.[70]

Furthermore, it can be said that tin halide perovskites $ASnX_3$ (A = MA, FA or Cs, X = I, Cl, Br) as lead-free absorber materials were most frequently investigated. In 2014, Noel et al. published the first lead-free tin halide perovskite semiconductor, methyl ammonium tin iodide ($CH_3NH_3SnI_3$). Built solar cells with a device architecture (glass/FTO/c-TiO_2/mp-TiO_2/$CH_3NH_3SnI_3$/Spiro-OMeTAD/Au) showed efficiencies above 6%. In the same year, a mixed halogen perovskite $MASn(I_{1-x}Br_x)_3$ with a device structure

(glass/FTO/c-TiO$_2$/mp-TiO$_2$/CH$_3$NH$_3$SnI$_3$/Spiro-OMeTAD/Au) and an efficiency of 4.6% was also reported.[71]

Liu et al. showed the positive influence of combined treatment with hot anti-solvent and DMSO vapor on the film coverage as well as the average crystallite size in FA$_{0.75}$MA$_{0.25}$SnI$_3$ and achieved an efficiency of more than 7%.[72]

Liao et al. reported in 2017 that the low-dimensional Sn-perovskites have significantly improved stability in the ambient atmosphere compared to their three-dimensional counterparts, and therefore the degradation under air exposure is reduced. The low-dimensional tin halide perovskite thin films were fabricated using PEA as an organic separating interlayer. They substituted the FA-cation of an FASnI$_3$ with PEA to obtain a perovskite with the following structure PEA$_x$FA$_{1-x}$SnI$_3$. It was also found that the orientation is modified by the variation in the PEA$^+$ ratio. With 20% PEA, a highly oriented perovskite film could be realized perpendicular to the substrate. With these highly oriented perovskite films, a PCE of 5.94% is achieved with a V$_{oc}$ of 0.59 V, a J$_{sc}$ of 14.44 mA/cm^2 and an FF of 69%. A significantly higher V$_{oc}$, compared to previously reported 3D-FASnI$_3$ perovskite solar cells (varied between 0.262 and 0.465 V), was observed in this study. Such prepared solar cells were stable for more than 100 hours.[73]

In the same year, Shao et al. [27] demonstrated even better solar cell performance with a PCE of 9%, by using a combination of 2D and 3D FASnI$_3$ in a planar p-i-n device structure. To achieve a 2D structure, they used very small amounts of PEAI. They showed that the addition of a very small amount (0.08 M) of layered (2D) tin perovskite in 0.92 M 3D tin perovskite induces excellent crystallinity and orientation of the 3D FASnI$_3$ grains. The best solar cell performance was with a PCE of 9%, an FF of 71%, a V$_{OC}$ of 0.53 V and a J$_{SC}$ of 24.1 mA cm^{-2} with an inverse device architecture: glass/ITO/PEDOT: PSS/FASnI$_3$ (2D/3D mixture)/C60,BCP/Al. In order not to deteriorate the device performance, only a concentration of 0.1 M from SnF$_2$ (reducing agent) was used. In 2020, Liu et al reported tin perovskite solar cells, which consist of an amorphous layer of three halogen halides and cesium formamidinium tin iodide polycrystals. This structure blocked ion diffusion, oxygen and moisture and achieved a PCE value of over 10%.[74] Furthermore, in 2020 K. Nishimura et al reported the highest efficiency for lead-free tin halide PSCs using mixed cations (GeI$_2$ doped (FA$_{0.9}$EA$_{0.1}$)$_{0.98}$EDA$_{0.01}$SnI$_3$). The best solar cell performance was achieved with a PCE of 13.24% with a J$_{SC}$ of 20.32 mA cm^{-2}, an

FF of 0.78 and a V_{OC} of 0.84 V. For pure lead-free tin perovskite, this is the highest reported PCE value to date. [75]

2.2.2 Bismuth Based Perovskite Solar Cell

In the periodic table, bismuth is right next to lead and is therefore in the 15 group. Because of its similar electronic configuration, it has properties comparable to those of lead. [76] It is less toxic, which makes it particularly attractive, and it is used in medication. [77,78] Methylammonium bismuth iodide perovskite ($MA_3Bi_2I_9$) is a much studied, low toxic and air stable compound with promising properties. [79] In a planar normal device architecture (glass/FTO/TiO$_2$/MA$_3$Bi$_2$I$_9$/ P$_3$HT/Au) they were developed and examined by Lyu et al.[80], whereby a PCE of 0.08% was achieved. Ran et al. [81] managed to achieve a PCE of 0.39% in a planar inverted structure (glass/ ITO/PEDOT:PSS/MA$_3$Bi$_2$I$_9$/C60/BCP/Ag). The same perovskite material was able to achieve a PCE of 0.42% in a mesoporous device architecture (glass/ITO/TiO$_2$/m-TiO$_2$/MA$_3$Bi$_2$I$_9$/Spiro-MeOTAD/MoO$_3$/Ag). Because of the relatively high bandgap energy of 2.1 eV and poor surface morphologies, only a PCE of 1.09% for bismuth-based perovskites has been achieved so far. Park et al. published this result in a mesoporous structure (glass/FTO/c-TiO$_2$/mp-TiO$_2$/Cs$_3$Bi$_2$I$_9$/Spiro-OMeDAT/Ag), using cesium bismuth iodide (Cs$_3$Bi$_2$I$_9$) as absorber material.[82] Although bismuth-based perovskite solar cells have been extensively studied, the efficiencies are still very low, so further research is urgently needed to eliminate problems (such as poor morphology).

Organic-inorganic hybrid double perovskite $MA_2B^+Bi^{3+}X_6$ (X = I, Br, Cl; B = Ag, Tl, K) are more promising. Greul et al.[83] published a BiAg-based doubleperovskite ($MA_2AgBiBr_6$) with a low bandgap of 2.02 eV and achieved record efficiency of 2.43% in a mesoporous setup (glass/FTO/c-TiO$_2$/mp-TiO$_2$/absorber/spiro-OMeTAD/Au). In 2018, Fan et al showed that solar cells based on $Cs_3Bi_2I_9$ nanosheets instead of $Cs_3Bi_2I_9$ films have remarkably improved photovoltaic performance. By using CuI as HTM, a PCE value of 3.2% could be achieved.[84]

2.2.3 Germanium Based Perovskite Solar Cells

Germanium, which is like tin and lead, a group 14 element, is a further conclusive candidate for perovskite solar cells. Germanium has the same valent state as lead. In comparison to Pb^{2+}, Ge^{2+} exhibits a higher electronegativity, a more covalent character and an ionic radius (73 pm), which is smaller than the one of Pb^{2+} (119 pm). Interestingly, even though numerous theoretical studies attest to these materials having promising properties for solar cell applications,[85,86,87,88] germanium halide perovskites have rarely been investigated experimentally. This is most likely due to the instability of the Ge^{2+} ion towards oxidation to Ge^{4+}. In addition, Ge^{2+} is easier to oxidize because the 4s ione pairs are more active than the 6s ione pairs of lead. The same problem can be observed with tin-based perovskites, which can lead to metallic conductivity as well as short-circuits in the solar cell material.[89,90,91] Goldschmidt tolerance factor calculations for different germanium halide perovskites, such as for $CH_3NH_3GeCl_3$ (1.005), $CH_3NH_3GeBr_3$ (0.988), and $CH_3NH_3GeI_3$ (0.965), show that such a perovskite can be formed (ideal range: $0.97 < t < 1.03$).[86,92] Similar to lead, germanium halide perovskites are said to have high absorption coefficients and carrier transport properties.[90,93,94] Theoretical band gap calculations of $CsGeX_3$ perovskites show that they depend on the halide ion, therefore $CsGeI_3$ (1.53 eV) < $CsGeBr_3$ (2.32 eV) < $CsGeCl_3$ (3.67 eV).[92] Sun et al. examined methylammonium germanium halide perovskites and a similar trend was observed: $CH_3NH_3GeI_3$ (1.61 eV) < $CH_3NH_3GeBr_3$ (2.81 eV) < $CH_3NH_3GeCl_3$ (3.76 eV).[90]

Stoumpos et al. investigated a series of germanium halide perovskites with regard to their structural and optical properties and found that germanium perovskites crystallize in a trigonal crystal structure and possess suitable band gaps for solar cell applications (e.g. 1.9 eV for $MAGeI_3$, MA: methylammonium).[85] Furthermore, mixed tin and germanium halide perovskites were theoretically studied regarding applications in photovoltaics and small effective masses as well as low exciton-binding energies are predicted for these compounds.[86]

Germanium perovskite solar cells were first reported in 2015 by Krishnamoorthy et al.[90] $CsGeI_3$ based solar cells led to a PCE of 0.11%, while a PCE of 0.2% was obtained using $MAGeI_3$ as absorber layer (***Figure 16***). Here, the absorber materials were built in mesostructured perovskite solar cells on fluorine-doped tin oxide-coated glass substrates.

Figure 16c shows that poor performance and limited V_{OC} could be achieved, which is likely due to the rapid decomposition of theperovskite due to the oxidation of germanium.
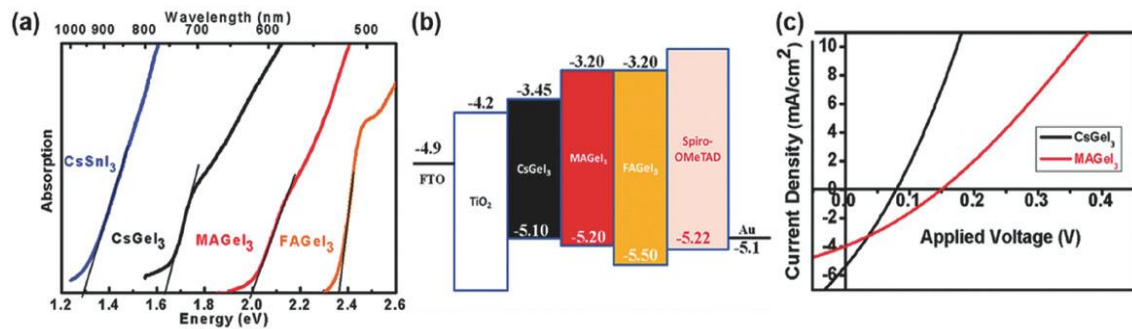
Figure 16. a) Optical absorption spectrum of CsGeI3, MAGeI3, and FAGeI3, in comparison with CsSnI3; b) Schematic energy level diagram of CsGeI3, MAGeI3, and FAGeI3; c) J–V curves of photovoltaic devices fabricated with different germanium halide perovskites.[90] Copyright 2015, RSC.

Chen reported in 2018 on a lead-free cesium germanium halide $CsGeX_3$ (X = Cl, Br, and I) perovskite, which was produced by solvothermal processes. The efficiency of the power conversion was 4.92%, by tuning the composition of the perovskite quantum rods.[95]

Mixed Ge- and Sn-perovskites are more promising. Compared to germanium-based perovskites, they show a narrower band gap and significantly better stability of the solar cells.[96, 102] At a conference in September 2018, S. Hayase et al. presented a new type of SnGe mixed metal perovskite solar cells with improved efficiency and stability. By doping the mixed cation tin halide perovskite $FA_{0.75}MA_{0.25}Sn_{1-x}Ge_xI_3$ with germanium, it was found that most Ge-atoms passivate the surface of the Sn perovskite. A mixed cation Sn perovskite ($FA_{0.75}MA_{0.25}SnI_3$) device without germanium showed an average J_{SC} 17.61 mA/cm², V_{OC} 0.46 V, FF 0.41 and PCE was 3.31%. Doping with 5 wt% of Ge increased the J_{SC} to 19.80 mA/cm², FF improved to 0.55 with an overall efficiency of 4.48% and doping with 10 wt% of Ge deteriorated all photovoltaic properties. Further optimizations increased the efficiency to 7.75% and significantly improved the air stability of the perovskite.[96]

In 2019, Chen et al.[102] demonstrate a lead-free, mixed allinorganic cesium tin-germanium triiodide ($CsSn_{0.5}Ge_{0.5}I_3$) perovskite absorber material with a band gap of 1.5 eV. The material was produced by thermal evaporation. In addition, to the promising efficiency of up to 7.11%, this absorber material showed a very high stability. After 500 hours of continuous operation in an N_2-atmosphere, without encapsulation, an efficiency drop of less than 10% was demonstrated. If the solar cells are exposed to ambient air, they can retain more than 90% of their original efficiency after 100 hours of continuous exposure. Such stability of the solar cells could be achieved by applying an ultra-thin GeO_2 surface layer to the absorber (glass/FTO/PCBM/$CsSn_{0.5}Ge_{0.5}I_3$/native oxide/Spiro-OMeTAD/Au).[102]

Table 2. Lead-free germanium halide perovskite absorbers: structural and optical data and the PCEs.

Perovskite	Dimensionality	Crystal system	Band gap [eV]	PCE [%]	References
$MAGeI_3$	3D	Trigonal	1.9–2.0	0.20	90, 97, 98
$MAGeBr_3$	3D	Trigonal	2.76–2.81	–	98, 99
$MAGeCl_3$	3D	Trigonal	3.74–3.76	–	98, 99
$MAGeI_{2.7}Br_{0.3}$	3D	Trigonal	2.1	0.57	100
$CsGeCl_3$	3D	Trigonal	3.4–3.67	–	98,99
$CsGeBr_3$	3D	Trigonal	2.32–2.4	–	98,99
$CsGeI_3$	3D	Trigonal	1.53–1.63	0.11 4.92	85, 90, 92, 93, 95, 101
$CH(NH_2)_2GeI_3$	3D	Trigonal	2.2–2.35	–	85, 90, 98
$CsSn_{0.5}Ge_{0.5}I_3$	3D	Trigonal	1.5	7.11	102
$RbSn_{0.5}Ge_{0.5}I_3$	3D	Trigonal	0.9-1.6	-	103
$GUAGeI_3$	3D	Monoclinic	2.7	–	85, 98
$TMAGeI_3$	3D	Hexagonal	2.8	–	85
$IPAGeI_3$	3D	Trigonal	2.7	–	85
$FA_{0.75}MA_{0.25}Sn_{0.95}Ge_{0.5}I_3$	3D	Trigonal		7.75	96

There are no further reports on germanium perovskite solar cells published so far besides one patent by Huang et al. application in which PCEs of 3% are claimed, however, only very limited data is provided.[104] For $CsGeI_3$, a theoretically maximum PCE of 27.9% was calculated using the Spectroscopic Limited Maximum Efficiency (SLME) mathematical model.[93]

2.3 Stability and Degradation

Perovskite solar cells are the fastest growing photovoltaic technology in history. In order to bring such a technology to the photovoltaic market, in addition to efficiency, there are also costs and lifetime considerations that should be taken into account. Only when these three points are met can a photovoltaic technology be commercialized. If you look at today's PV market, you can see that more than 90% of the current commercialized PVs are silicon PV. Silicon modules show an efficiency of 21%, they are also inexpensive (0.3 $ / watt), stable and therefore have a lifetime of more than 25 years.[105] In comparison, PSCs are half the price and show almost similar efficiencies. Their greatest disadvantage is their stability and thus their service life (see *Figure 17*). The longest lifetime of PSCs is currently around one year and is therefore the greatest hindrance to why this type of solar cell cannot be commercialized.[106,107]
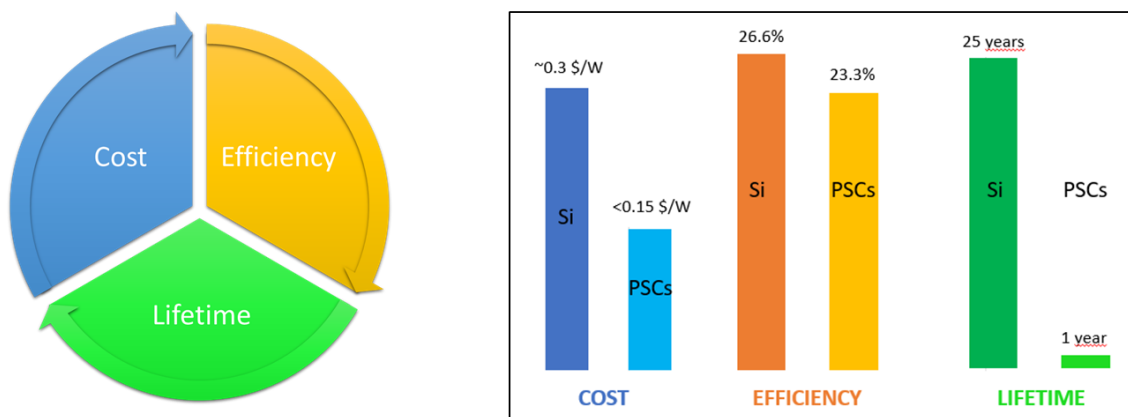
Figure 17. Comparison of perovskite and silicon solar cells based on cost, efficiency and lifetime.

The causes of this poor stability can be divided into two categories: extrinsic and intrinsic factors. Extrinsic factors are all environmental influences, such as: UV-light, oxygen, H_2O or mechanical stress. Encapsulation can avoid these factors. The intrinsic factors can in turn be broken down into intrinsic stability of the device architecture (chemical stability, illumination, temperature) and intrinsic stability of perovskite layer (illumination, temperature). In order to avoid the intrinsic factors, the perovskite material as well as the device architecture must be changed.

Perovskite materials are very sensitive to humidity.[108] An increased degradation takes place especially if the material comes into contact with air humidity in addition to UV

light, high temperatures or under an electric field.[109,110,111] The most used organic part (MA) of this compound is very hygroscopic. The water molecules form weak hydrogen bonds with the cations. This can produce a hydrated perovskite phase, which affects the perovskite structure. ***Figure 18*** shows schematic illustrations of different degradation pathways in PSCs.
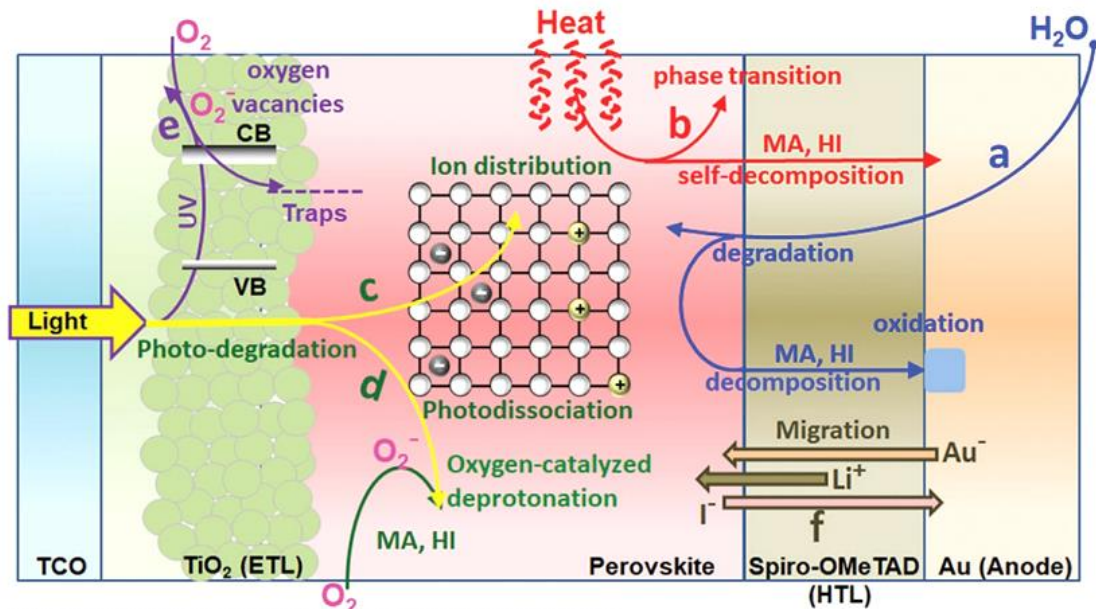
Figure 18: Degradation pathways induced by moisture, heat, and light in regular (n–i–p) architecture PSCs.[112] Copyright 2018, Adv. Mater.

The degradation of perovskites is closely related to their structural instability.[113] The presence of volatile organic components and mobile ion defects in particular lead to the degradation of the structure. While many research groups report on moisture-induced degradation, which makes the structure unstable, others report that a proportion of 30-35% moisture facilitates perovskite crystallization and improves the morphology of the layer.[114,115,116] Considering that MAI is hygroscopic[117], it helps absorb moisture within the grain boundary, thereby significantly increasing the grain size and suppressing the formation of pinholes, resulting in improved photovoltaic performance.[127],[118]

The moisture-induced degradation can be divided into three stages. Monohydrate (MAPbI$_3$ · H$_2$O) is already formed by low concentrations of moisture.[119] With higher humidity and prolonged exposure, dihydrate ((MA)$_4$PbI$_6$ · H$_2$O) and PbI$_2$ are being

formed which makes entire process partially irreversible.[132],120,121 In the event of longer exposure, the perovskite irreversibly decomposes into PbI_2 and volatile MAI.[133][134]

Furthermore, oxygen leads to a rapid degradation of the perovskite, this process can take from minutes to a few hours. If the perovskite is exposed to light and oxygen, a superoxide is generated which decomposes the perovskite into PbI_2, methylamine, iodine, and water.[122,123]

Aristidou et al. reported that light-induced superoxide species form much more easily on perovskite films with smaller grain sizes. Thus perovskites with poor crystallinity are degraded significantly faster and are also more unstable.[124]

Unencapsulated perovskite solar cells can be stable (in ambient air) for up to 500 hours under direct sunlight and 1000 hours under full sunlight. However, these values are still far from commercial standards.[125,126]

These powerful photovoltaic devices could be on the market in the near future. In order to commercialize this phenomenal technology, there are still some issues to be solved. These include, for example: a scalable and reproducible process, controlled production of thin layers, high stability and long life as well as low toxicity.

3 AIM OF THIS THESIS

When I started my PhD, perovskite solar cells were on the way to revolutionizing the photovoltaic industry with their low fabrication cost and high efficiency. Because of the toxicity issues of lead halide perovskites, which are so far the best performing compounds in this class of materials, this work should produce a lead-free perovskite material and investigate its photovoltaic properties.

For this reason, this thesis is divided into the four following sections:

The first target was to prepare a new perovskite material for solar cells as an alternative to the lead-based perovskite. Many metals were tested, but germanium showed the most promising results. One major problem of these perovskite materials is the easy oxidation of Ge^{2+}, which causes stability problems and a poor solar cell performance. In addition to the homovalent substitution of the divalent lead cation (Pb^{2+}) with the group 14 element cation germanium (Ge^{2+}), the optimal solvent as well as the optoelectronic properties and the photovoltaic performance of experimental and theoretical experiments of the first germanium iodid perovskites ($MAGeI_3$, $FAGeI_3$ and $CsGeI_3$) were discussed.

In a second study, the germanium perovskite was stabilized by modifying the chemical composition of the germanium perovskite, therefore by introducing bromide ions into the methylammonium germanium iodide perovskite ($MAGeI_3$) and improving the solar cell performance.

The third topic of this thesis is to investigate the positive influence of the PEA^+ (phenethylammonium) on the germanium perovskites. To check this behavior, the PEA^+ was added to the perovskite in different concentrations and integrated in solar cells, and the behavior of the solar cells was observed over 20 days.

Furthermore, an LED lamp was used to check whether the heat and light had a negative effect on the germanium perovskite and how the annealing step of the absorber layer influences the morphology of the layer.

The work describes also the new non-toxic perovskite materials to understand and improve the stability of perovskite solar cells. This thesis gives the photovoltaic community new non-toxic germanium perovskite materials and helps to understand their stability.

4 EXPERIMENTAL

4.1 Materials

4.1.1 Chemicals

GeI_2 (99.99%, ABCR), MAI and MABr (Dyesol), PEDOT:PSS (Clevios P VP.Al 4083, Heraeus), $PC_{70}BM$ (99.5%, Solenne BV), PEAI (Dyesol), FAI (≥98%, Sigma Aldrich), toluene (≥99.5%, Rotipuran®, Roth), 2-propanol (≥99.8%, Rotipuran®, Roth), anhydrous chlorobenzene (99.8%, Sigma Aldrich), DMF (≥99.9%, SeccoSolv®), DMSO (with a water content ≤0.02%), GBL (Microchem SU-8 5), Spiro-MeOTAD and FK-209 (99%, Sigma Aldrich), LiTFSi (99%, ACROS Organics), for TiO_2 layer Ti (IV) isopropoxide (97%, Sigma Aldrich), PMMA (100%, Sigma Aldrich).

4.1.2 Substrate

ITO coated glass substrates (15×15 mm^2, 15 Ω/square, purchased from Lumtec).

4.2 Methods of Analysis

4.2.1 X-Ray Diffraction (XRD)

X-ray diffraction measurements were conducted on a PANalytical Empyrean diffractometer in Bragg-Brentano configuration operated at 40 kV and 40 mA using Cu Kα radiation. For the XRD measurements, the perovskite films were prepared on glass slides and covered with a thin PMMA protection layer, spin coated from a chlorobenzene solution (10 mg/mL).

4.2.2 Optical Characterization

UV-Vis spectra were acquired with a Perkin Elmer Lambda 35 UV-Vis spectrometer equipped with an integrating sphere. For the UV-Vis measurements, the perovskite films were prepared on glass slides and covered with a thin PMMA protection layer, spin coated

from a chlorobenzene solution (10 mg/mL). All measurements were carried out in a wavelength scan range from 350 nm to 1000 nm with a slit width of 2 nm and a scan rate of 480 nm.

4.2.3 JV-Measurements

JV curves were recorded in a glovebox using a Keithley 2400 source measure unit and a custom made LabView software. The samples were illuminated by a Dedolight xenon lamp with a spectrum similar to the AM 1.5G spectrum at 100 mW/cm^2.

4.2.4 Contact Profilometer

The layer thickness (nm) was determined with a DektakXT Bruker surface profiler. A scratch in the layer was used to calculate the thickness of the coating. The scan length was set to 100 µm over the time duration of 3 seconds. The diamond stylus had a radius of 12.5 µm and the force was 3 mg with a measurement range of 6.5 µm. The profile was set to Hills and Valleys.

4.2.5 Optical Microscopy

The optical microscopy measurements were carried out with an Olympus BX60 microscope and the images were taken with an Olympus E-520 camera. Images were captured at maximum light intensity.

4.2.6 External Quantum Efficiency (EQE)

The EQE spectra were measured using monochromatic light from a MuLTImode4 monochromator (AMKO) equipped with a 75 W Xenon lamp chopped at 30 Hz. The signals (wavelength increment: 10 nm) were measured by a lock-in amplifier from Stanford Research Systems (Model SR830). A spectrally calibrated 818-UV/DB photodiode (Newport Corporation) was used as a reference. A sealed measuring box with a quartz glass window was used to protect the solar cells against ambient atmosphere during the EQE measurement.

4.2.7 Scanning Electron Microscopy - Energy Dispersive X-Ray Spectroscopy (SEM-EDX)

The investigation of the microstructure was performed by using a field emission scanning electron microscope (FESEM) TESCAN MIRA3 (TESCAN Brno s.r.o., Brno, Czech Republic) coupled with an energy dispersive X-ray spectrometer (EDS) Octane Plus detector and the TEAM v.4.5 software analysis (Ametek, Inc. Berwyn, PA, USA) were used. Thereby, SEM micrographs were acquired in In-Beam SE Mode, with an acceleration voltage of 3 kV, beam spot size of 4 nm and a working distance of 3.5 mm. The SEM micrographs were further analyzed using ImageJ software.

4.2.8 FIB/SEM

The cross section of the solar cell was prepared via the focused ion beam (FIB) technique using a FEI NOVA 200 FIB/SEM dual beam system with multiple current approach to minimize spatial sample damage. SEM imaging was done in low dose conditions to minimize e-beam related material alteration.

4.3 Device Fabrication

The devices were built in the same inverted planar device construction:

<p align="center">glass/ITO/PEDOT:PSS/Perovskite/PC$_{70}$BM/Ag</p>

ITO coated glass substrates (15 x 15 mm, 15 Ω/sq, purchased from Lumtec) were carefully rinsed with acetone and put into an isopropanol bath followed by sonication for 30 min at 40 °C. Subsequently, the substrates were dried under an N_2 gas stream and treated with oxygen plasma for 3 min. As first layer, a PEDOT:PSS (30 µl) film was spin coated (spin coater: Model XW-4A 220 Volts) at 6000 rpm for 30 s and the substrates were put into a glovebox immediately afterwards for a temperature treatment at 120 °C for 20 min. PEDOT:PSS was filtered with a 0.45 µm filter (PVDF-45/25 Chromafil Xtra). Next, the precursor solution was spin coated (spin coater: Model WS 650 MZ-23NPPB) onto the PEDOT:PSS film in glovebox atmosphere with the following spin coating conditions: 4000 rpm, 1000 rpm/s, 30 s. After 10 s of spinning, 30 µl chlorobenzene was

dropped onto the rotating substrate, whereupon the color of the film changed from yellow to orange/red. Afterwards, the perovskite was tempered at 70 °C for 10 min (programmable heating plate: MCS 66, CAT Ingenieurbüro M. Zipperer GmbH). The perovskite precursor solution was filtered before with a 0.45 µm filter (PTFE, 13 mm Syringe Filter). A $PC_{70}BM$ solution (30 µl) in dry chloroform (50 mg/mL) was spin coated on top of the perovskite layer with 1000 rpm, 500 rpm/s for 30 s. $PC_{70}BM$ was always filtered before spin coating with a 0.45 µm filter (PTFE, 13 mm Syringe Filter). Ag electrodes (3 x 3 mm²) were deposited by a thermal evaporation chamber MB-EVAP (mounted inside the glovebox) at a rate of 2 Å/s at a base pressure below $1x10^{-5}$ mbar. During thermal evaporation the substrates were rotated. The layer thickness was 100 nm for each electrode.

4.4 Perovskite Precursor Solution Preparation

The perovskite precursor solutions were prepared under nitrogen atmosphere in the glovebox (MBraun). A 1 M precursor solution was prepared by dissolving GeI_2 in dry DMF. The cations were added in a ratio such that a 1 M solution concerning the cations was obtained. In the case of $MA_{0.9}PEA_{0.1}GeI_3$ there were added 90 mol% of MAI and 10 mol% PEAI. The solution was stirred for 24 h at room temperature in N_2 atmosphere in a glovebox. Before use, the precursor solution was filtered through a 0.45 µm PTFE filter.

5 RESULTS

5.1 Solubility of Germanium Perovskites

Properties of perovskite layers that are prepared by a solution-based process are heavily dependent on the solvent used. Thus, different solvents can have differences in absorption, film thickness, film coverage, roughness, and crystallization. Solvents therefore have a major influence on the efficiency of a solar cell.

The optimal solvent should be found for the preparation of methylammonium germanium perovskite. For this, five different solutions or mixed solvents were considered. The solvents used were dimethylformamide (DMF), γ-butyrolactone (GBL), dimethyl sulfoxide (DMSO), a mixture of DMF and DMSO (4:1), and a mixture of DMF and GBL (4:1), respectively (see *Figure 19*). Unfortunately, the GeI_2 and MAI did not completely dissolve in any of the solvents.
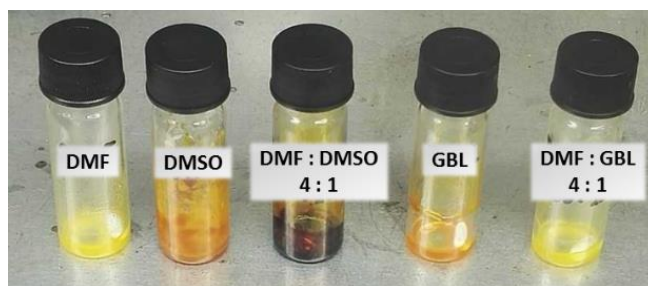
Figure 19. Photograph of precursors, using DMF, DMSO, DMF and DMSO (4:1), GBL, and DMF and GBL (4:1) as a solvent.

Figure 20A shows the absorption spectra of the germanium perovskite layers. $MAGeI_3$ layer fabricated from DMF, GBL and DMF:GBL (4:1) show similar absorption spectra. The absorption coefficients of the $MAGeI_3$ layer fabricated from the solvent DMF were higher than that of $MAGeI_3$ layers fabricated from GBL and DMF:GBL (4:1) because of the large amount of crystallization in the film (*Figure 20B*). DMF and a DMF:DMSO

mixtures are very suitable as solvents in perovskites and promote a homogeneous, crystalline layer formation in the antisolvent step. However, the DMSO has a negative influence on germanium. Adding small amounts of DMSO to the precursor solution prevents perovskite formation. There is no homogeneous layers because such precursor solution is very viscous and sticky. The lower absorption of perovskite layers fabricated from GBL was ascribed to the lower solubility in this solvent of the materials GeI_2 and MAI.

The X-ray diffractograms of the prepared germanium perovskites fabricated using various solvents are depicted in *Figure 20B*. The main peaks of the simulated diffraction pattern for trigonal $MAGeI_3$ (based on single crystal X-ray diffraction data reported by Stoumpos et al.[85]) at 14.3°, 25.4° and 29.0° 2θ match well with the measured diffraction peaks of the prepared thin films fabricated from DMF, GBL and DMF:GBL (4:1). The perovskite layers prepared from the DMF and GBL solvents are highly crystalline structures.
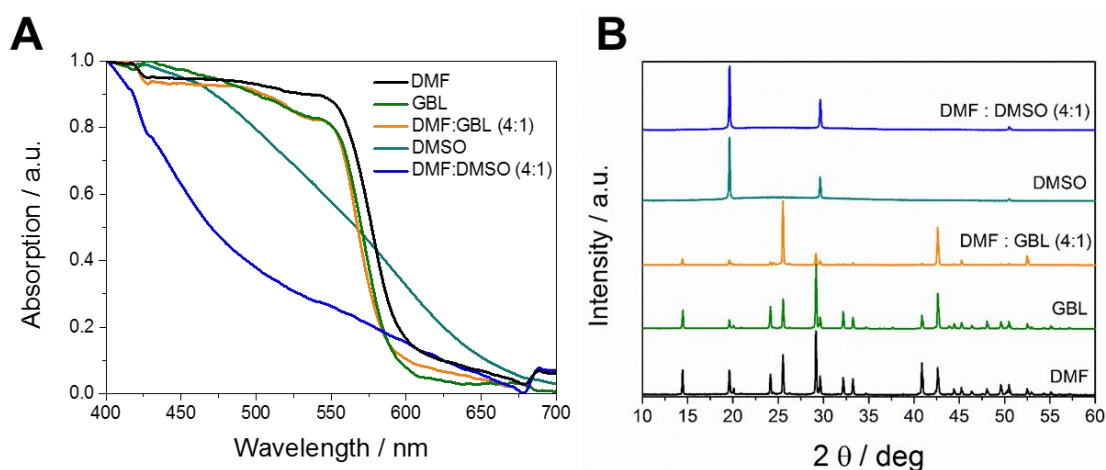
Figure 20. (A) Absorption spectra and (B) X-ray diffraction patterns of germanium perovskite layers fabricated from various solvents.

5.2 Fabrication and Characterization of the First Germanium Iodid Perovskites

The first three germanium iodide perovskite materials $AGeI_3$ (A = Cs, MA (CH_3NH_3) or FA ($HC(NH_2)_2$)) were synthesized experimentally. ***Figure 21*** shows photos of $MAGeI_3$, $FAGeI_3$ and $CsGeI_3$ perovskite films deposited on glass.
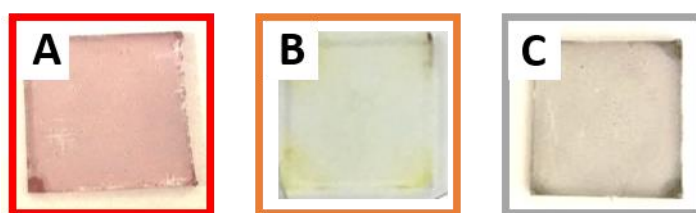
Figure 21. Photos of $MAGeI_3$ (A), $FAGeI_3$ (B) and $CsGeI_3$ (C) films deposited on glass.

By applying different A^+-cations, the colour of the compound's changes from red (A=MA^+) to yellowish (A=FA^+) and black (A=Cs^+). Germanium (II) iodide as educt, is bright yellow as well, which might indicate that the $FAGeI_3$ perovskite is not formed.

Photos and light microscopic images of $MAGeI_3$, $FAGeI_3$ and $CsGeI_3$ films deposited on glass outside the glovebox are shown in ***Figure 22***. A very rapid degradation of $MAGeI_3$ perovskites and poor film-forming abilities of the $CsGeI_3$ perovskites were found.
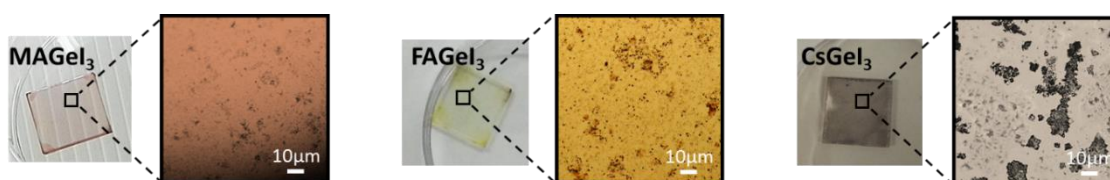
Figure 22. Photos and light microscopic images of $MAGeI_3$, $FAGeI_3$ and $CsGeI_3$ films deposited on glass. (1000x magnification).

The solar cells with $FAGeI_3$ as active layers have not worked properly and mainly short circuited solar cells have been obtained. On the other hand, the solar cells based on $MAGeI_3$ and $CsGeI_3$ show good performance and efficiencies up to 0.13% (see Figure 23 and Table 3).
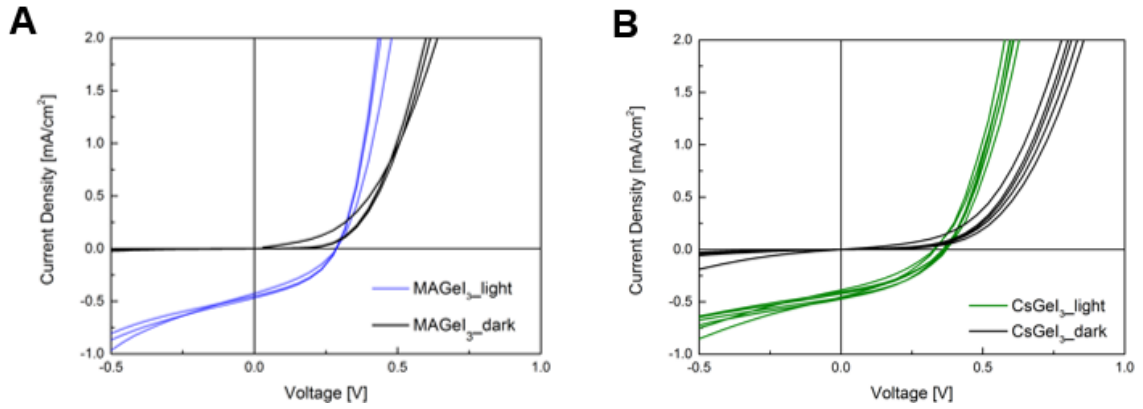
Figure 23. J–V curves of photovoltaic devices fabricated with different germanium halide perovskites: $MAGeI_3$ (A) and $CsGeI_3$ (B).

Table 3. Parameters including mean values and standard deviations of the solar cells extracted from the JV curves shown in *Figure 23*. The highest efficiency of the measured solar cells is given in the second line.

	V_{OC} / V	J_{SC} / mA cm^{-2}	FF / %	PCE / %
$MAGeI_3$	263 ± 34	1.21 ± 0.48	38.01 ± 6.20	0.11 ± 0.01
	276	1.07	41.74	(max. 0.12)
$CsGeI_3$	343 ± 0.02	0.99 ± 0.07	38.49 ± 1.44	0.13 ± 0.12
	357	1.05	40.88	(max. 0.15)
$FAGeI_3$	42 ± 0.02	0.88 ± 0.21	69.97 ± 35.8	0.03 ± 0.02
	50	1.03	88.89	(max. 0.05)

The absorption spectra of $MAGeI_3$, $FAGeI_3$ and $CsGeI_3$ show a high absorption below 650 nm, 450 nm and 750 nm. The optical band gaps were determined, and they are different for the prepared perovskites: 1.93 eV ($MAGeI_3$), 2.16 eV ($FAGeI_3$) and 1.61 eV ($CsGeI_3$). Nevertheless, these results are in good agreement with the literature values (2.0 eV, 2.35 eV and 1.63 eV)[85,90] (see *Figure 24* and *Table 4*). In terms of optical properties,

these materials are potential candidates for the application as absorber materials in solar cells.
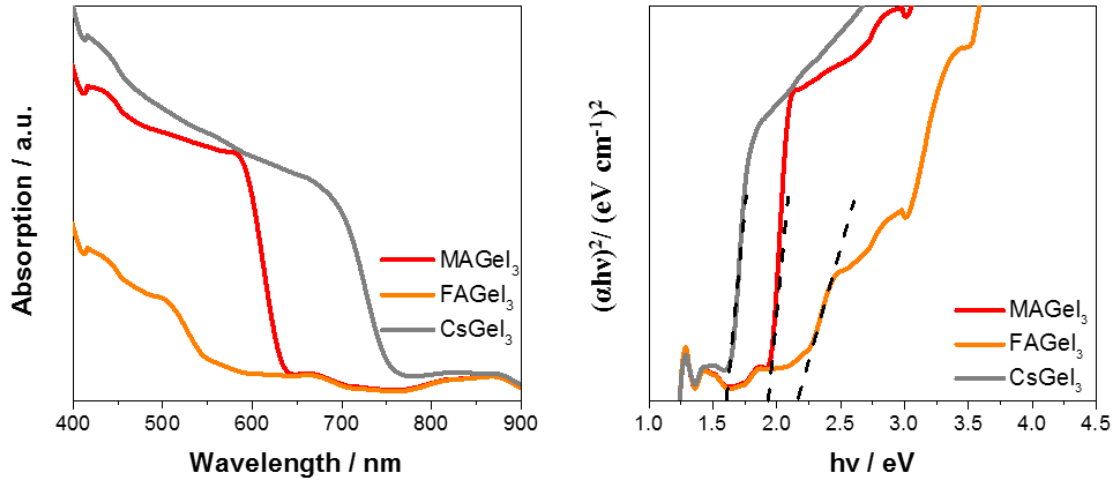
Figure 24. UV-Vis absorption data of MAGeI₃, FAGeI₃ and CsGeI₃ films deposited on glass (left) and Calculation of the band gap for these perovskites via the Tauc-Plot with a band gap energy of 1.93 eV, 2.16 eV and 1.61 eV (right).

Table 4. Experimentally and literature band gap determination of the germanium perovskites.

Perovskite	Band gap / eV (Experimentally)	Band gap / eV (Literature)
MAPbI₃	1.58	1.6 [85]
MAGeI₃	1.93	2.0 [90]
FAGeI₃	2.16	2.35 [90]
CsGeI₃	1.61	1.63 [90]
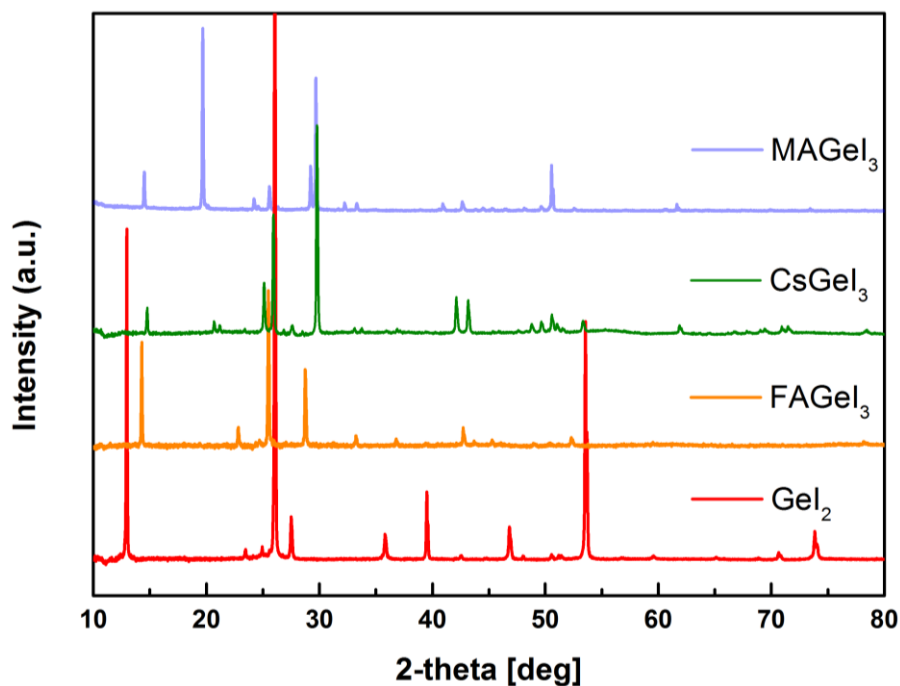
Figure 25. XRD pattern of a produced germanium perovskites (MAGeI$_3$, FAGeI$_3$ and CsGeI$_3$) films. Peaks of the starting compound GeI$_2$ are also present in the diffractogram.

The formation of the germanium perovskites via a low-temperature solution based processing route was confirmed by XRD measurements. Comparing the X-ray diffraction patterns of the perovskites with the educt GeI$_2$, the corresponding starting material was not found in the perovskites.

In summary, germanium (II) may act as a suitable replacement for lead in metal halide perovskite materials for solar cell applications. MAGeI$_3$ and CsGeI$_3$ are solution-processable perovskite absorber materials with low toxicity and band gaps in the range of 1.6-2.2 eV. The solar cells reach efficiencies up to 0.09% for MAGeI$_3$ and 0.13% for CsGeI$_3$, respectively. Solar cells with the active material FAGeI$_3$ did not show diode characteristics. Furthermore, this material also showed the highest band gap (2.16 eV).

In order to improve the stability of pure germanium perovskites, mixed cations (MA$^+$, FA$^+$, Cs$^+$) and mixed halides (I$^-$, Br$^-$) were introduced into the pure perovskite structure (see *Table 5*). The use of several cations, such as MA and FA, stabilized the FAPbI$_3$ perovskite for lead perovskites and increased the efficiency of solar cells from 13 to over 18%.[127] Lee et al significantly improved photo and moisture stability by partially replacing the FA$^+$ cation with Cs$^+$ (FA$_{0.9}$Cs$_{0.1}$PbI$_3$).[128] 2016 Graetzel et al. presented a

new triple cation type perovskite $Cs_x(MA_{0.17}FA_{0.83})_{(1-x)}Pb(I_{0.83}Br_{0.17})_3$, which in addition to the high efficiency also showed good phase stability.[129] Mixed germanium perovskites with tri-cation and dual anion show significantly higher efficiencies, but the stability was only minimally improved.

Table 5. Parameters including best solar cell, mean values and standard deviations of the solar cells prepared with mixed cations (MA^+, FA^+, Cs^+) and mixed halides (I^-, Br^-) in the $AGeX_3$ absorber layer.

Perovskite	V_{OC} / mV	J_{SC} / mA/cm²	FF	PCE / %
$MA_{0.95}Cs_{0.05}GeI_3$	435	2.15	40.50	**0.37** (max.)
	429 ± 8	2.17 ± 0.04	39.68 ± 1.25	0.35 ± 0.01
$MA_{0.9}Cs_{0.1}GeI_3$	451	2.06	39.83	**0.37** (max.)
	451 ± 0.1	2.02 ± 0.04	39.26 ± 0.54	0.35 ± 0.01
$MA_{0.8}Cs_{0.2}GeI_3$	451	1.77	36.01	**0.29** (max.)
	451 ± 0.1	1.76 ± 0.07	35.22 ± 0.78	0.28 ± 0.01
$MA_{0.9}FA_{0.1}GeIBr$	498	1.44	37.70	**0.27** (max.)
	459 ± 18	1.12 ± 0.32	34.93 ± 2.93	0.18 ± 0.03
$MA_{0.9}Cs_{0.1}GeIBr$	451	2.12	41.67	**0.39** (max.)
	451 ± 0.1	2.12 ± 0.02	39.99 ± 1.21	0.38 ± 0.01
$FA_{0.9}Cs_{0.1}GeIBr$	482	1.04	34.60	**0.17** (max.)
	425 ± 50	0.94 ± 0.09	29.47 ± 4.48	0.12 ± 0.05
$Cs_{0.08}MA_{0.15}FA_{0.77}Ge(I_{0.94}Br_{0.06})_3$	455	0.87	74.29	**0.29** (max.)
	444 ± 40	1.06 ± 0.14	56.40 ± 9.24	0.26 ± 0.02
$MA_{0.15}FA_{0.85}Ge(I_{0.94}Br_{0.06})_3$	529	1.40	44.75	**0.33** (max.)
	472 ± 40	1.17 ± 0.32	$36,90 \pm 5.11$	0.21 ± 0.09
$Cs_{0.05}MA_{0.15}FA_{0.77}Ge(I_{0.94}Br_{0.06})_3$	561	1.43	45.46	**0.38** (max.)
	561 ± 0.1	1.41 ± 0.03	44.88 ± 0.49	0.35 ± 0.02
$Cs_{0.10}MA_{0.15}FA_{0.77}Ge(I_{0.94}Br_{0.06})_3$	514	1.14	40.08	**0.23** (max.)
	498 ± 16	1.12 ± 0.02	36.16 ± 6.42	0.20 ± 0.04
$Cs_{0.15}MA_{0.15}FA_{0.77}Ge(I_{0.94}Br_{0.06})_3$	560	1.46	45.54	**0.37** (max.)
	561 ± 0.1	1.43 ± 0.03	45.28 ± 0.79	0.36 ± 0.01
$Cs_{0.20}MA_{0.15}FA_{0.77}Ge(I_{0.94}Br_{0.06})_3$	560	1.48	44.52	**0.37** (max.)
	560 ± 0.1	1.47 ± 0.02	43.69 ± 0.82	0.36 ± 0.01

5.3 Enhanced Performance of Germanium Halide Perovskite Solar Cells through Compositional Engineering

Enhanced Performance of Germanium Halide Perovskite Solar Cells through Compositional Engineering

Indira Kopacic,[1] Bastian Friesenbichler,[1] Sebastian F. Hoefler,[1] Birgit Kunert,[2] Harald Plank,[3] Thomas Rath,[1,*] Gregor Trimmel[1]

[1] Institute for Chemistry and Technology of Materials (ICTM), NAWI Graz, Graz University of Technology, Stremayrgasse 9, 8010 Graz, Austria

[2] Institute of Solid State Physics, Graz University of Technology, Petersgasse 16, 8010 Graz, Austria

[3] Institute for Electron Microscopy and Nanoanalysis, Graz University of Technology & Centre for Electron Microscopy Graz, Steyrergasse 17, 8010 Graz, Austria

ACS Publications
Most Trusted. Most Cited. Most Read.

ABSTRACT

Germanium halide perovskites are an attractive alternative to lead perovskites because of their well-suited optical properties for photovoltaic applications. However, the power conversion efficiencies of solar cells based on germanium perovskites has remained below 0.2% so far and also device stability is an issue. Herein, we present that modifying the chemical composition of the germanium perovskite, i.e. introducing bromide ions into the methylammonium germanium iodide perovskite, leads to a significant improvement of the solar cell performance along with a slight enhancement of the stability of the germanium perovskite. By substituting 10% of the iodide with bromide, power conversion efficiencies up to 0.57% were obtained in $MAGeI_{2.7}Br_{0.3}$ based solar cells with a planar p-i-n architecture using PEDOT:PSS as hole and $PC_{70}BM$ as electron transport layer.
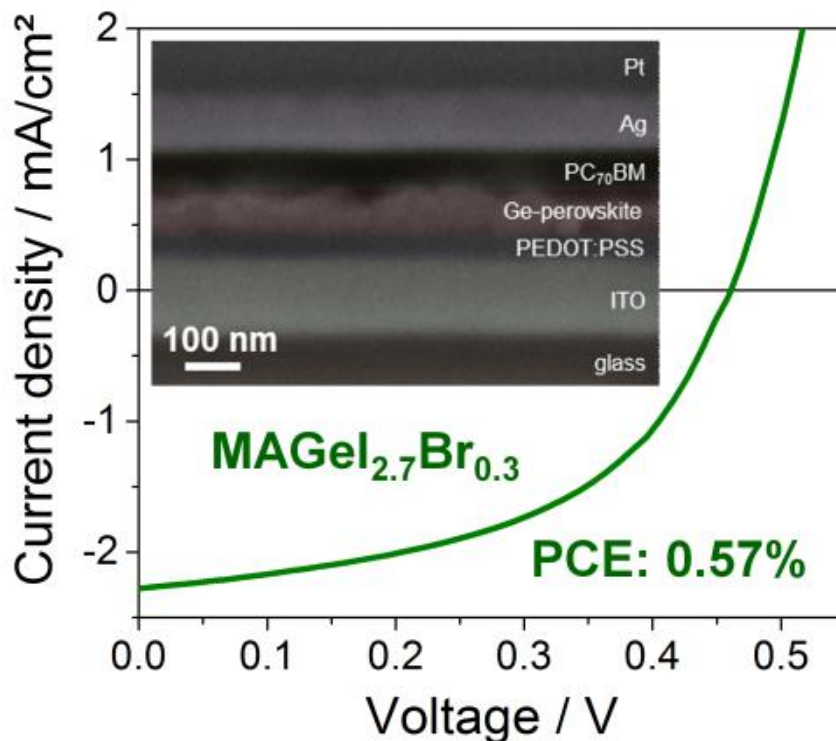
5.3.1 Introduction

Metal halide perovskites have garnered strong attention over the past several years due to their exciting properties for photovoltaic and other optoelectronic applications. Because of the toxicity issues of lead halide perovskites, which are so far the best performing compounds in this material class, there is now growing endeavor to study lead-free perovskite materials with regard to their photovoltaic properties.[57,130] Among lead-free perovskites, tin perovskites have been most thoroughly studied up to now and remarkable power conversion efficiencies (PCEs) up to 9% have recently been reported.[27,131] Germanium, which is like tin and lead, a group 14 element, is a further conclusive candidate for perovskite solar cells. In comparison to Pb^{2+}, Ge^{2+} exhibits a higher electronegativity, a more covalent character and an ionic radius (73 pm), which is smaller than the one of Pb^{2+} (119 pm). Interestingly, even though numerous theoretical studies attest that these materials have promising properties for solar cell applications,[85,86,87] germanium halide perovskites have only been rarely investigated experimentally. This is most likely due to the instability of the Ge^{2+} ion towards oxidation to Ge^{4+}. Stoumpos et al. investigated a series of germanium halide perovskites with regard to their structural and optical properties and found that germanium perovskites crystallize in a trigonal crystal structure and possess suitable band gaps for solar cell applications (e.g. 1.9 eV for $MAGeI_3$, MA: methylammonium).[85] Furthermore, mixed tin and germanium halide perovskites were theoretically studied regarding applications in photovoltaics and small effective masses, as well as low exciton-binding energies, are predicted for these compounds.[132]

Germanium perovskite solar cells were first reported in 2015 by Krishnamoorthy et al.[90] $CsGeI_3$ based solar cells led to a PCE of 0.11%, while a PCE of 0.2% was obtained using $MAGeI_3$ as absorber layer. There are no further reports on germanium perovskite solar cells published so far besides one patent application in which PCEs of 3% are claimed, however, only very limited data is provided.[90] For $CsGeI_3$, a theoretically maximum PCE of 27.9% was calculated using the Spectroscopic Limited Maximum Efficiency (SLME) mathematical model.[93]

We took this as an incentive to investigate the photovoltaic performance and the stability of germanium halide perovskites and found that by partly substituting iodide with bromide, the perovskite $MAGeX_3$ (X = I, Br) becomes less prone to degradation and also the performance in solar cells is significantly improved.

In this study, the germanium halide perovskites were synthesized from GeI_2, MAI and MABr, respectively. DMF was used as solvent for the precursor solution. After spin coating this solution (including an anti-solvent dripping step), the film was tempered at 70 °C for 10 min to form the perovskite thin film. This is in contrast to previous reports on the synthesis of germanium halide perovskites,[85,90] in which GeO_2 was used as the germanium source.

The introduction of bromide into the crystal structure was done via MABr, whereby we could vary the amount of bromide as X-site anion from 0% ($MAGeI_3$) to 33% ($MAGeI_2Br$). A further increase of the bromide content, which we attempted to realize by partly exchanging GeI_2 with $GeBr_2$, failed as no stable precursor solutions containing $GeBr_2$ could be obtained.

5.3.2 Results and Discussion

The X-ray diffractograms of the prepared germanium perovskites are depicted in **Figure 26A**. The obtained patterns are typical for an ABX_3 perovskite structure and very similar to the ones observed for $MAPbI_3$ or $MASnI_3$.[133,134] The main peaks of the simulated diffraction pattern for trigonal $MAGeI_3$ (based on single crystal X-ray diffraction data reported by Stoumpos et al.[85]) at 14.3°, 25.4° and 29.0° 2θ match well with the measured diffraction peaks of the prepared thin films. It is also clearly visible in **Figure 26B** that the peaks shift to higher 2θ values with increasing bromide content indicating a contraction of the unit cell. However, from the diffraction data it can be concluded that there is no change in the crystal structure in the investigated series of samples up to a bromide content of 33%. The peak at approx. 18.6° 2θ (marked with an asterisk) is only present upon addition of bromide, which correlates with findings for MASnI,Br perovskites.[134]

The optical band gaps of the perovskites (extracted from the absorption onset) range between 2.0 eV for $MAGeI_3$ and 2.1 eV for $MAGeI_2Br$ with a continuous hypsochromic shift of the absorption onset with increasing bromide content (see **Figure 26C**). The absorption maximum of the materials is found between 480 and 520 nm, and the slight increase of the curve at energies below the band gap can be most likely ascribed to scattering effects due to the comparably rough surfaces of the films.
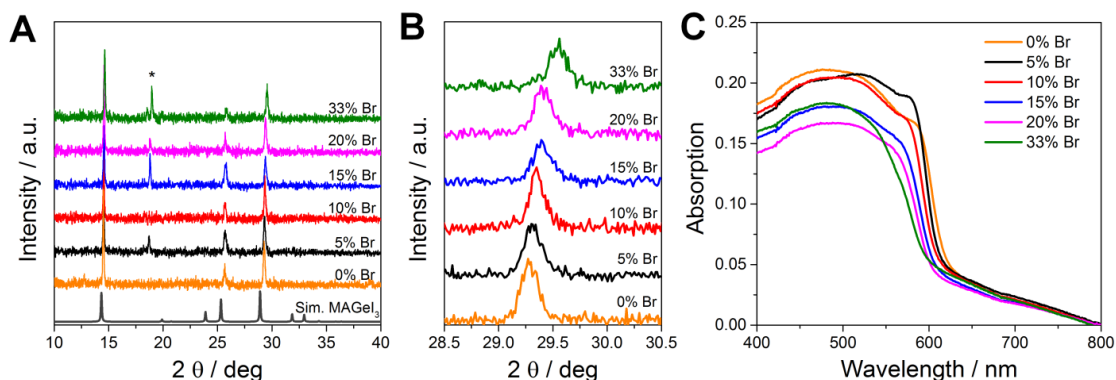
Figure 26. (A) X-ray diffraction patterns of the prepared methylammonium germanium halide perovskites with different Br-content and a simulated diffraction pattern for $MAGeI_3$ based on single crystal X-ray data published by Stoumpos et al. [85], (B) magnification of the area between 28.5° and 30.5° 2 θ and (C) UV-Vis spectra of the prepared germanium perovskite thin films.

The absorption data of the germanium perovskites were also exploited to evaluate the stability of the perovskite films under ambient conditions. Therefore, the films were taken out of the nitrogen filled glovebox and absorption spectra were acquired over 24 h while the films were exposed to ambient air. As shown in *Figure 27*, the absorption of the $MAGeI_3$ decreases much faster than that of the $MAGeI_{2.7}Br_{0.3}$ layer. In the $MAGeI_{2.7}Br_{0.3}$ sample, 65% of its initial absorption at 510 nm are retained, while in the $MAGeI_3$ film only 32% of the absorption at the start of the experiment are left. This improved ambient stability of the bromide containing germanium perovskite correlates well with the lifetimes of the prepared solar cells. While the $MAGeI_3$ based solar cells completely lost their performance within a few hours, even under inert conditions, the degradation of the $MAGeI_{2.7}Br_{0.3}$ was retarded. Also for $MAPbX_3$ (X = I, Br) lead perovskite solar cells, an improved stability was obtained by partly substituting the X-site anion from iodide to bromide, which was ascribed to a more compact and stable crystal structure by the reduction of the lattice constant concomitant with a transition from a pseudocubic to a cubic phase.[135]
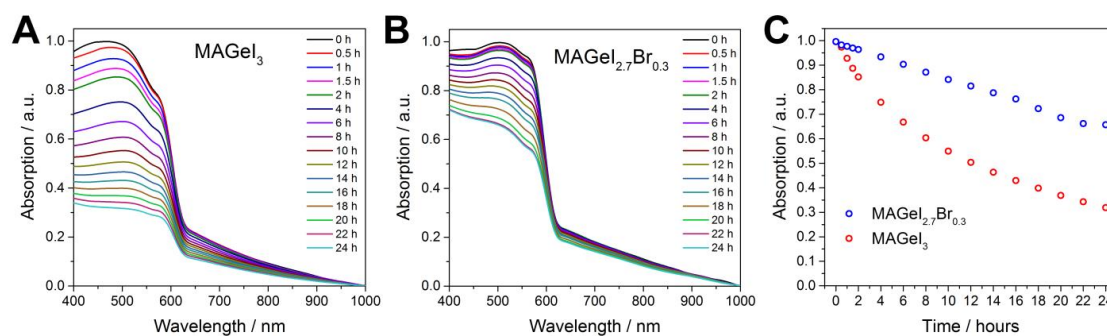
Figure 27. Time-resolved UV-Vis measurements to probe the ambient stability of the germanium perovskite samples (A: $MAGeI_3$; B: $MAGeI_{2.7}Br_{0.3}$) and the absorption intensity at 510 nm plotted versus time (C).

To examine the photovoltaic properties of the methylammonium germanium halide perovskites with different bromide content, photovoltaic devices were prepared in the "organic" p-i-n solar cell architecture using PEDOT:PSS as hole transport layer (HTL) and $PC_{70}BM$ as electron transport layer (ETL). This device setup turned out to be advantageous compared to the classic architecture using mesoporous TiO_2 thin films. The results are summarized in *Figure 28* (and

Table S 1) and typical JV curves are shown in *Figure S 1*. The mean values of the photocurrents range between 2.3 and 2.5 mA/cm² in all samples, except for the solar cells prepared with the germanium perovskite with a bromide content of 33% (MAGeI$_2$Br), which have a lower J_{SC} around 1.9-2.0 mA/cm². The photovoltage increases continuously with higher bromide content due to the widening of the optical band gap (c.f. *Figure 26*). MAGeI$_3$ based solar cells reveal a V_{OC} of 345 mV, while V_{OC}s above 500 mV could be obtained for solar cells with a MAGeI$_2$Br absorber layer. The fill factors are between 0.35 and 0.50. Overall, the PCEs of the solar cells increase up to a Br-content of 10%, from whereon the mean values are quite constant at around 0.45%. Therefore, we chose to use the germanium perovskite with 10% bromide (MAGeI$_{2.7}$Br$_{0.3}$) for further optimization. Compared to the study by Krishnamoorthy et al.[90], in which the CsGeI$_3$ and MAGeI$_3$ based solar cells have been prepared using mesoporous TiO$_2$ as ETL and spiro-OMeTAD as HTL, the V_{OC} obtained for MAGeI$_3$ based solar cells in this work is considerably higher (345 mV compared to 150 mV). The increased V_{OC} of the solar cells in the present study might be due to the new preparation method for the germanium perovskite, which might lead to improved defect chemistry.[87] Moreover, a very low water and oxygen content in the glovebox atmosphere (<0.1 ppm) was essential to obtain functioning solar cells.
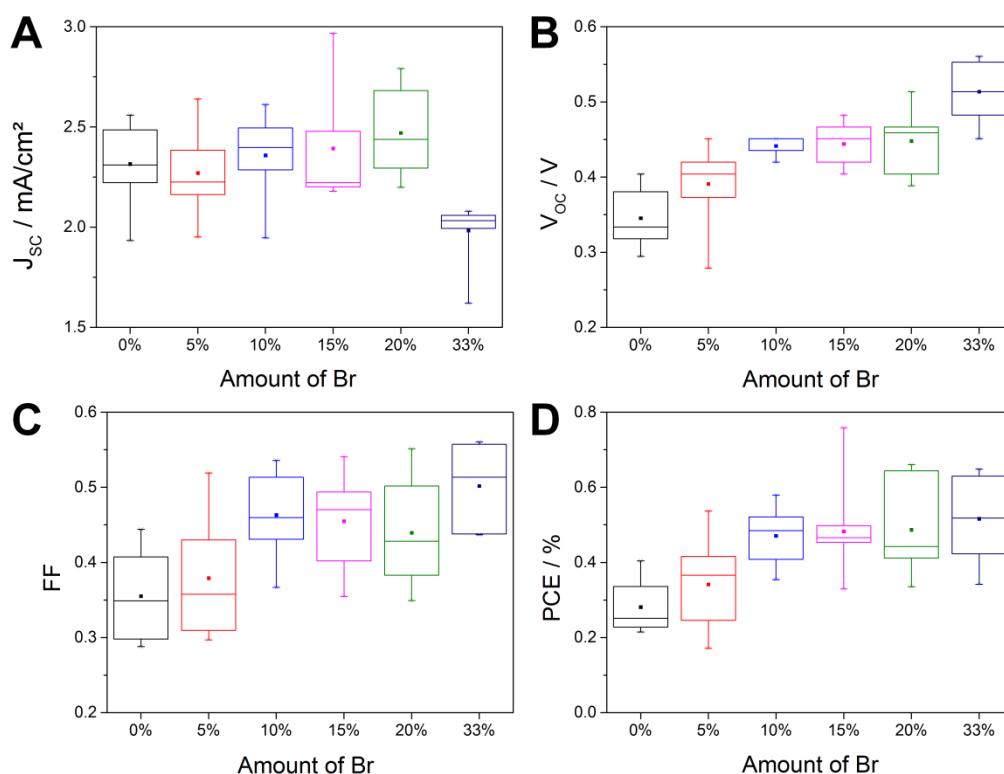
Figure 28. Characteristic parameters of the prepared solar cells depending on the amount of Br as X-site anion in MAGeX$_3$ (X = I, Br). The best solar cells (minimum eight) of each absorber layer composition were considered for calculating the statistics (see *Figure S 1*).

By fine-tuning the thicknesses of the PEDOT:PSS, the germanium perovskite absorber layer and the $PC_{70}BM$ ETL, the PCE of the $MAGeI_{2.7}Br_{0.3}$ perovskite solar cells could be further improved to 0.68% (measured without shadow mask). A measurement with a 2.9 x 2.9 mm² shadow mask led to a PCE of 0.57%. *Figure 29A* shows a cross sectional SEM image of this device prepared using the focused ion beam (FIB) technique. The different layers in the solar cell stack (glass/ITO/PEDOT:PSS/$MAGeI_{2.7}Br_{0.3}$/$PC_{70}BM$/Ag) can be clearly recognized and appear very flat and homogenous. Only the germanium perovskite layer with a thickness of approx. 85 nm discloses some roughness, however, the $PC_{70}BM$ layer on top (70 nm) levels that out leading again to a smooth interface of the $PC_{70}BM$ layer to the silver electrode (100 nm). The ITO layer is 130 nm thick, the PEDOT:PSS layer has a thickness of 40 nm and the Pt layer was deposited as protection layer before the FIB-preparation of the cross section.
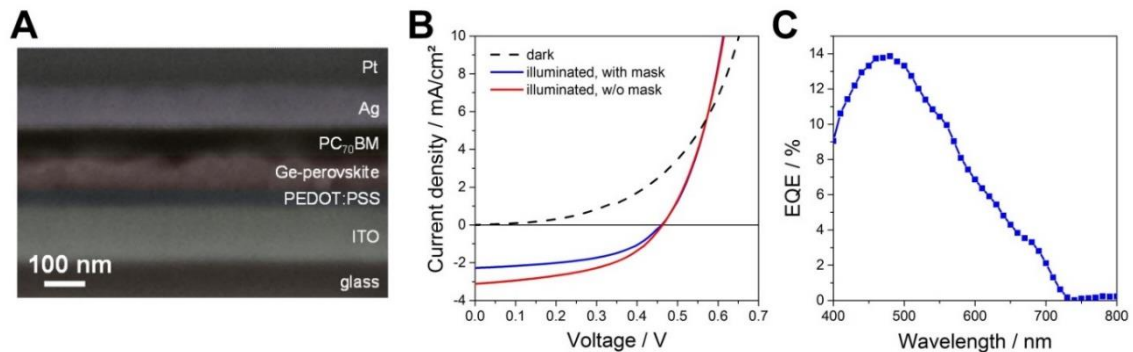
Figure 29. (A) SEM image of a FIB processed cross-section, (B) JV curves measured in the dark and under 100 mW/cm² illumination with and without 2.9 x 2.9 mm² shadow mask and (C) an EQE spectrum of an optimized $MAGeI_{2.7}Br_{0.3}$ based solar cell.

The JV curves measured in the dark and under 100 mW/cm² illumination are plotted in *Figure 29B*. The V_{OC} of this solar cell is 460 mV, the J_{SC} is 3.11 mA/cm² and the FF lies at 0.48, which results in a PCE of 0.68%. The series and shunt resistance of this solar cell are 30 Ω cm² and 0.7 kΩ cm², respectively. When measured with a shadow mask, the PCE decreases to 0.57%, which is based on a reduction of the J_{SC} to 2.43 mA/cm². The FF slightly improves to 0.51 and the V_{OC} is unaffected by the illumination through the shadow mask.

The hysteresis is not very pronounced in this type of solar cell, as can be seen from the JV curves of a similarly prepared solar cell measured in forward and backward direction

(see **Figure S2**). The corresponding characteristic device parameters are summarized in **Table S 2**.

The EQE spectrum of a $MAGeI_{2.7}Br_{0.3}$ based solar cell is presented in **Figure 29C**. The maximum in the EQE spectrum is slightly below 500 nm, which is in good agreement with the absorption properties of the germanium halide perovskites (c.f. **Figure 26C**). The onset of photocurrent generation is, however, already at 720 nm. This suggests also that the ETL $PC_{70}BM$ is partly contributing to the current generation, as the absorption onset of $PC_{70}BM$ is exactly in this wavelength range. A steeper increase of the EQE spectrum can be recognized at around 610 nm, which correlates with the absorption onset of $MAGeI_{2.7}Br_{0.3}$. To investigate the contribution of the ETL, reference solar cells without the $MAGeI_{2.7}Br_{0.3}$ layer were prepared to give devices with a photovoltage of 357 mV and a J_{SC} below 0.1 mA/cm² (**Figure S3**, **Table S3**).

The JV characteristics and device parameters of the $MAGeI_{2.7}Br_{0.3}$ based solar cell used for the measurement of the EQE spectrum are shown in **Figure S 4** and **Table S 4**. After the EQE measurements, which were performed in a sealed measuring box, the device revealed a J_{SC} of 1.9 mA/cm^2 and a PCE of 0.21%, while the PCE was 0.57% when measured directly after preparation. The loss of almost two thirds of the initial performance within several hours after the preparation also exemplifies the stability issue of the germanium perovskite based solar cells, even though the addition of bromide had slightly increased the stability of this material. Thus, addressing the stability issue of this class of materials will be inevitable in future research. In analogy to tin perovskites, the formation of 2D perovskites by the addition of bulky cations like PEA^+ (phenethylammonium) might be a promising approach.[73]

Acknowledgment

5.3.3 Conclusion

In summary, we could show that the bromide content in methylammonium germanium halide perovskites plays an important role in their performance in photovoltaic devices. Solar cells with PCEs of 0.57% could be obtained with a $MAGeI_{2.7}Br_{0.3}$ absorber layer. Even though the step forward in PCE with this material is encouraging, the stability of the devices remains a crucial issue, which will be tackled in further studies.

5.3.4 Experimental Section

Sample and solar cell preparation:

MAI and MABr (Dyesol), GeI_2 (99.99%, ABCR), PEDOT:PSS (Clevios P VP.Al 4083, Heraeus), and $PC_{70}BM$ (99.5%, Solenne BV) were used as received.

A 1 M precursor solution of $MAGeI_{3-x}Br_x$ was prepared by dissolving MAI, MABr and GeI_2 with the amount of bromide as X-site anion with x = 0, 0.15, 0.30, 0.45, 0.60, and 1, respectively, in dry DMF. The solution was stirred for 24 h at room temperature in N_2 atmosphere in a glovebox. Before use, the precursor solution was filtered through a 0.45 µm PTFE filter.

ITO coated glass substrates (15 x 15 mm, 15 Ω/sq, purchased from Lumtec) were carefully rinsed with acetone and put into an isopropanol bath followed by sonication for 30 min at 40 °C. Subsequently, the substrates were dried under an N_2 gas stream and treated with oxygen plasma for 3 min. As first layer, a PEDOT:PSS film was spin coated at 6000 rpm for 30 s and the substrates were put into a glovebox immediately afterwards for a temperature treatment at 120 °C for 20 min. Next, the precursor solution was spin coated onto the PEDOT:PSS film in glovebox atmosphere with the following spin coating conditions: 4000 rpm, 1000 rpm/s, 30 s. After 10 s of spinning, chlorobenzene was dropped onto the rotating substrate, whereupon the color of the film changed from yellow to orange/red. Afterwards, the perovskite was tempered at 70 °C for 10 min. A $PC_{70}BM$ solution in dry chloroform (50 mg/mL) was spin coated on top of the perovskite layer with 1000 rpm, 500 rpm/s for 30 s. Ag electrodes (3 x 3 mm²) were deposited by thermal evaporation at a rate of 2 Å/s at a base pressure below $1x10^{-5}$ mbar.

For (time-resolved) UV-Vis measurements, the perovskite films were prepared on glass substrates in the same way as described above. The UV-Vis measurements were taken

(and the time resolved measurements were started) immediately after taking the samples out of the nitrogen filled glovebox.

Characterization techniques:

X-ray diffraction measurements were conducted on a PANalytical Empyrean diffractometer in Bragg-Brentano configuration operated at 40 kV and 40 mA using Cu K_α radiation. For the XRD measurements, the perovskite films were prepared on glass slides and covered with a thin PMMA protection layer, spin coated from a chlorobenzene solution (10 mg/mL). UV-Vis spectra were acquired with a Perkin Elmer Lambda 35 UV-Vis spectrometer equipped with an integrating sphere.

JV curves were recorded in a glovebox using a Keithley 2400 source measure unit and a custom made LabView software. The samples were illuminated by a Dedolight xenon lamp with a spectrum similar to the AM 1.5G spectrum at 100 mW/cm^2. The EQE spectra were measured using monochromatic light from a MuLTImode4 monochromator (AMKO) equipped with a 75 W Xenon lamp chopped at 30 Hz. The signals (wavelength increment: 10 nm) were measured by a lock-in amplifier from Stanford Research Systems (Model SR830). A spectrally calibrated 818-UV/DB photodiode (Newport Corporation) was used as a reference. A sealed measuring box with a quartz glass window was used to protect the solar cells against ambient atmosphere during the EQE measurement.

The cross section of the solar cell was prepared via the focused ion beam (FIB) technique using a FEI NOVA 200 FIB/SEM dual beam system with multiple current approaches to minimize spatial sample damage. SEM imaging was done in low dose conditions to minimize e-beam related material alteration.

ASSOCIATED CONTENT

Supporting Information. Additional JV curves and solar cell data.

AUTHOR INFORMATION

ORCID

Sebastian F. Hoefler: 0000-0003-1038-5082

Harald Plank: 0000-0003-1112-0908

Thomas Rath: 0000-0002-4837-7726

Gregor Trimmel: 0000-0001-8922-4163

Notes

The authors declare no competing financial interest.

Supporting Information

Enhanced Performance of Germanium Halide Perovskite Solar Cells through Compositional Engineering

Indira Kopacic,[1] Bastian Friesenbichler,[1] Sebastian F. Hoefler,[1] Birgit Kunert,[2] Harald Plank,[3] Thomas Rath,[1,] Gregor Trimmel[1]*

[1] Institute for Chemistry and Technology of Materials (ICTM), NAWI Graz, Graz University of Technology, Stremayrgasse 9, 8010 Graz, Austria

[2] Institute of Solid State Physics, Graz University of Technology, Petersgasse 16, 8010 Graz, Austria

[3] Institute for Electron Microscopy and Nanoanalysis, Graz University of Technology & Centre for Electron Microscopy Graz, Steyrergasse 17, 8010 Graz, Austria

Corresponding Author
* E-mail: thomas.rath@tugraz.at

Table S 1. Parameters including mean values and standard deviations of the solar cells prepared with different Br-content in the $MAGeX_3$ (X = Br, I) absorber layer. This data is presented graphically using box plots in *Figure 28*.

Br-content	V_{OC} / V	J_{SC} / mA/cm²	FF	PCE / %
0% Br	0.326	2.41	0.32	0.25
	0.310	2.56	0.29	0.23
	0.294	2.56	0.29	0.21
	0.357	2.18	0.38	0.29
	0.341	1.93	0.39	0.25
	0.404	2.27	0.43	0.38
	0.404	2.29	0.44	0.40
	0.326	2.33	0.31	0.23
	0.345 ± 0.038	2.32 ± 0.19	0.36 ± 0.06	0.28 ± 0.07
5% Br	0.357	2.20	0.31	0.25
	0.404	2.64	0.35	0.36
	0.451	2.60	0.40	0.46
	0.279	2.04	0.30	0.17
	0.310	1.95	0.30	0.18
	0.420	2.38	0.38	0.37
	0.451	2.35	0.52	0.54
	0.435	2.22	0.44	0.41
	0.404	2.24	0.36	0.32
	0.388	2.42	0.49	0.45
	0.388	2.10	0.35	0.28
	0.373	2.18	0.30	0.24
	0.420	2.16	0.43	0.39
	0.391 ± 0.049	2.27 ± 0.19	0.38 ± 0.07	0.34 ± 0.11
10% Br	0.435	2.52	0.44	0.48
	0.451	2.24	0.51	0.51
	0.451	2.38	0.54	0.56
	0.435	2.43	0.37	0.38
	0.451	2.56	0.46	0.52
	0.435	2.61	0.38	0.43
	0.435	2.41	0.39	0.40
	0.451	2.49	0.53	0.58
	0.451	2.40	0.53	0.56
	0.451	2.29	0.49	0.50
	0.435	2.28	0.43	0.41
	0.435	2.08	0.49	0.42
	0.420	1.95	0.45	0.35
	0.441 ± 0.010	2.36 ± 0.18	0.46 ± 0.06	0.47 ± 0.07

Continued Table S1

Br-content	V_{OC} / V	J_{SC} / mA/cm²	FF	PCE / %
	0.420	2.48	0.35	0.37
	0.404	2.85	0.40	0.45
	0.48	2.97	0.54	0.76
	0.451	2.19	0.47	0.47
15% Br	0.404	2.23	0.37	0.33
	0.451	2.21	0.48	0.47
	0.467	2.18	0.49	0.50
	0.451	2.20	0.46	0.46
	0.467	2.22	0.53	0.54
	0.444 ± 0.027	2.39 ± 0.29	0.46 ± 0.06	0.48 ± 0.11
	0.467	2.34	0.39	0.43
	0.404	2.58	0.35	0.37
	0.498	2.39	0.55	0.66
	0.514	2.48	0.51	0.65
	0.467	2.68	0.50	0.64
20% Br	0.388	2.79	0.38	0.41
	0.404	2.71	0.40	0.43
	0.420	2.23	0.37	0.34
	0.451	2.30	0.48	0.48
	0.467	2.20	0.46	0.45
	0.448 ± 0.040	2.47 ± 0.20	0.44 ± 0.06	0.49 ± 0.11
	0.482	2.03	0.44	0.42
	0.561	2.08	0.56	0.65
	0.451	1.96	0.47	0.42
33% Br	0.545	2.03	0.55	0.61
	0.482	2.03	0.44	0.42
	0.561	2.08	0.56	0.65
	0.545	2.04	0.55	0.61
	0.482	1.62	0.44	0.34
	0.514 ± 0.033	1.98 ± 0.35	0.50 ± 0.05	0.52 ± 0.15
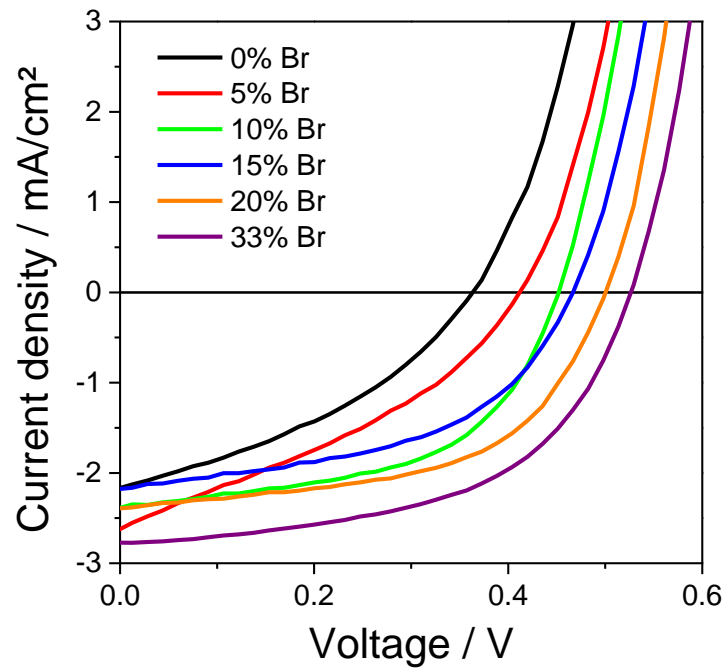
Figure S 1. Typical JV curves of MAGeX$_3$ (X = Br, I) based solar cells with different Br-content.
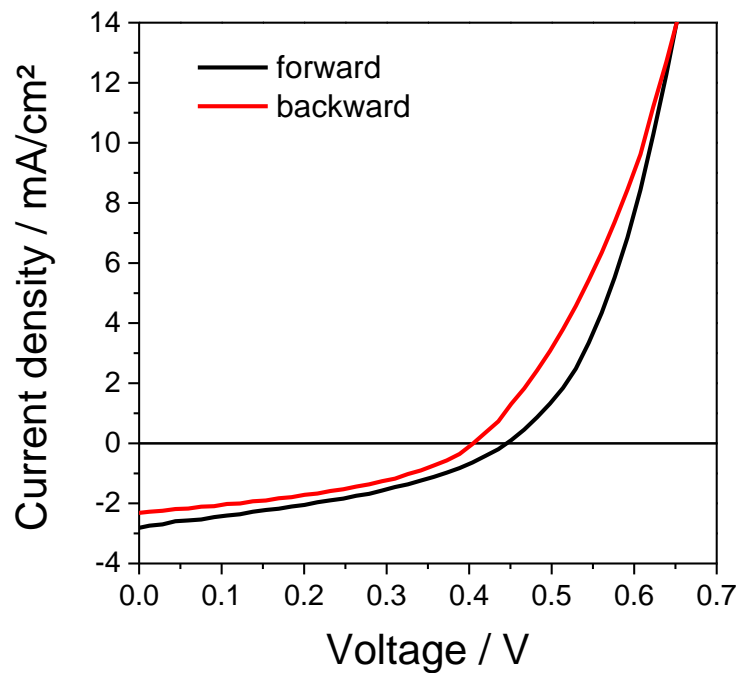
Figure S 2. JV curves of a germanium perovskite (MAGeI$_{2.7}$Br$_{0.3}$) solar cell measured in forward (0 V to 1.5 V) and backward (1.5 V to 0 V) scan direction with a scan rate of 150 mV/s.

Table S 2. Characteristic solar cell parameters extracted from the JV curves shown in *Figure S 2*.

scan direction	V_{OC} / V	J_{SC} /mA/cm²	FF	PCE / %
forward	0.451	2.83	0.37	0.47
backward	0.404	2.32	0.40	0.38
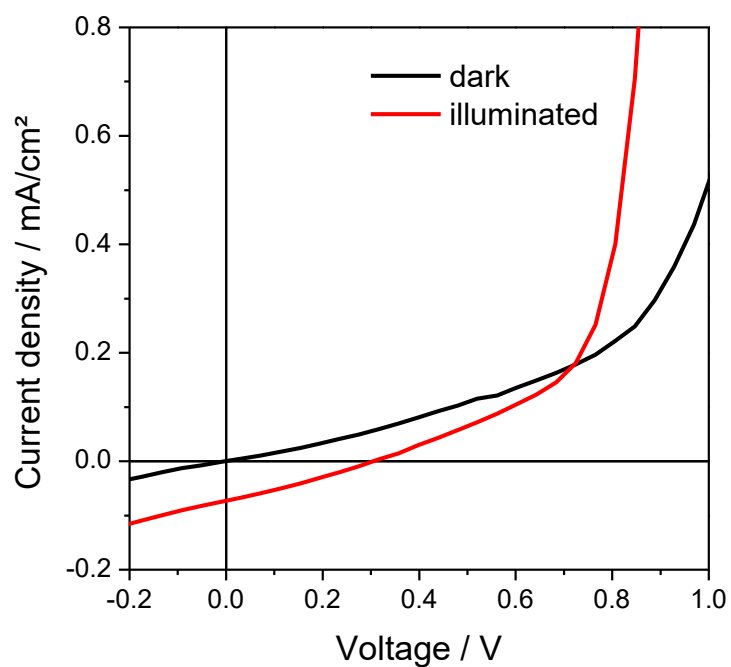
Figure S3. JV curves measured in the dark and under 100 mW/cm² illumination of an ITO/PEDOT:PSS/PC$_{70}$BM/Ag solar cell.

Table S3. Characteristic solar cell parameters extracted from the JV curves shown in *Figure S3*.

V_{OC} / V	J_{SC} / mA/cm²	FF	PCE / %
0.357	0.074	0.25	0.006
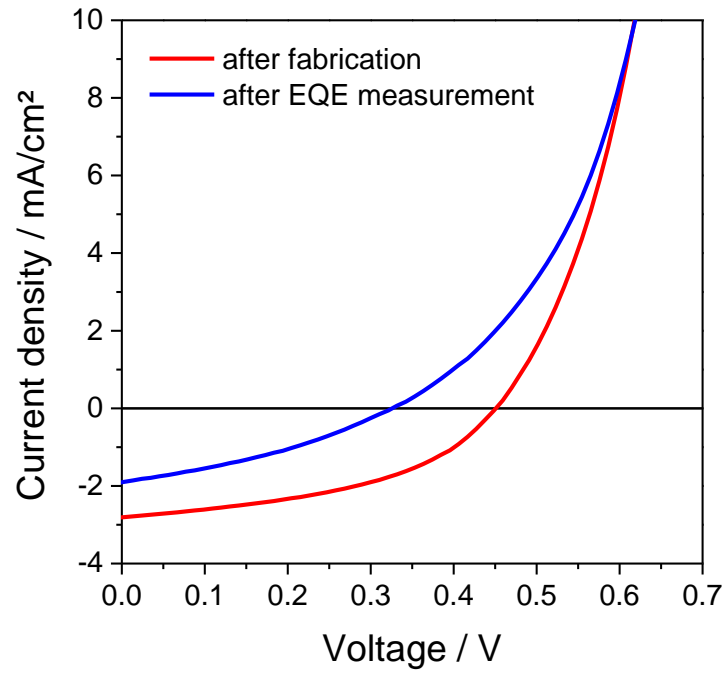
Figure S 4. JV curves of a MAGeI$_{2.7}$Br$_{0.3}$ perovskite based solar cell measured directly after fabrication as well as after encapsulation and the EQE measurements.

Table S 4. Characteristic solar cell parameters extracted from the JV curves shown in *Figure S4*.

	V_{OC} / V	J_{SC} / mA/cm²	FF	PCE / %
after fabrication	0.449	2.8	0.45	0.57
after EQE measurement	0.321	1.9	0.35	0.21

5.4 A Mixed-Cation Two-Dimensional (2D) / Three-Dimensional (3D) Germanium Halide Perovskite: Structural, Optical and Photovoltaic Properties

ABSTRACT

In this chapter, the synthesis and characterization of the low-dimensional mixed-cation germanium halide perovskite ($PEA_2MA_{n-1}Ge_nX_{3n+1}$) as a lead-free perovskite-type is presented. The optical, electronical and photovoltaic properties were discussed in comparison to the three-dimensional (3D) methylammonium germanium iodide bromide perovskite ($MAGeI_2Br$). The exchange of methylammonium (MA) with phenylethylammonium (PEA) cation during synthesis leads to the formation of a mixed-cation germanium halide perovskite with a lower dimensionality. The 3D perovskite structure was modified by changing the amount of PEA from 0, 10, 20, 30, 40 up to 50 mol%. The low-dimensional mixed 2D/3D perovskites demonstrate a significantly enhanced stability in the glovebox atmosphere compared to the three-dimensional perovskites. By substituting 40% of the MA cation with PEA, power conversion efficiencies up to 0.65% were obtained in solar cells with a planar p-i-n architecture (glass/ITO/PEDOT:PSS/Perovskite/$PC_{70}BM$/Ag).
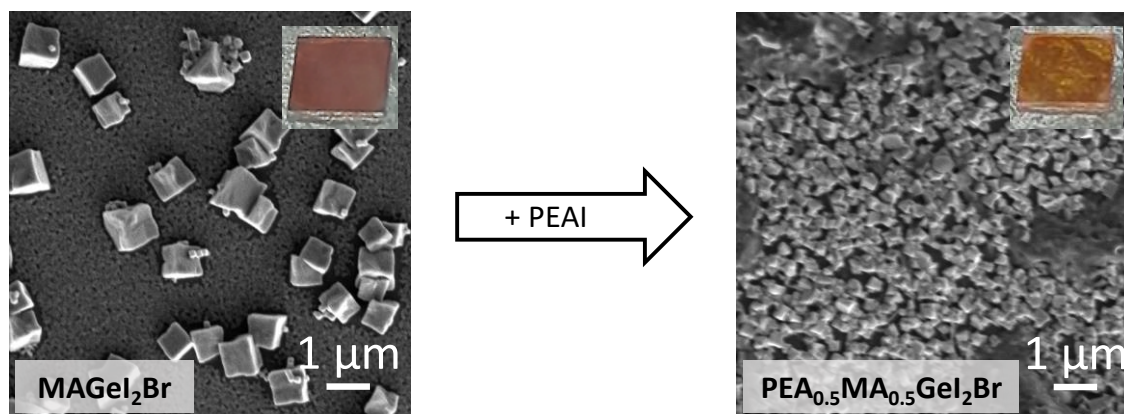
5.4.1 Introduction

As previously reported by other research groups and us, germanium, like tin and lead in group 14, is a promising candidate for the substitution of lead in the perovskite structure. The main disadvantage of germanium is that it easily oxidizes from Ge^{2+} to Ge^{4+}, which is probably why germanium halide perovskites are rarely experimentally investigated by research groups.[90,90] Such a problem of oxidation stability is already known from tin perovskites, but it is more remarkable with germanium perovskites because of the reduced effect of inert electron pairs.[65,85] This instability can lead to degradation of the perovskite structure and cause various defects that complicate the use of germanium perovskite materials in solar cells.

We improved the photovoltaic performance by modifying the chemical composition of the germanium perovskite, i.e. by introducing bromide ions into the methylammonium germanium iodide perovskite ($MAGeI_{3-x}Br_x$). This resulted in a significant improvement of the efficiency to 0.57% for a mixed-anion germanium perovskite with 10 mol% bromide ($MAGeI_{2.7}Br_{0.3}$). It was found that the incorporation of bromide improves the environmental stability. Such cognitions can be very helpful to promote the development of germanium perovskite solar cells.[100]

Germanium perovskite films decompose very quickly when exposed to the ambient atmosphere. In a nitrogen environment, the decomposition progresses more slowly. The main responsibility for perovskite decomposition is the adsorption of water and oxygen molecules on perovskites.[136,137,138,139]

The stability of a perovskite solar cell can be significantly improved by encapsulation.[140] However, it is essential to develop new strategies to increase the long-term stability of the devices.

In this work, a suitable stabilization method was used, which was already very successfully utilized when it comes to lead and tin perovskite materials.[141,142,143] A spacer cation (PEA$^+$= phenylethylammonium, $C_6H_5CH_2CH_2NH_3^+$) was added in different amounts to the 3D perovskite $MAGeI_2Br$ as an A-site cation, wherein the three-dimensional crystal structure is layered into a two-dimensional film. The partial substitution of methylammonium cation (MA, $CH_3NH_3^+$) in $MAGeI_2Br$ with the larger

PEA$^+$ cations resulted in the formation of mixed two-dimensional (2D) / three-dimensional (3D) perovskite with a lower dimensionality. In such 2D/3D mixed perovskites, the 3D perovskite structure (AGeX$_3$), with corner-sharing GeX$_6$ octahedra, is separated by 2D bilayers. The dimensionality of the perovskite structure can be tuned by changing the stoichiometric ratio from 0 mol% (3D perovskite structure) to 100 mol% PEA (2D perovskite structure).[11] In our case, the PEA$^+$-content in the perovskite film was examined from 0 to 50%. A higher PEA$^+$-content could not be achieved due to the poor layer formation during spin coating. All mixed 2D/3D perovskite materials were then examined for their structure and properties. It was found that the addition of the PEA$^+$ spacer cation has a positive influence on both the crystal formation of the perovskite and its lifetime.

Since only very limited data related to germanium perovskites are known and found in literature, the influence of the PEA$^+$-cation on the tin perovskites (see Chapter 2.2.1 Tin Based Perovskite Solar Cells) is discussed. Studies have shown that the addition of a very small amount of layered (2D) tin perovskite to 3D tin perovskite induces excellent crystallinity and orientation of the 3D FASnI$_3$ grains.[73,144,145]

The germanium halide perovskites were synthesized from GeI$_2$, MAI, MABr and a varying amount of phenylethylammonium iodide (PEAI) dissolved in DMF. During the spin coating process, an antisolvent (chlorobenzene) is dripped on the sample and the film was tempered at 70 °C for 10 min to form the perovskite thin film. Solar cells with a planar p-i-n architecture using PEDOT: PSS as a hole and PC$_{70}$BM as an electron transport layer were prepared (for details, see Experimental Details). As a result of the addition of PEA$^+$, the MAGeI$_2$Br perovskite is separated into 2D layers, the layers of germanium halide octahedra being cut into the cubic MAGeI$_2$Br along the (100) direction. The resulting cut layers are insulated by two layers of PEA. Changing the stoichiometric ratio of PEA to MA from 0% to 50% also changes the structural unit and the number of germanium halide layers.

5.4.2 Results and Discussion

The X-ray diffractograms of the simulated diffraction pattern for $MAGeI_3$ (based on single crystal X-ray data published by Stoumpos et al.[84]) and mixed 2D/3D (with 30% and 50% of PEAI) germanium halide perovskites are depicted in ***Figure 30A***. An XRD measurement of these samples was important to investigate the effects of PEA^+-cation on the crystal structure and the grains of the 3D $MAGeI_2Br$ perovskite, and these correspond well with the information about the crystal structure from the literature.[27,146] The main peaks of the trigonal $MAGeI_2Br$ at 14.3°, 25.4° and 29.0° 2 θ match well with the measured diffraction peaks of the prepared thin films (see chapter 5.2 for details). In this perovskite, the peak value of approx. 18.6° was measured and this is due to the incorporation of bromide in the crystal structure. Similar dominant diffraction peaks at 14.2°, 28.5°, 43.4° and 59.1°, which are assigned to the lattice planes (100, 200, 300 and 400), were found in the literature for mixed 2D/3D low-dimensional tin halide perovskite thin films.[27,73] The crystalline phases of $MAGeI_2Br$ are separated by organic interlayers composed of PEA^+ aromatic groups (spacer cation), arranged to each other.

By adding PEAI to the $MAGeI_2Br$ perovskite, a strong diffraction peak at 4° and a smaller diffraction peak at 7° appear in the films of the layers and remain there even with higher concentrations of PEAI. It is believed that these peaks may indicate the presence of the 2D perovskite phase, as similar observations were made in mixed perovskites of tin and lead.[147,148] In addition, it should be noted that with an increase in the PEAI content (2D perovskites), a decrease in the crystal intensity of $MAGeI_2Br$ was observed.[149]

In accordance with the XRD data for used educts depicted in ***Figure 30B***, it has been proven that all utilized components were embedded in the crystal structure.
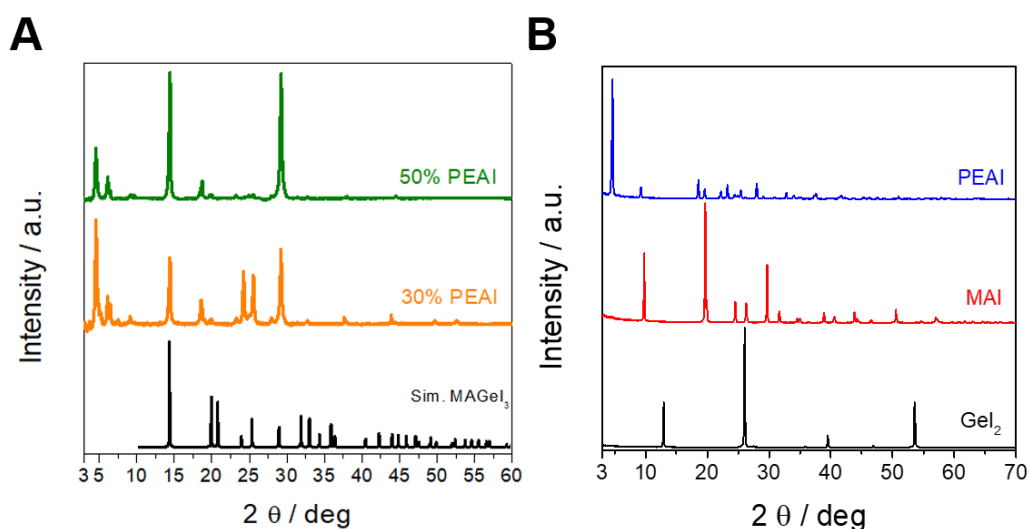
Figure 30. (A) X-ray diffraction patterns of the prepared methylammonium germanium halide perovskites (deposited on glass substrates) with different PEAI-content and a simulated diffraction pattern for $MAGeI_3$ based on single crystal X-ray data published by Stoumpos et al.[84] (B) X-ray diffraction patterns of the educts: GeI_2, MAI and PEAI (powder samples).

Optical properties of the mixed MA-PEA perovskites were derived from UV/Vis spectra. The absorption of the prepared perovskites shows a high absorption in the wavelength range up to 640 nm, which also matches well with the orange/red color of the perovskite layers (*Figure 31*). All samples have a good visible onset between 620 nm and 640 nm, where the absorption coefficient increases with the PEA-content, which may be due to the positive influence of PEA^+, which results in less rough layers.
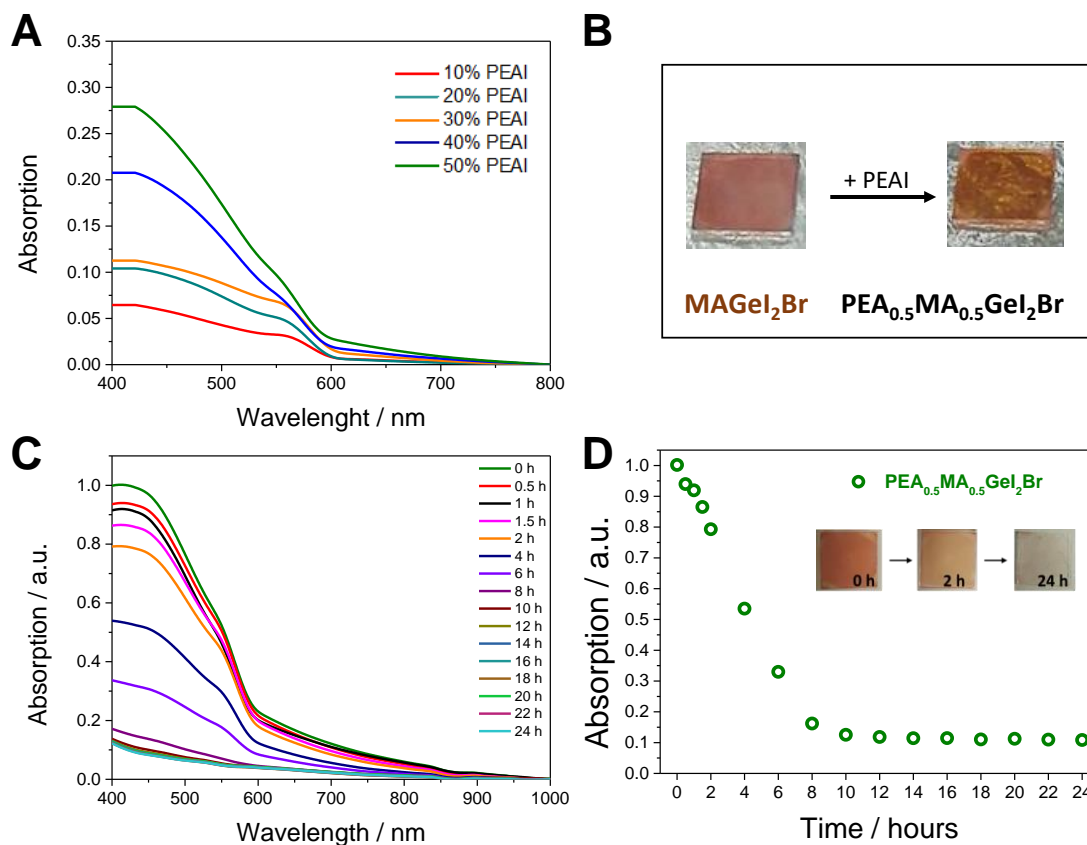
Figure 31. (A) UV-Vis spectra of the prepared germanium perovskite thin films (B) photos of the perovskite layers without (left) and with 50% PEAI (right) (C) time-resolved UV-Vis measurements to probe the ambient stability of the germanium perovskite samples ($PEA_{0.5}MA_{0.5}GeI_2Br$) and (D) the absorption intensity at 412 nm plotted versus time.

The optical band gaps of the perovskites (extracted from the absorption start) are approx. 2.1 eV to 2.15 eV for all mixed MA-PEA samples and 2.1 eV for $MAGeI_2Br$. Therefore, it can be said that there is no or only a slight shift in the absorption start with increasing PEA^+-content. The absorption spectra confirm also the formation of low-dimensional perovskite phases in the mixed MA-PEA samples. A pure 3D $MAGeI_2Br$ sample shows an absorption maximum between 480 and 520 nm, while the mixed MA-PEA samples shift the absorption maximum to lower wavelengths ~412 nm. Overall, the absorption has a slight increase, with increasing PEA^+-content, over the whole spectrum (see *Figure 31A*).

The change of the layer by addition of the organic cation can even be observed optically. *Figure 31B* shows a much more homogeneous and smoother layer by adding 50% PEAI.

To evaluate the stability of the perovskite films under ambient conditions, the absorption data of the germanium perovskites were also exploited. Therefore, the film was taken out of the nitrogen filled glovebox and absorption spectra were acquired over 24 h while the film was exposed to ambient air. For this study, the sample was taken with 50% PEAI as it showed the best performance. As shown in *Figure 31C*, the absorption of the mixed 2D/3D $PEA_{0.5}MA_{0.5}GeI_2Br$ perovskites decreases very quickly. After only 4 hours, the sample lost almost 50% of its initial absorption and after 10 hours the absorption was completely lost. The significantly poorer environmental stability of the new perovskites shows that the new mixed 2D/3D germanium halide perovskite is significantly more unstable from outside the glovebox compared to $MAGeI_3$ and $MAGeI_{2.7}Br_{0.3}$ perovskites (see *Chapter 5.3*, *Figure 26C*).

To examine the photovoltaic properties of the layered 2D/3D methylammonium germanium halide perovskites with different PEA$^+$-content, photovoltaic devices were prepared in the p-i-n solar cell architecture using PEDOT:PSS (as HTL) and $PC_{70}BM$ (as ETL). The typical JV curves of the best $PEA_xMA_{(1-x)}GeI_2Br$ based solar cells with different PEA$^+$-content are shown in *Figure 32A* and the characteristic solar cell parameters extracted from these JV curves results are summarized in *Table S5*. The mean values of the photocurrents range between 2.45 and 2.73 mA/cm² in all samples, except for the solar cells prepared with the germanium perovskite with a PEA$^+$-content of 10%, which have a lower J_{SC} around 1.8 mA/cm². $PEA_xMA_{(1-x)}GeI_2Br$ based solar cells with 10 and 20% PEA reveal a V_{OC} of 409 mV and 429 mV, while V_{OC}'s of 490 mV could be obtained for solar cells with 30% and 40% and 450 mV for 50% PEA film absorber layers. The filling factors are in the range of 0.38 and 0.51. The PCEs of the solar cells increase up to a PEA-content of 20%, from whereon the PCE values are quite constant at around 0.49% to 0.55%. The solar cell prepared with 40% PEA film gave the highest PCE value of 0.65%. The JV curves of the best peforming cell are depicted in *Figure 32B*. The green line illustrates the measurement under illumination and the black dotted line under dark conditions.
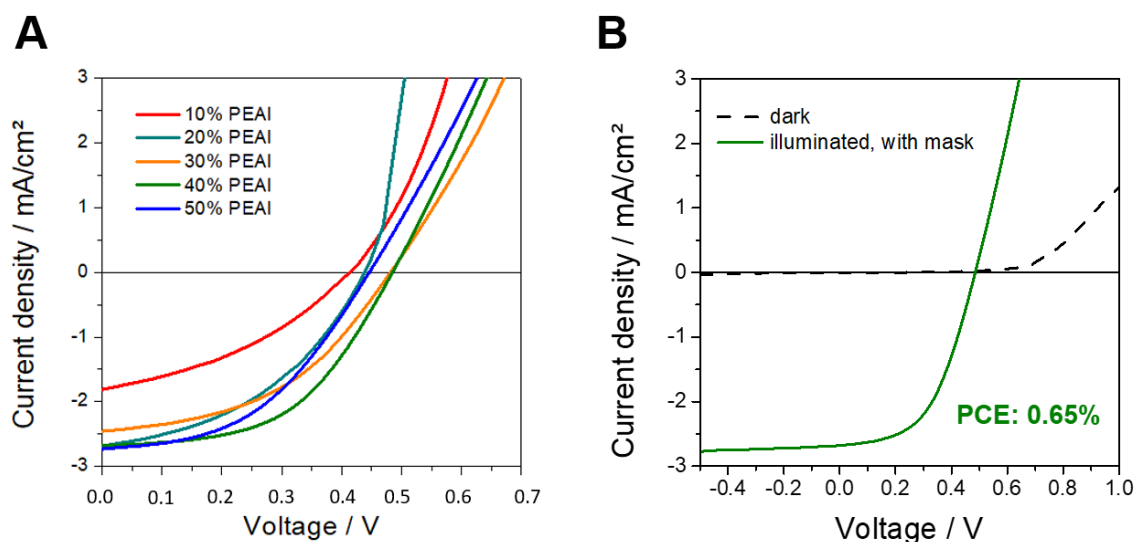
Figure 32. (A) JV curves of the best $PEA_xMA_{(1-x)}GeI_2Br$ based solar cells with different PEA^+-content (B) JV curve of the best performing perovskite solar cell with 40% PEA: green line giving the measurement under illumination and black dotted line giving the measurement under dark conditions.

Table 6. Characteristic solar cell parameters extracted from the JV curves shown in *Figure 32A*.

PEAI-Content	V_{OC} / V	J_{SC} / mA/cm²	FF	PCE / %
10%	0.409	1.80	0.38	0.27
20%	0.429	2.68	0.43	0.49
30%	0.490	2.45	0.44	0.53
40%	**0.490**	**2.68**	**0.51**	**0.65**
50%	0.450	2.73	0.45	0.55

The JV curves of 40% and 50% PEA solar cells, as well as a solar cell without PEA are shown in *Figure 33*. Solar cells with 40% and 50% PEA stabilized after the second measurement and lost performance only from the fourteenth day. In comparison, the solar cells without PEA lost their performance rapidly the next day (see *Figure 33C* and *Figure 33D* and *Table 7-9*). These results clearly show that the dimensional reduction from 3D $MAGeI_2Br$ to 2D/3D $PEA_xMA_{(1-x)}GeI_2Br$ perovskite significantly improves the stability and thus the oxidation breakdown of the perovskite effectively suppressed.
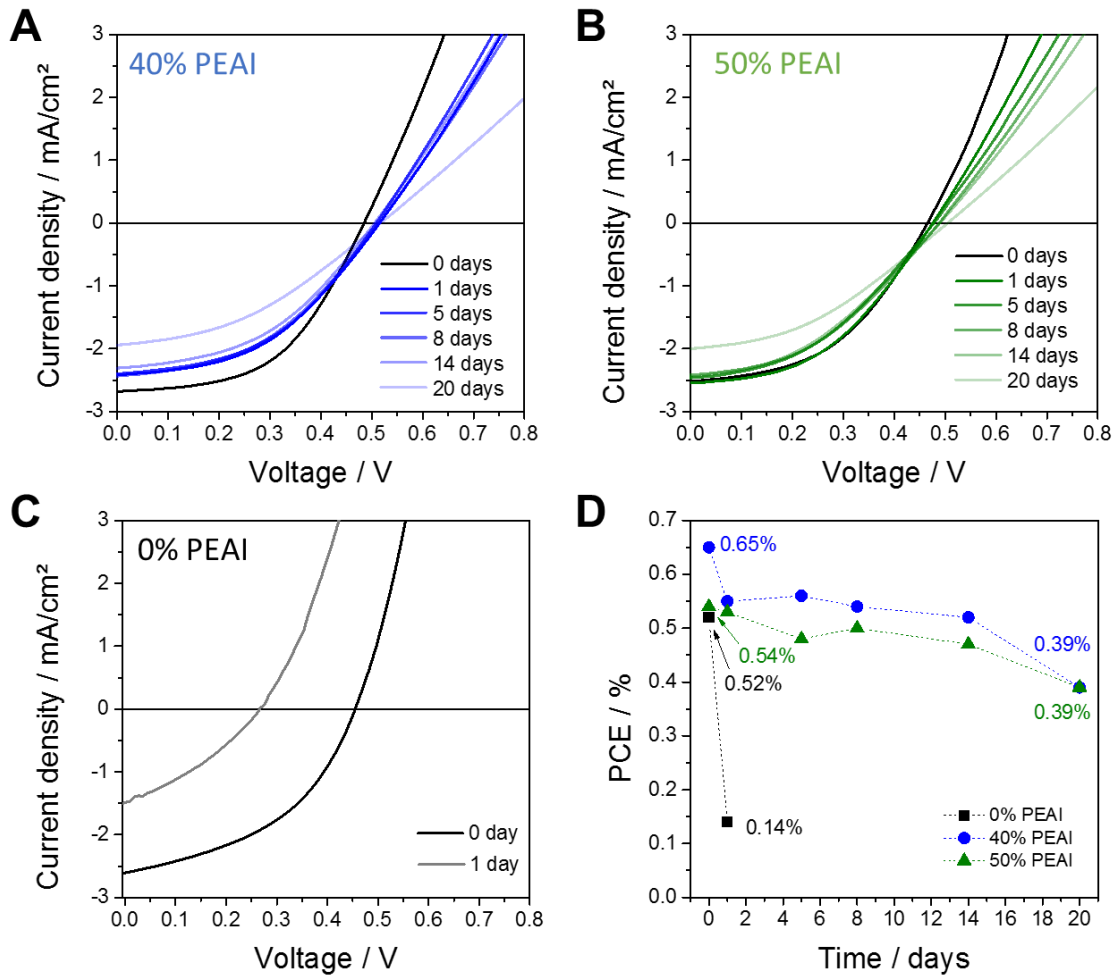
Figure 33. J-V curves (Stability test) of the best-performing solar cells with 40% (A) 50% (B) and 0% of PEAI and the PCE degradation with time (D).

Table 7. Characteristic solar cell (with 40% PEAI) parameters extracted from the JV curves shown in *Figure 33A*.

Days	V_{OC} / V	J_{SC} / mA/cm²	FF	PCE / %
0	0.490	2.68	0.51	0.65
1	0.510	2.41	0.46	0.55
5	0.510	2.42	0.46	0.56
8	0.510	2.45	0.44	0.54
14	0.510	2.33	0.44	0.52
20	0.530	1.96	0.38	0.39

Table 8. Characteristic solar cell (with 50% PEAI) parameters extracted from the JV curves shown in *Figure 33B*.

Days	V_{OC} / V	J_{SC} / mA/cm²	FF	PCE / %
0	0.470	2.52	0.46	0.54
1	0.470	2.54	0.45	0.53
5	0.490	2.48	0.40	0.48
8	0.490	2.44	0.41	0.50
14	0.490	2.47	0.39	0.47
20	0.510	2.02	0.39	0.39

Table 9. Characteristic solar cell (without PEAI) parameters extracted from the JV curves shown in *Figure 33C*.

Days	V_{OC} / V	J_{SC} / mA/cm²	FF	PCE / %
0	0.451	2.61	0.45	0.52
1	0.268	1.49	0.33	0.14

The increase in the V_{OC}, J_{SC} and PCE value of the solar cells in the present study could be due to the positive effect of the PEA$^+$-content in the germanium perovskite. The PEA$^+$-content apparently improves the layer morphology and layer homogeneity in the solar cell. In order to maintain functioning, high-efficiency solar cells, the water and oxygen content in the glovebox atmosphere had to be kept very low (0.1 ppm) at all times. This was particularly important for the next study, where the lifetime of the built solar cells was tested. The device performance was tracked in the N_2 atmosphere in the glovebox and the solar cells were not encapsulated. The results of this study are summarized in *Figure 34* (and *Table S 5*). After each measurement, the cells were kept in the dark. Impressively, the PCE of the cells with a PEA$^+$-content over 30% had a lifetime of more than 20 days. In contrast, solar cells with a low PEA$^+$-content of 10 and 20% stopped working on the fifth day. The Jsc and PCE varied only slightly throughout the measurements and showed major losses only on the twentieth day. The best results were achieved with 40% and 50% PEA and could maintain 60-72% of its initial PCE after 20 days.
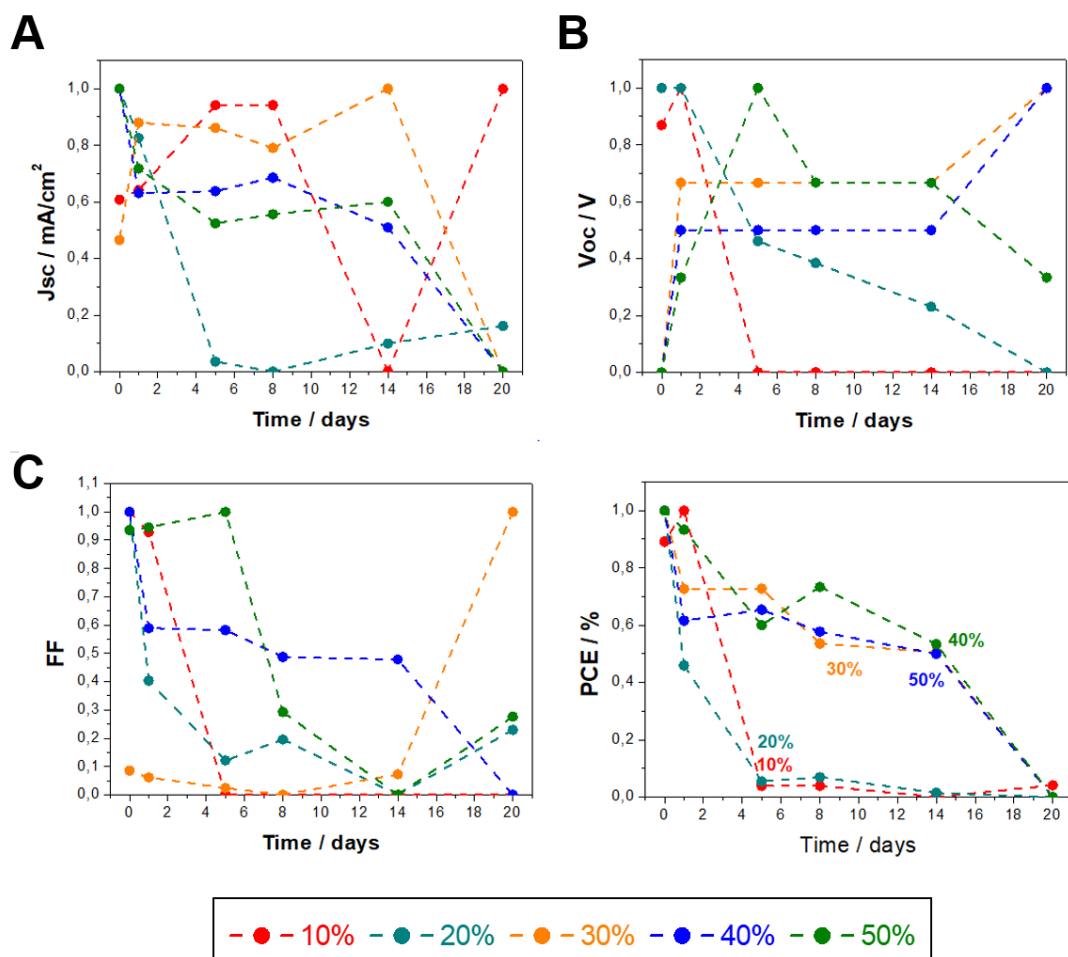
Figure 34. Characteristic parameters of the best $PEA_xMA_{(1-x)}GeI_2Br$ based solar cells with different PEA^+-content over 20 days. The maximum values have been normalized to 1 for easier tracking.

Furthermore, the hysteresis of the new solar cells was investigated. Only slight Current–Voltage hysteresis is observed for these types of solar cells, as shown in the JV curves of a similarly prepared solar cell measured in forward (-0.5 V to 1.5 V) and backward (1.5 V to -0.5 V) direction (see ***Figure 35A***). The corresponding characteristic device parameters are summarized in ***Table S 6***. In addition, an EQE spectra of a $PEA_{0.4}MA_{0.6}GeI_2Br$ based solar cell is presented in ***Figure 35 B***. The onset of photocurrent generation is at 720 nm (start of absorption of $PC_{70}BM$), whereby the ETL $PC_{70}BM$ partially contributes to the current generation and the maximum in the EQE spectra is approx. 480 nm, which is in good agreement with the absorption properties of the germanium halide perovskites. The integrated J_{SC} calculated from the EQE spectrum

is between 2.7 and 3.0 mA/cm². This value is within a few percent deviation from the values extracted from the JV curves.

A

B
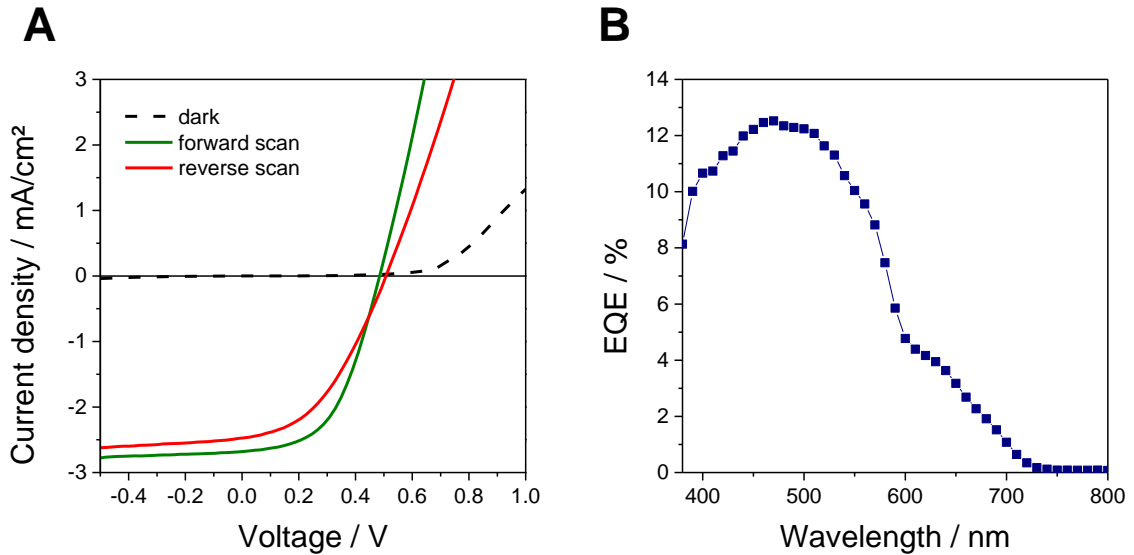
Figure 35. (A) JV curves of a germanium perovskite (PEA$_{0.4}$MA$_{0.6}$GeI$_2$Br) solar cell measured in forward (-0.5 V to 1.5 V) and backward (1.5 V to -0.5 V) scan direction with a scan rate of 150 mV/s. (B) and a corresponding EQE spectra of an optimized PEA$_{0.4}$MA$_{0.6}$GeI$_2$Br based solar cell.

Table 10. Characteristic solar cell parameters extracted from the JV curves shown in *Figure 35A*.

scan direction	V_{OC} / V	J_{SC} / mA/cm²	FF	PCE / %
forward	0.490	2.68	0.51	0.65
backward	0.510	2.47	0.42	0.52

To examine the dense and full coverage of the PEA$_x$MA$_{(1-x)}$GeI$_2$Br film, the morphology of the perovskite films, which were deposited on ITO/glass/PEDOT:PSS-coated substrates by spin-coating technique was observed using a scanning electron microscope (SEM). The resulting micrographs are shown in *Figure 36*. In the Figure 36, SEM images of four different germanium perovskites with 10%, 30% and 50% of PEA$^+$ and without PEA$^+$ are depicted. It can be observed that the addition of 10%, 30% and 50% of PEA$^+$ leads to smaller crystals on the surface, whereas on the layer of perovskites without the addition of PEA$^+$, very large crystals can be observed (*Figure 36A*). All four different

germanium perovskites had one thing in common, they are very crystalline materials, which not only formed a layer, but differently sized crystals were also formed on them.

The SEM images were analysed with ImageJ to calculate the crystal size distribution. The size of ten crystals was measured and a mean value was calculated (see *Figure 36A* (yellow lines on the crystals). *Figure 36B* shows the ratio between the PEAI-content and the average perovskite crystal size. In both illustrations, it can be observed that the crystal size decreases due to the increasing PEAI-content. The sample without PEAI showed the largest crystals, with diameters of about 600 to 1300 nm. In contrast, the sample with a PEAI-content of 50% showed the smallest crystals, with diameters of about 60 to 300 nm. It is important to note that in each sample, these crystals were distributed very homogeneously on the sample.
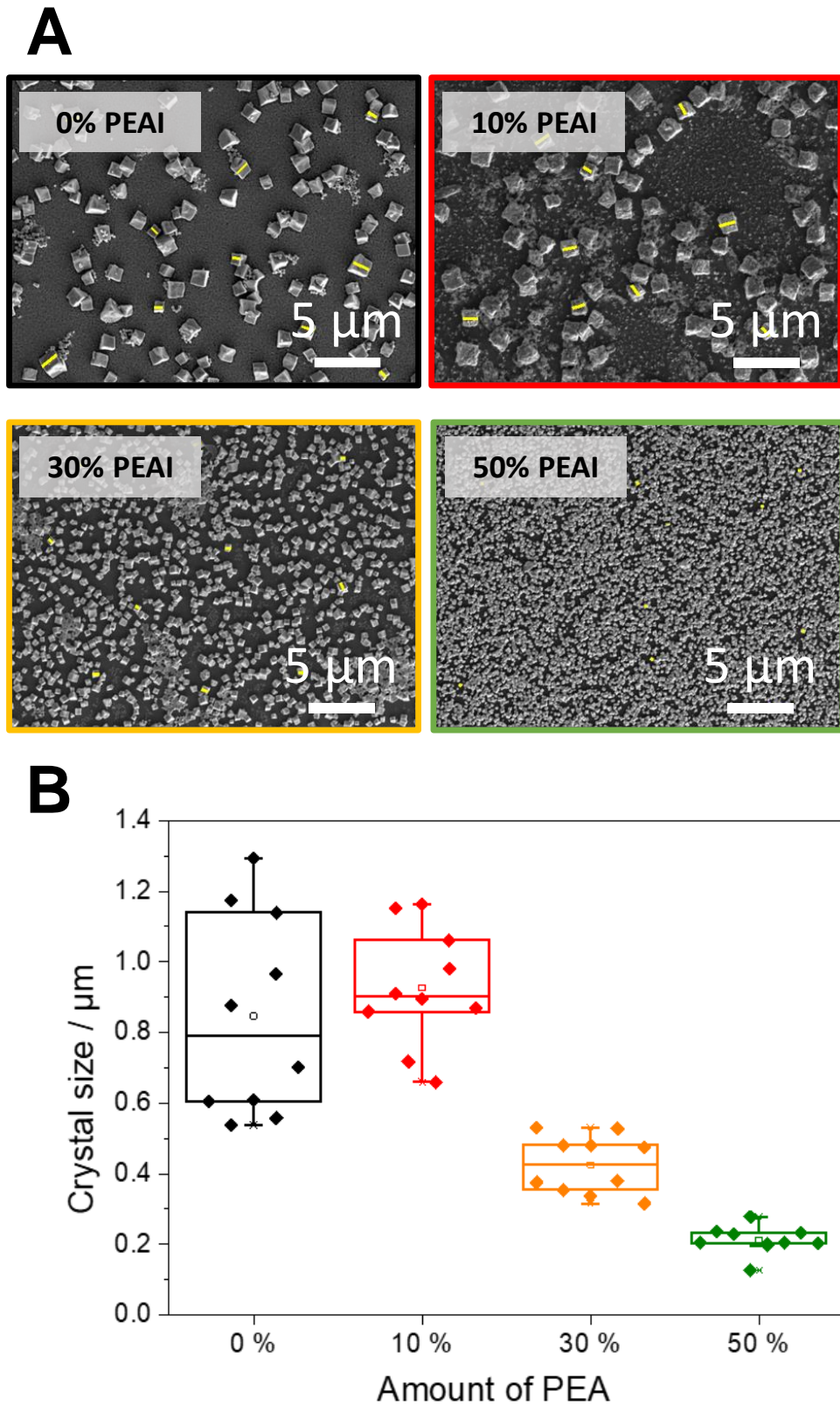
Figure 36. (A) Top view SEM images of the different $PEA_xMA_{(1-x)}GeI_2Br$ perovskite films, without (top left) and with different amounts of the PEA+-cation (bottom right) (B) Relationship between PEAI-content and average perovskite crystal size (are summarized in *Table S 7*).

In order to clarify the influence of the PEAI on the methylammonium germanium halide perovskite, in *Figure 37*, samples were compared without and with 50% PEAI. The Figure shows the optical light microscope images and SEM images with different magnifications of the two perovskite layers: $PEA_{0.5}MA_{0.5}GeI_2Br$ and $MAGeI_2Br$. The crystal size can be controlled by varying the PEAI concentration. As can be seen in the optical light microscopy and SEM images in *Figure 36* and *Figure 37*, a relatively low PEAI concentration is found to increase the methylammonium germanium halide perovskite crystal size, but smaller sizes are obtained at high PEA^+-concentrations. The photovoltaic performance is significantly influenced by the concentration of PEAI, which indicates that the crystal size of the perovskite layer plays an important role in determining the photovoltaic parameters. The increase in the photocurrent density with decreasing crystal size respectively (with the increasing concentration of PEAI) can be seen in *Figure 34*.
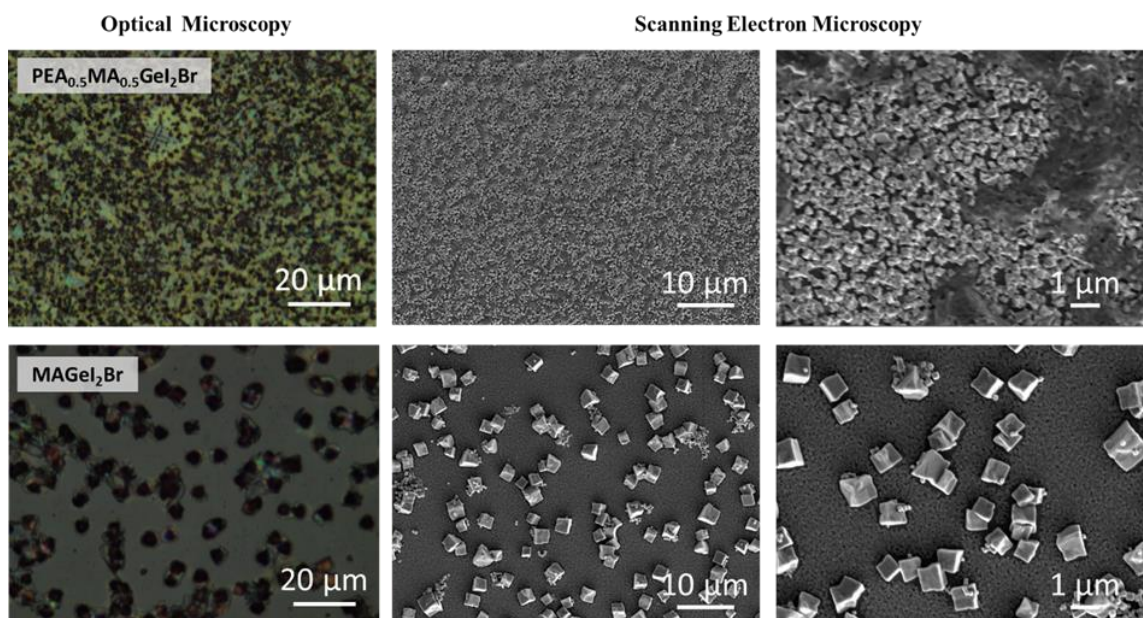
Figure 37. Optical light microscopy images (left) and SEM images with different magnifications (middle and right) of different perovskite layers: $PEA_{0.5}MA_{0.5}GeI_2Br$ and $MAGeI_2Br$.

In addition, it should be investigated whether the produced perovskite layers are just crystals or crystals and a homogeneous perovskite layer underneath. For this purpose, the

surfaces of the produced perovskite layers were examined by light microscopy. A simple method was used for this purpose. All the perovskites to be examined were produced on glass substrates and the layer was removed at one point (in the form of a line) with a cotton swab (see *Figure 38A*). *Figure 37B* clearly shows that by wiping the perovskite layer, not only the crystals but also an underlying homogeneous layer was removed. The light microscope images obtained show a very similar morphology of the layers as in the top view of the SEM images. The methylammonium germanium bromide iodide perovskite (MAGeI$_2$Br) is a very crystalline material, which through the spinning coating process forms a homogeneous layer with large crystals. The presence of this homogeneous perovskite layer below the crystals could also be confirmed by EDX measurement (see *Figure S 5*). For this purpose, the elemental composition of the perovskite layer from the underlying homogeneous layer and that of the crystals were examined. The EDX spectrum obtained showed all element-specific peaks of a perovskite structure, both in the case of the larger crystals and in the homogeneous layer below, whereby the formation of undesired GeI$_2$ crystals could be excluded with a high degree of probability.

In addition, the crystal size decreased from 0% PEA to 50% PEA, and a more homogeneous film layer was formed. These results show that the main factor influencing the morphology of the PEA$_x$MA$_{(1-x)}$GeI$_2$Br perovskite films is the concentration of PEA-cation. This simple technique, the partial exchange of MA to PEA cations in the methylammonium germanium bromide iodide perovskite (MAGeI$_2$Br), could prove extremely useful for crystalline germanium perovskites as a general method for controlling the crystal size and preparation of film layers with full surface coverage.
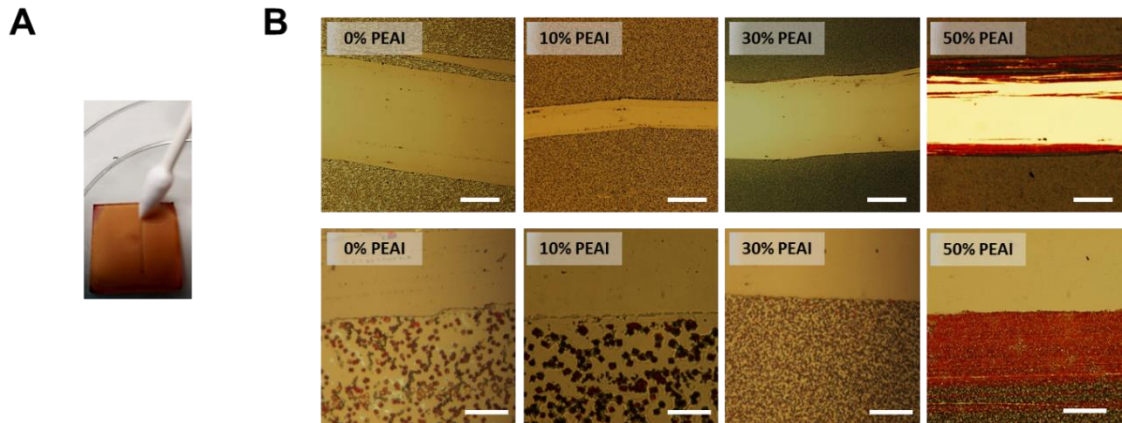
Figure 38. (A) Sample preparation for light microscopy measurement (B) Light microscopy images of the different $PEA_xMA_{(1-x)}GeI_2Br$ perovskite films starting from 0% PEAI (left) to 50% PEAI (right), a magnification of 100x (scale bar 200 µm) and 1000x (scale bar 20 µm) was used.

Figure 39 shows a top-view image of a perovskite film with 50% PEAI deposited on glass/ITO/PEDOT:PSS substrates comparable to the substrates used for the photovoltaic devices. The SEM image shows the perovskite surface in the area 2 - 3 mm from the edge of the solar cell. A formation of two phases could be observed: perovskite crystals (light area) and a second phase (dark area). Since these two phases occur more on the edges of the solar cell and at higher concentrations of PEAI, it can be assumed that this second darker phase comes from the excess of PEAI. The antisolvent step with chlorobenzene creates a more homogeneous layer in the centre of the solar cell than at the edges. Such an accumulation of PEAI at the edge of the solar cell can prevent contact with the electrode and thus lead to defects in the solar cell. The antisolvent step is of great importance for these solar cells. In particular, the time and distance to the solar cell play a significant role.
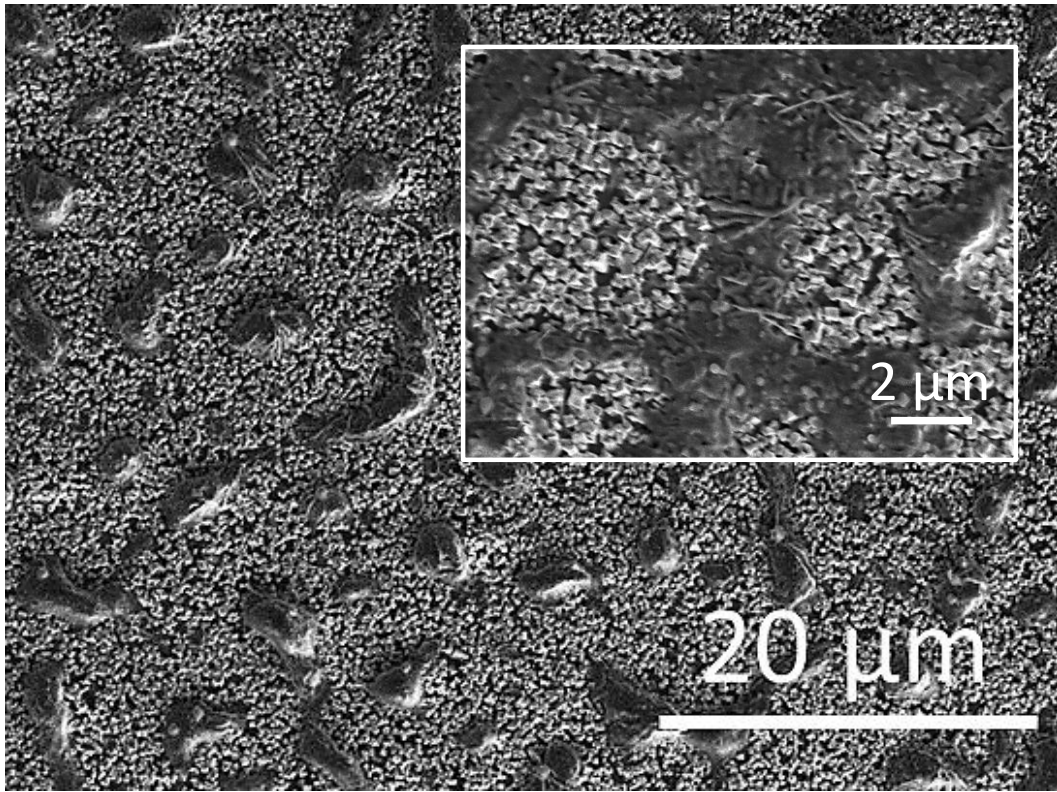
Figure 39. SEM top-view images (2 - 3 mm from the edge of the solar cell) with different magnifications of a perovskite film with 50% PEAI deposited on glass/ITO/PEDOT:PSS with 5.0 kX and 20.0 kX (inset) fold magnification. Inset shows clearly the formation of two phases.

5.4.3 Conclusion

Partial exchange of MA to PEA cations in the methylammonium germanium bromide iodide perovskite (MAGeI$_2$Br) lead to the new 2D/3D mixed-cation germanium halide perovskite exhibiting a significantly different crystal structure with a low dimensionality. The optical properties of this new material are similar to the MAGeI$_2$Br, only a slight hypochromic shift is found in the low-dimensional perovskites. The optical band gaps of the perovskites are approx. 2.1 eV to 2.15 eV for all mixed MA-PEA samples and 2.1 eV for MAGeI$_2$Br. The low-dimensional germanium perovskites have a significantly improved stability in the glovebox atmosphere compared to the three-dimensional perovskite. The large PEA molecules on the border of perovskite bilayers formed significantly more compact and pinhole-free films and thus significantly increased the lifetime of the solar cells. Using these mixed 2D/3D perovskite films obtained by mixing 40% PEA, a PCE of 0.65% was achieved in a planar p-i-n device structure. When stored under inert conditions, these solar cells show stability over 20 days. This solar cell was also examined for hysteresis and it was found that only a slight hysteretic effect can be observed.

5.4.4 Experimental Section

Chemicals and Materials: MAI and MABr (Dyesol), GeI$_2$ (99.99%, ABCR), PEAI (Dyesol), PEDOT:PSS (Clevios P VP.Al 4083, Heraeus), and PC$_{70}$BM (99.5%, Solenne BV) were used as received. Anhydrous chlorobenzene was obtained from Sigma Aldrich and DMF was used from SeccoSolv® with a purity ≥99.9 % dried.

Sample and solar cell preparation: A 1 M precursor solution of PEA$_x$MA$_{(1-x)}$GeI$_2$Br was prepared by dissolving MAI, MABr and GeI$_2$ with a varying amount of phenylethylammonium iodide (PEAI) (x = 0, 0.10, 0.30, 0.40 and 0.50) dissolved in dry N,N-dimethylformamide (DMF). The solution was stirred for 24 h at room temperature

in N_2 atmosphere in a glovebox. Before use, the precursor solution was filtered through a 0.45 µm PTFE filter.

ITO coated glass substrates (15 x 15 mm, 15 Ω/sq, purchased from Lumtec) were carefully rinsed with acetone and put into an isopropanol bath followed by sonication for 30 min at 40 °C. Subsequently, the substrates were dried under an N_2 gas stream and treated with oxygen plasma for 3 min. As first layer, a PEDOT:PSS film was spin coated at 6000 rpm for 30 s and the substrates were put into a glovebox immediately afterwards for a temperature treatment at 120 °C for 20 min. Next, the precursor solution was spin coated onto the PEDOT:PSS film in glovebox atmosphere with the following spin coating conditions: 4000 rpm, 1000 rpm/s, 30 s. After 10 s of spinning, chlorobenzene was dropped onto the rotating substrate, whereupon the color of the film changed from yellow to orange/red. Afterwards, the perovskite was tempered at 70 °C for 10 min. A $PC_{70}BM$ solution in dry chloroform (50 mg/mL) was spin coated on top of the perovskite layer with 1000 rpm, 500 rpm/s for 30 s. Ag electrodes (3 x 3 mm²) were deposited by thermal evaporation at a rate of 2 Å/s at a base pressure below 1×10^{-5} mbar.

Optical characterisation: UV-Vis spectra were acquired with a Perkin Elmer Lambda 35 UV-Vis spectrometer equipped with an integrating sphere. For (time-resolved) UV-Vis measurements, the perovskite films were prepared on glass substrates in the same way as described above. The UV-Vis measurements were taken (and the time resolved measurements were started) immediately after taking the samples out of the nitrogen filled glovebox.

X-Ray Diffraction (XRD): Powder X-ray diffraction (XRD) patterns were recorded on a Rigaku Miniflex diffractometer (600 W) operated at 40 kV and 40 mA using Cu K_α radiation. For the XRD measurements, the perovskite films were prepared on glass slides (15 x 15 mm) and covered with a thin PMMA protection layer, spin coated from a chlorobenzene solution (10 mg/mL).

Device characterization: JV curves (measured with a shadow mask) were recorded in a glovebox using a Keithley 2400 source measure unit and a custom made LabView software. The samples were illuminated by a Dedolight xenon lamp with a spectrum similar to the AM 1.5G spectrum at 100 mW/cm². The EQE spectra were measured using monochromatic light from a MuLTImode4 monochromator (AMKO) equipped with a 75 W Xenon lamp chopped at 30 Hz. The signals (wavelength increment: 10 nm) were measured by a lock-in amplifier from Stanford Research Systems (Model SR830). A

spectrally calibrated 818-UV/DB photodiode (Newport Corporation) was used as a reference. A sealed measuring box with a quartz glass window was used to protect the solar cells against ambient atmosphere during the EQE measurement.

Scanning Electron Microscopy (SEM): The investigation of the microstructure was performed using a field emission scanning electron microscope (FESEM) TESCAN MIRA3 (TESCAN Brno s.r.o., Brno, Czech Republic) coupled with an energy dispersive X-ray spectrometer (EDS) Octane Plus detector and the TEAM v.4.5 software analysis (Ametek, Inc. Berwyn, PA, USA) was used. Thereby, SEM micrographs were acquired in In-Beam SE Mode, with an acceleration voltage of 3 kV, a beam spot size of 4 nm and a working distance of 3.5 mm. The SEM micrographs were further analyzed using ImageJ software.

Acknowledgment

Supporting Information

A Low-Dimensional Mixed-Cation Germanium Halide Perovskite: Structural, Optical and Photovoltaic Properties

Table S 5. Parameters including mean values and standard deviations of the best solar cells prepared with different PEAI-content in the $PEA_xMA_{(1-x)}GeI_2Br$ absorber layer over 20 days.

PEA-content	VOC / V	JSC / mA/cm²	FF	PCE / %
	0,409	1,80	0,38	0,27
	0,409	1,78	0,38	0,27
0.1 M	0,409	1,75	0,38	0,27
	0,389	1,72	0,37	0,24
	0,389	1,57	0,33	0,20
	0.401 ± 0.010	**1.73 ± 0.09**	**0.37 ± 0.02**	**0.25 ± 0.03**
	0,429	2,68	0,43	0,49
	0,429	2,46	0,42	0,44
0.2 M	0,409	2,62	0,41	0,43
	0,409	2,52	0,37	0,38
	0,349	1,64	0,28	0,16
	0.405 ± 0.030	**2.38 ± 0.38**	**0.38 ± 0.05**	**0.38 ± 0.12**
	0,490	2,45	0,44	0,53
	0,470	2,54	0,45	0,53
0.3 M	0,450	2,71	0,42	0,52
	0,450	2,49	0,40	0,43
	0,450	2,45	0,39	0,42
	0.462 ± 0.01	**2.53 ± 0.10**	**0.42 ± 0.02**	**0.49 ± 0.05**
	0,490	2,68	0,51	0,65
	0,470	2,46	0,45	0,51
0.4 M	0,349	2,25	0,45	0,34
	0,349	2,06	0,41	0,28
	0,328	2,07	0,27	0,18
	0.397 ± 0.07	**2.30 ± 0.23**	**0.42 ± 0.08**	**0.40 ± 0.17**
	0,450	2,73	0,45	0,55
	0,470	2,52	0,46	0,54
0.5 M	0,450	2,50	0,43	0,48
	0,389	2,65	0,39	0,39
	0,308	2,45	0,35	0,26
	0.413 ± 0.07	**2.56 ± 0.12**	**0.42 ± 0.05**	**0.44 ± 0.12**

Table S 6: Parameters including mean values and standard deviations of the solar cells prepared with different PEAI-content in the $PEA_xMA_{(1-x)}GeI_2Br$ absorber layer over 20 days.

	Days	V_{OC} / V	J_{SC} / mA/cm²	FF	PCE / %
10% PEAI	0	0.409	1.80	0.38	0.27
	1	0.470	1.89	0.35	0.30
	5	0.005	2.64	1	0.01
	8	0.005	2.64	1	0.01
	14	0.005	0.28	1	0.00
	20	0.005	2.78	1	0.01

	Days	V_{OC} / V	J_{SC} / mA/cm²	FF	PCE / %
20% PEAI	0	0.429	2.68	0.43	0.49
	1	0.429	2.08	0.27	0.23
	5	0.288	-0.64	0.19	0.03
	8	0.268	-0.76	0.21	0.04
	14	0.227	-0.42	0.15	0.01
	20	0.167	-0.20	0.22	0.01

	Days	V_{OC} / V	J_{SC} / mA/cm²	FF	PCE / %
30% PEAI	0	0.490	2.45	0.44	0.53
	1	0.490	2.75	0.35	0.47
	5	0.490	2.74	0.35	0.47
	8	0.510	2.68	0.31	0.42
	14	0.490	2.58	0.32	0.41
	20	0.530	2.04	0.27	0.29

	Days	V_{OC} / V	J_{SC} / mA/cm²	FF	PCE / %
40% PEAI	0	0.490	2.68	0.51	0.65
	1	0.510	2.41	0.46	0.55
	5	0.510	2.42	0.46	0.56
	8	0.510	2.45	0.44	0.54
	14	0.510	2.33	0.44	0.52
	20	0.530	1.96	0.38	0.39

	Days	V_{OC} / V	J_{SC} / mA/cm²	FF	PCE / %
50% PEAI	0	0.470	2.52	0.46	0.54
	1	0.470	2.54	0.45	0.53
	5	0.490	2.48	0.4	0.48
	8	0.490	2.44	0.41	0.50
	14	0.490	2.47	0.39	0.47
	20	0.510	2.02	0.39	0.39

Table S 7: ImageJ evaluation: the size of ten crystals was measured and an average was calculated.

0 % PEAI

Crystal	Area	Mean	Min	Max	Angle	Length
1	0.168	141.864	16	215	12.804	1.139
2	0.087	66.971	50	98	-41.634	0.608
3	0.138	128.222	114	183	47.121	0.965
4	0.24	112.489	77	167	-25.463	1.175
5	0.112	98.364	73	187	-5.194	0.558
6	0.168	72.955	58	201	-19.44	0.878
7	0.122	81	50	126	0	0.606
8	0.158	106.839	39	227	-30.256	0.702
9	0.286	76.634	46	181	38.66	1.294
10	0.117	163.696	115	255	-48.814	0.537

10 % PEAI

Crystal	Area	Mean	Min	Max	Angle	Length
1	0.26	80.549	47	175	34.38	1.163
2	0.145	78.93	56	142	-32.471	0.659
3	0.255	113.9	31	204	15.255	1.152
4	0.199	85.167	49	188	16.39	0.895
5	0.158	113.677	75	198	-50.711	0.718
6	0.184	100.833	70	156	3.18	0.91
7	0.194	122.697	62	185	11.889	0.981
8	0.194	99.145	59	233	-61.928	0.859
9	0.191	109.347	56	251	-54.462	0.869
10	0.214	111.964	70	205	0	1.061

30 % PEAI

Crystal	Area	Mean	Min	Max	Angle	Length
1	0.071	114.929	87	157	0	0.337
2	0.071	111.214	87	157	0	0.354
3	0.082	173.781	128	246	0	0.379
4	0.102	144.825	68	238	0	0.48
5	0.102	151.075	109	230	0	0.48
6	0.064	101.4	77	176	-45	0.375
7	0.112	116.909	65	223	-66.038	0.527
8	0.069	99.37	71	191	-30.964	0.316
9	0.102	120.975	96	153	26.565	0.531
10	0.102	126.4	94	253	-26.565	0.474

50 % PEAI

Crystal	Area	Mean	Min	Max	Angle	Length
1	0.041	161.688	96	255	-90	0.202
2	0.059	162.826	114	221	-78.69	0.278
3	0.043	156.353	108	211	56.31	0.204
4	0.041	154.625	126	188	-14.036	0.229
5	0.046	183.056	78	255	-36.87	0.233
6	0.041	145.75	81	201	0	0.236
7	0.043	153.471	37	238	45	0.197
8	0.036	153.286	91	253	-14.036	0.204
9	0.02	188.375	170	221	-90	0.126
10	0.043	150.882	101	188	0	0.205

Table S 8. ImageJ evaluation: comparison of crystal sizes of the different $PEA_xMA_{(1-x)}GeI_2Br$ perovskite films starting from 0% PEAI to 50% PEAI.

	Length / µm			
Crystal	**0 %**	**10 %**	**30 %**	**50 %**
1	1.139	1.163	0.337	0.202
2	0.608	0.659	0.354	0.278
3	0.965	1.152	0.379	0.204
4	1.175	0.895	0.48	0.229
5	0.558	0.718	0.48	0.233
6	0.878	0.91	0.375	0.236
7	0.606	0.981	0.527	0.197
8	0.702	0.859	0.316	0.204
9	1.294	0.869	0.531	0.126
10	0.537	1.061	0.474	0.205
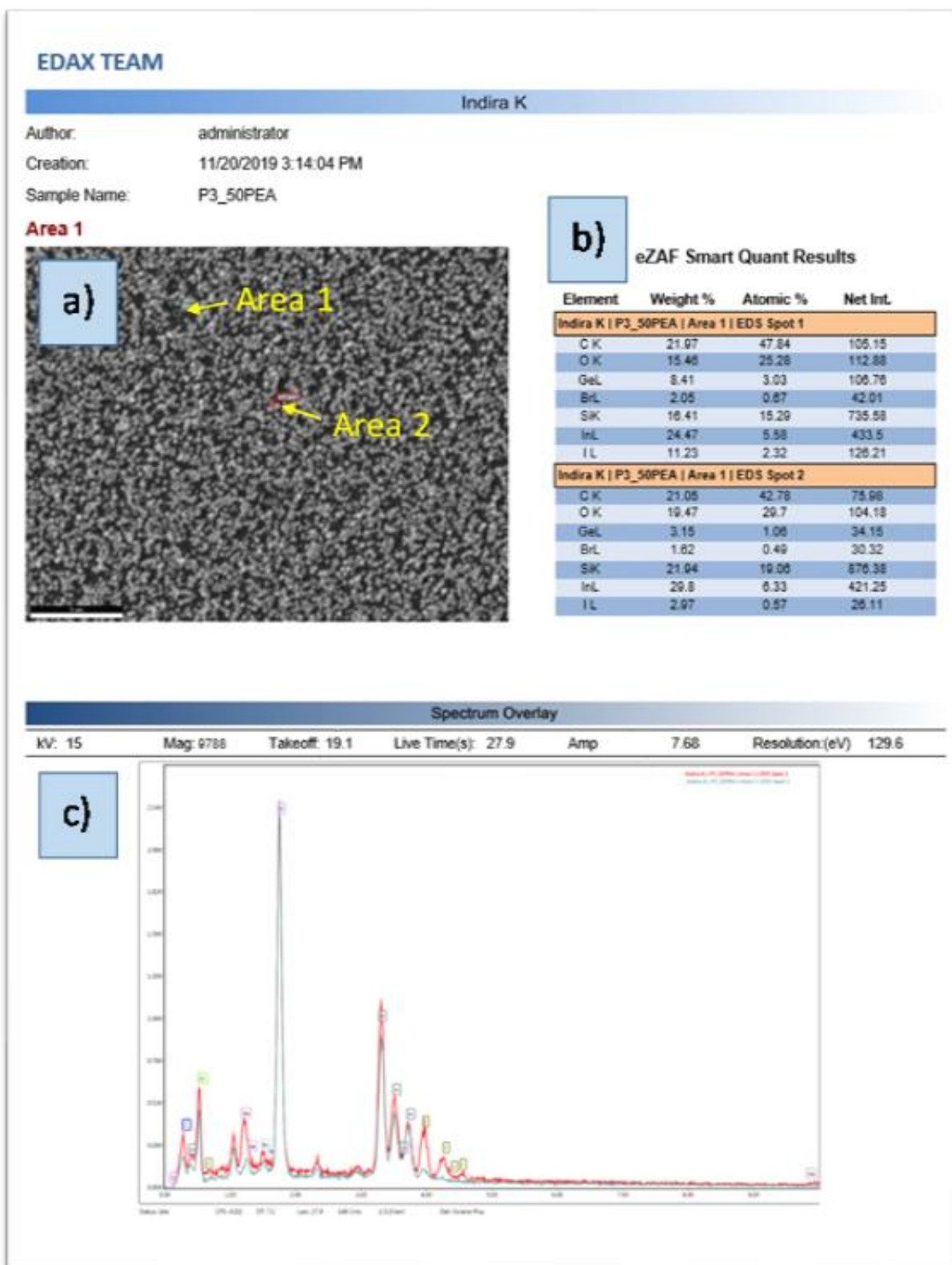
Figure S 5. The morphology, structures, and chemical composition of the prepared mixed 2D/3D germanium halide perovskite with 50 % PEAI. a) the top-view SEM image of the glass/ITO/PEDOT:PSS/ perovskite film, b) the EDX results and c) spectrum of area 1 (crystal) and area 2 (dark area below the crystals).
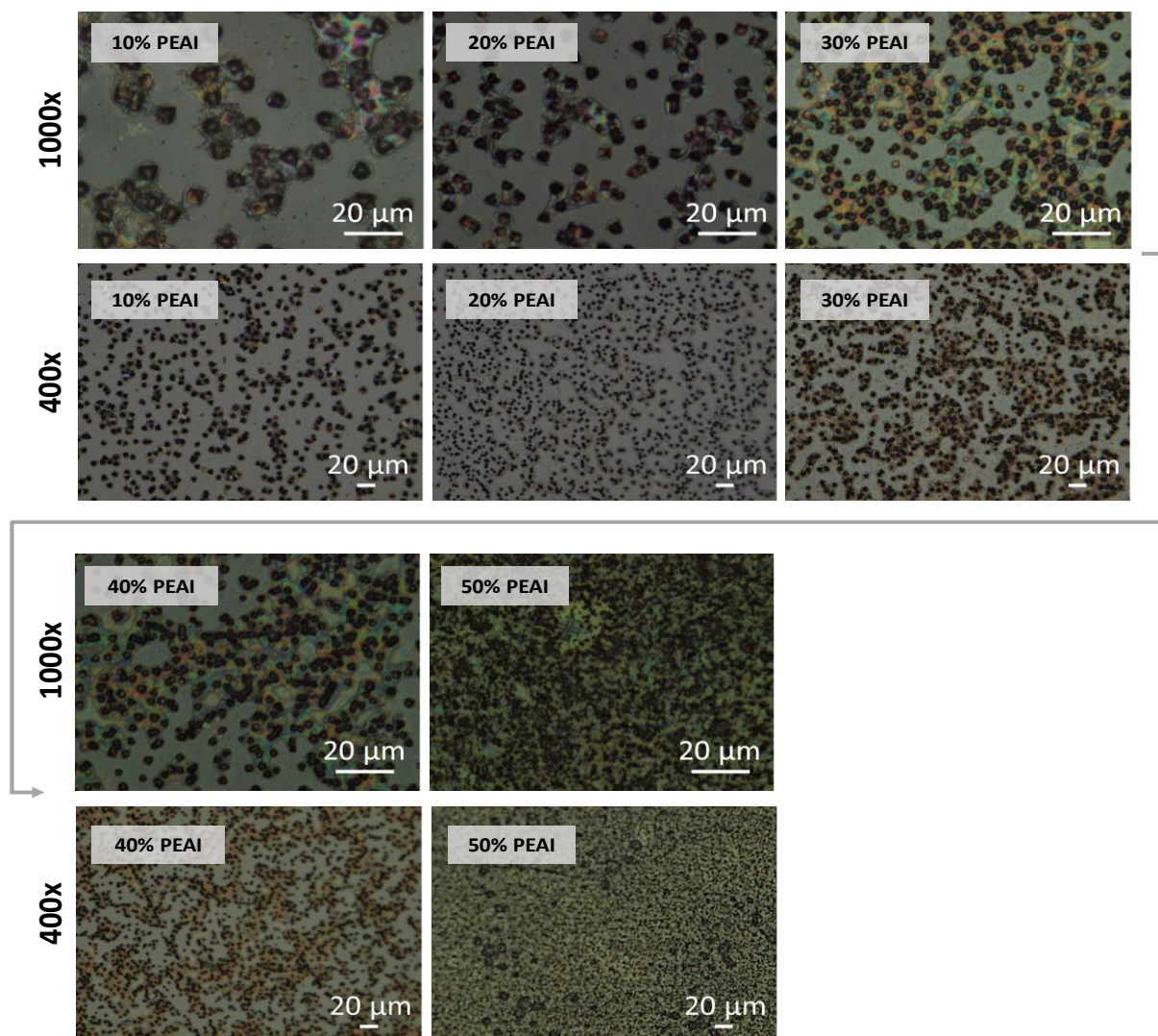
Figure S 6. Optical microscopy images of the different PEA$_x$MA$_{(1-x)}$GeI$_2$Br blends starting from 0.1 M PEAI (top left) to 0.5 M PEAI (bottom right).

5.5 Influence of the Annealing Step of the Perovskite Layer on the Solar Cell Performance

5.5.1 Introduction

The annealing step of the perovskite layer after spin coating is of crucial importance and has a direct influence on the performance of a solar cell. The different layer formation influences the carrier transport and thus a different performance of the solar cell arises. Therefore, this was examined in more detail and the perovskite layer was annealed both at 70 and at 100 °C for 10 minutes. All layers of perovskite ($MAGeI_2Br$ and $PEA_xMA_{(1-x)}GeI_2Br$ (X=50%)) were placed directly on the warm heating plate (70 °C or 100 °C) at room temperature in the glove box. The prepared germanium perovskites were then examined using SEM microscopy.

In addition to anneaing, the radiation source (halogen lamp) and its influence on the germanium perovskite were also examined. The use of an LED lamp is to ensure that no unknown heat exchange negatively affects the sample, which could cause the germanium perovskite to degrade more quickly. Two solar cells with almost identical performance were selected for this experiment. The samples were illuminated with an LED and a standard xenon lamp with a spectrum similar to the AM 1.5 G spectrum at 100 mW / cm².

5.5.2 Results and Discussion

The best solar cell performance achieved within this study was with a direct annealing step on the hot heating plate at 70 °C for 10 minutes (see *Figure 40*). Solar cells that have not been annealed show very scattering PCE values from 0% to 0.35%. While solar cells that were annealed at 100 °C have no or only very low efficiencies up to 0.1%.

Figure 40. Boxplot of the mean values and standard deviation of the PCE of MAGeI$_2$Br solar cells that were not annealed and of solar cells that were annealed at 70 °C and 100 °C (see *Table S 9*).

Although a temperature of 100 °C was the best choice for other perovskites, germanium perovskites showed almost no performance. One explanation for this is the very fast crystallization of the germanium absorber material. At an annealing step of 100 °C of the MAGeI$_2$Br, with the solvent evaporating faster, in particular, the formation of large crystals as well as crystals that were poorly arranged geometrically, was observed (see *Figure 41*).

Figure 41. SEM images of the MAGeI$_2$Br annealed at 70 °C (first rich) and 100 °C (second rich) with 5.0 kX (left), 10 kX (center) and 20.0 kX (right) fold magnification.

Partial exchange of MA to PEA cations in the methylammonium germanium bromide iodide perovskite (MAGeI$_2$Br) lead to the new 2D/3D mixed-cation germanium halide perovskite, exhibiting a significantly different crystal structure with a low dimensionality. Such a crystal structure shows, in comparison to MAGeI$_2$Br perovskites, significantly smaller and finer crystals at an annealing step at 70 °C as well as at 100 °C. More detailed examinations of the crystals could not be carried out because they melted during SEM microscopy at higher magnifications (see **Figure 43**). With the PEA$_{0.5}$MA$_{0.5}$GeI$_2$Br absorber material, the best solar cell performance was also achieved with a direct annealing step on the hot heating plate at 70 °C for 10 minutes (see **Figure 42**). Solar cells that have not been tempered show very scattering PCE values from 0% to 0.35%. While solar cells that have been tempered at 100 °C have no or only very low efficiencies of up to 0.15%.
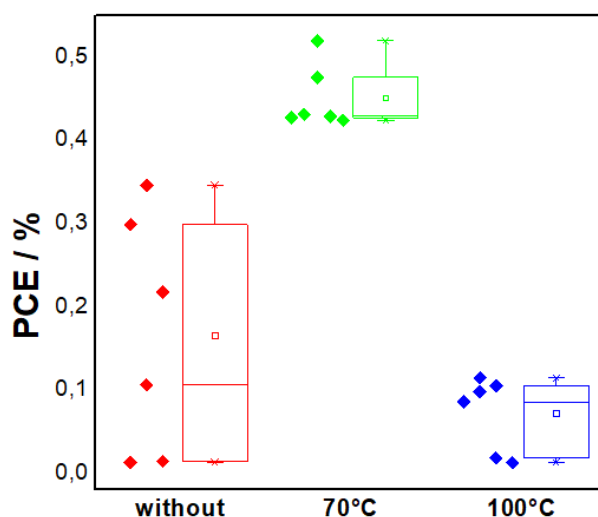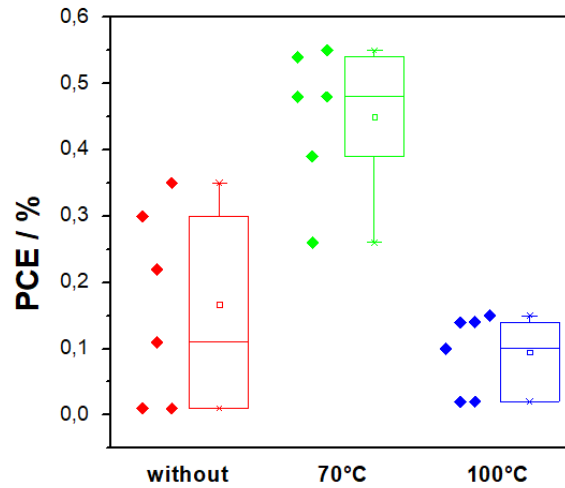
Figure 42. Boxplot of the mean values and standard deviation of the PCE of $PEA_{0.5}MA_{0.5}GeI_2Br$ solar cells that were not annealed and of solar cells that were annealed at 70 °C and 100 °C (see *Table S 10*)
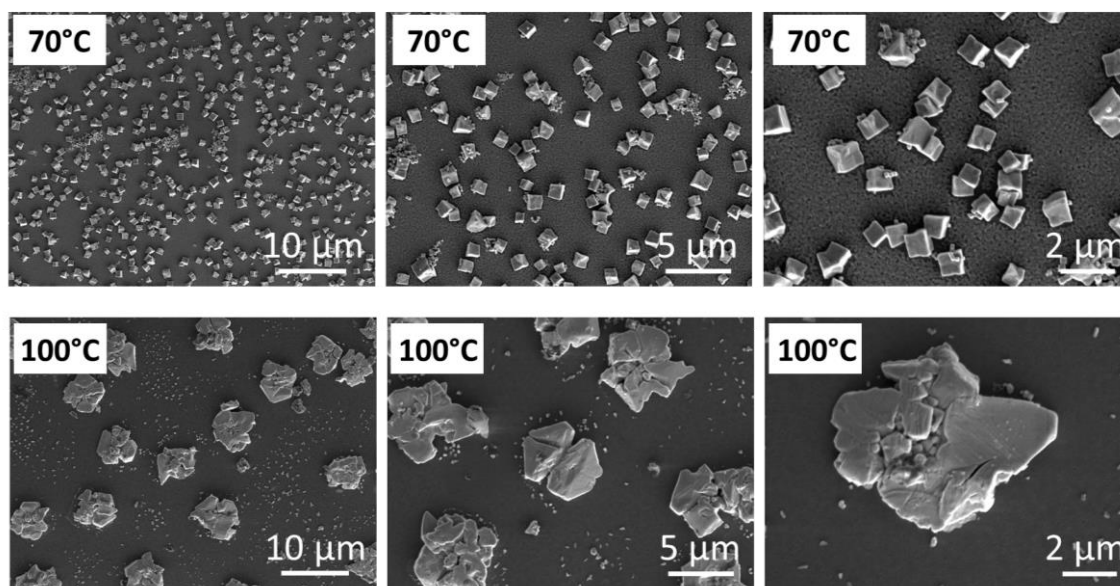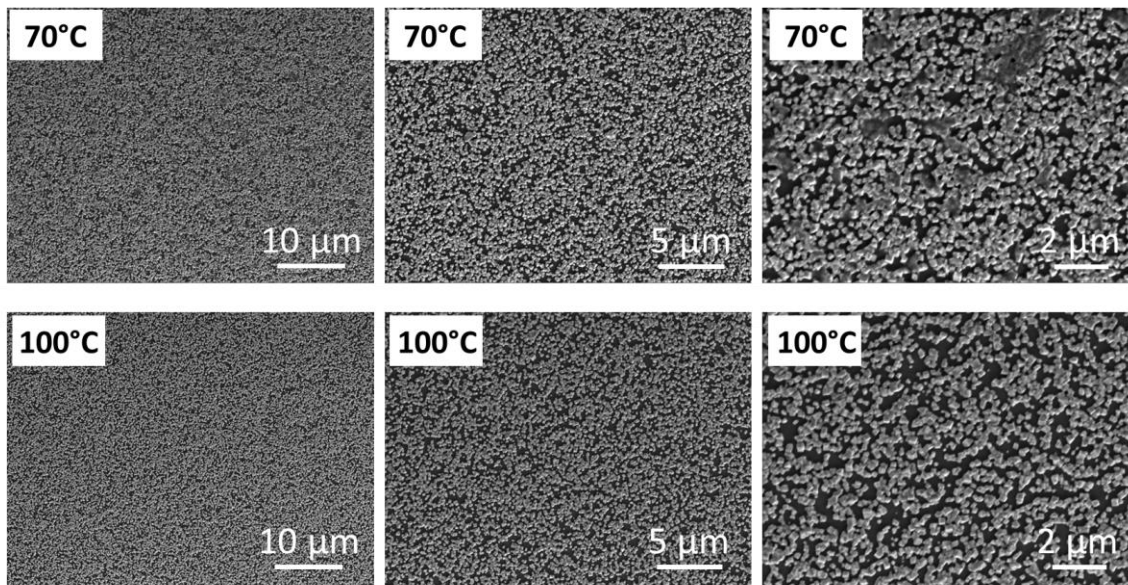

Figure 43. SEM images of the $PEA_{0.5}MA_{0.5}GeI_2Br$ annealed at 70 °C (first rich) and 100 °C (second rich) with 5.0 kX (left), 10 kX (center) and 20.0 kX (right) fold magnification.

Furthermore, MPP tracking measurements (see ***Figure 44***) were carried out, whereby measurements realized with a halogen lamp show a constantly decreasing output of the solar cells. The voltage at MPP (V_{MPP}) at the beginning of the measurement increases

slightly and drops sharply after 20 minutes. The current density at MPP (J_{MPP}) also deteriorates, which means that after 60 minutes there was no more power output (PCE) from the solar cell. The solar cell was continuously illuminated.
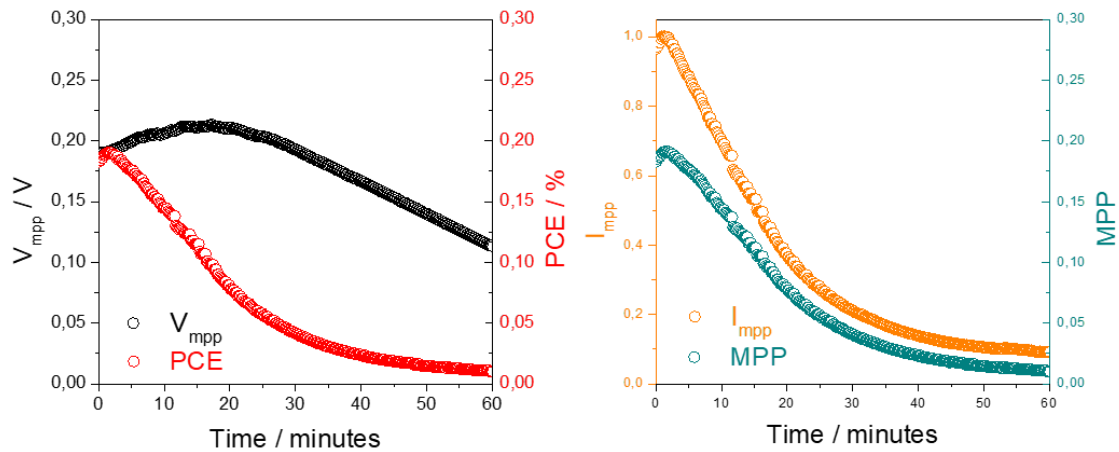
Figure 44. Maximum power point tracking measurements halogen lamp.

When the light source was replaced and an LED lamp was used, it could be shown that the MPP tracking measurements (see *Figure 45*) showed constant power from the solar cell. The voltage at MPP (V_{MPP}) increases slightly at the start of the measurement and stabilizes after approx. 50 minutes, while the current density at MPP (J_{MPP}) deteriorates slightly. Impressively, the use of a new light source led to a constant power output and a PCE of 0.23% after even 90 minutes of continuous lighting. It could be determined therefore, that germanium perovskite, as already suspected, is sensitive to heat.
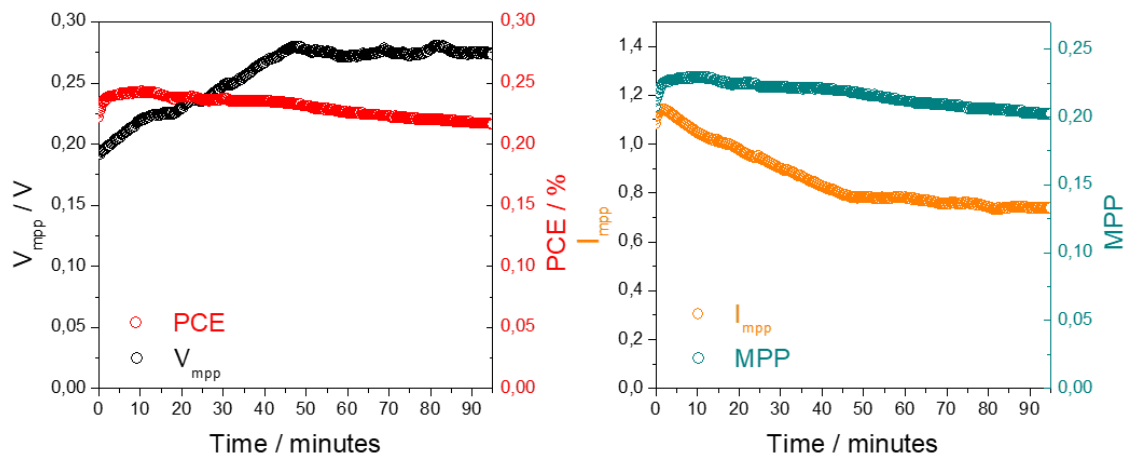
Figure 45. Maximum power point tracking measurements with LED lamp.

With the help of the PT100 table, the exact temperature increase could be determined using the measured resistance of a glass substrate. This measurement showed that the glass substrate already had a temperature of 29 °C at the beginning of the measurement and after 100 minutes of continuous exposure the temperature rose to 42 °C (see *Figure 46*).
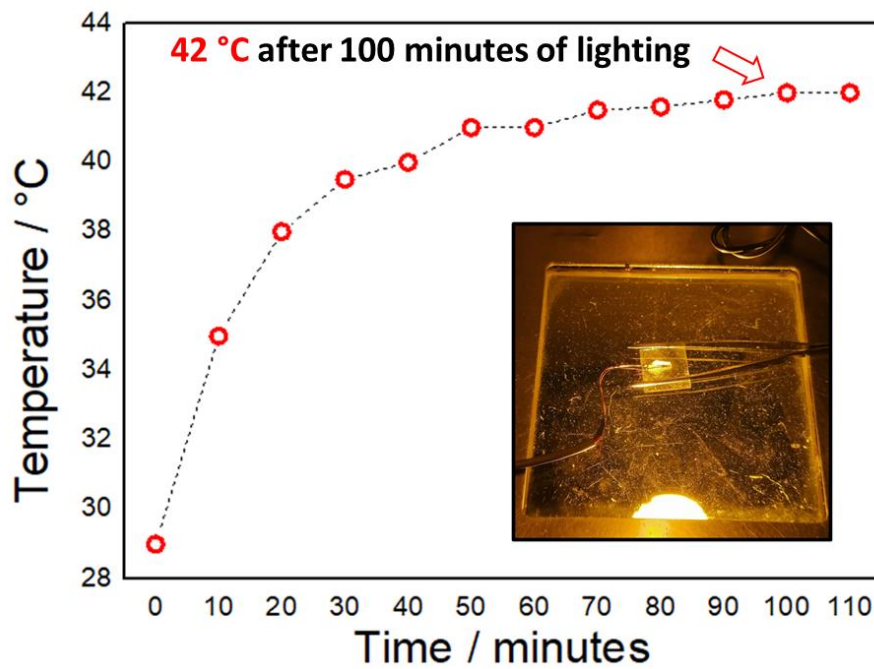
Figure 46. Heat development of a glass substrate determined using the PT100 table over the time. Continuous exposure using a halogen lamp. Inset shows a photo of the measured glass substrate.

Table 11. Time, resistance and the determined temperature (via PT100 table) from the measured glass substrate.

Time / min	Resistance / Ω	Temperature / °C
0	111.90	29
10	113.51	35
20	114.60	38
30	115.22	39.5
40	115.59	40
50	115.80	41
60	115.90	41
70	116.05	41.5
80	116.13	41.6
90	116.25	41.8
100	116.31	42
110	116.34	42

5.5.3 Conclusion

In summary, it could be shown that the formation of a homogeneous perovskite layer is essential for the performance of the solar cell. The annealing step in germanium perovskite is very important for the crystallization of the perovskite layer. It was found that direct annealing for 10 minutes at 70 °C on a hot plate gives the best results. At an annealing step of 100 °C of the $MAGeI_2Br$, with the solvent evaporating faster, in particular, the formation of large crystals as well as crystals that were poorly arranged geometrically, was. It is assumed that similar defects also occur with mixed 2D / 3D low dimensional germanium perovskites. However, due to the smaller and finer crystals, this could not be confirmed by SEM microscopy. The built solar cells showed almost no performance either when the annealing step was omitted nor annealed at a temperature of 100 °C. While germanium perovskite solar cells, both heated directly on a hot plate at 70 °C for 10 minutes, gave the best performance.

Furthermore, it was also found that the heating of the halogen lamp has a negative influence on the germanium perovskite. The measured resistance showed that the glass substrate warmed to 29 °C at the start of the measurement and reached 42 °C after 100 minutes. Such heating of the germanium perovskite solar cell degrades the perovskite, and the solar cell stops working after a short time. When the light source was replaced and an LED lamp was used, it could be shown that the MPP tracking measurements showed an almost unchanged performance of the solar cell, even after 90 minutes.

Supporting Information

Table S 9. Photovoltaic performance parameters of MAGeI$_2$Br solar cells without and with an annealing step at 70 °C and 100 °C for 10 minutes.

	V_{OC} / V	J_{SC} / mA/cm²	FF	PCE / %
without	0.279	1.69	0.45	0.22
	0.451	1.64	0.46	0.35
	0.044	1.99	0.16	0.01
	0.043	1.78	0.17	0.01
	0.216	1.84	0.27	0.11
	0.435	1.48	0.46	0.30
	V_{OC} / V	J_{SC} / mA/cm²	FF	PCE / %
70 °C	0.451	2.45	0.44	0.48
	0.435	2.26	0.48	0.43
	0.451	2.61	0.45	0.52
	0.435	2.23	0.45	0.43
	0.435	2.29	0.44	0.43
	0.435	2.25	0.44	0.42
	V_{OC} / V	J_{SC} / mA/cm²	FF	PCE / %
100 °C	0.090	0.87	0.23	0.02
	0.357	0.79	0.35	0.10
	0.373	0.84	0.34	0.10
	0.388	0.87	0.34	0.11
	0.075	0.80	0.21	0.01
	0.357	0.70	0.34	0.09

Table S 10. Photovoltaic performance parameters of PEA$_{0.5}$MA$_{0.5}$GeI$_2$Br solar cells without and with an annealing step at 70 °C and 100 °C for 10 minutes.

	V$_{OC}$ / V	J$_{SC}$ / mA/cm²	FF	PCE / %
without	0.279	1.69	0.45	0.22
	0.451	1.64	0.46	0.35
	0.044	1.99	0.16	0.01
	0.043	1.78	0.17	0.01
	0.216	1.84	0.27	0.11
	0.435	1.48	0.46	0.30
	V$_{OC}$ / V	J$_{SC}$ / mA/cm²	FF	PCE / %
70 °C	0.450	2.73	0.45	0.55
	0.470	2.52	0.46	0.54
	0.450	2.50	0.43	0.48
	0.389	2.65	0.39	0.39
	0.308	2.45	0.35	0.26
	V$_{OC}$ / V	J$_{SC}$ / mA/cm²	FF	PCE / %
100 °C	0.090	1.05	0.24	0.02
	0.388	0.94	0.39	0.14
	0.388	0.97	0.39	0.14
	0.404	0.98	0.38	0.15
	0.075	0.89	0.25	0.02
	0.372	0.79	0.36	0.10

6 SUMMARY AND OUTLOOK

Lead perovskite solar cells have achieved power conversion efficiencies that approximate established photovoltaic technologies. The biggest problem is that the absorber material in conventional perovskite solar cells always contains of lead. They are also sensitive to moisture and have a short lifespan. Although the lead quantities in the PSCs are very small, the lead represents a considerable hurdle, both in the application of photovoltaic devices and in regards to social acceptance. Therefore, many PSCs research communities are endeavoring to make not only efficient, but also stable and lead-free PSCs. In this work, I described how germanium is suitable as a possible alternative element for the replacement of lead in metal halide perovskites.

First, new germanium perovskites were synthesized, installed in solar cells and examined more closely with the following device architecture: glass/ITO/PEDOT:PSS/perovskite/$PC_{70}BM$/ Ag. The manufacturing processes have been optimized to improve the performance of the solar cells. Furthermore, all the optical properties of the prepared germanium perovskites were examined. After the synthesis of the first germanium perovskite and the optimization of the manufacturing steps, cations and anions could be varied. Germanium halide perovskite has good optoelectronic properties but was disadvantageous compared to the bivalent lead (Pb^{2+}) because it can easily be oxidized to the +4-oxidation state.

In the second part of this work, I focused on improving the stability of methylammonium germanium iodide perovskite ($MAGeI_3$). In summary, we could show that the bromide content in methylammonium germanium halide perovskites plays an important role for their performance in photovoltaic devices. Modifying the chemical composition of the germanium perovskite, i.e. introducing bromide ions into the methylammonium germanium iodide perovskite, leads to a significant improvement of the solar cell performance, along with a slight enhancement of the stability of the germanium perovskite. By substituting 10% of the iodide with bromide, power conversion efficiencies up to 0.57% were obtained in $MAGeI_{2.7}Br_{0.3}$ based solar cells. While the $MAGeI_3$-based solar cells completely lost their performance within a few hours, even under inert conditions, the dismantling of the $MAGeI_{2.7}Br_{0.3}$ was delayed. The improved

stability arises when the X-site anion is partially replaced by iodide on bromide, which is due to the reduction of the lattice of a more compact and stable crystal structure.

The third topic of this work was the preparation of a new low-dimensional germanium perovskite. This was done by the partial with exchange of MA for PEA cations in the methylammonium germanium bromide iodide perovskite ($MAGeI_2Br$). The new 2D / 3D germanium halide perovskite with mixed cations showed a significantly different crystal structure with low dimensionality. The optical properties of this new material are like those of $MAGeI_2Br$, with only a slight hypochromic shift in the low-dimensional perovskites. The optical bandgaps of the perovskites are approx. 2.1 eV to 2.15 eV for all mixed MA-PEA samples and 2.1 eV for $MAGeI_2Br$. The low-dimensional germanium perovskites have a significantly improved stability in the glove compartment atmosphere, compared to the three-dimensional perovskite. The large PEA molecules on the border of the perovskite nano-layers formed significantly more compact and hole-free films and thus extended the lifespan of the solar cells considerably. Using these mixed 2D / 3D perovskite films obtained by mixing 40% PEA, a PCE of 0.65% was achieved in a planar p-i-n device structure. When stored under inert conditions, these solar cells show stability over 20 days. This solar cell was also examined for hysteresis and it was found that only a slight hysteretic effect can be observed.

Furthermore, it could be argued that the formation of a homogeneous perovskite layer is essential for the performance of the solar cell. The annealing step in germanium perovskite is very important for the crystallization of the perovskite layer. It has been found that direct annealing for 10 minutes at 70 °C on a hot plate gives the best results. When the $MAGeI_2Br$ was annealed at 100 °C and the solvent evaporated more quickly, in particular, the formation of large crystals as well as crystals that were poorly arranged geometrically, was observed. Solar cells of both absorber materials ($MAGeI_2Br$ and $PEA_{0.5}MA_{0.5}GeI_2Br$) that were not tempered show very scattering PCE values from 0% to 0.35%. While solar cells that have been tempered at 100 °C have no or only very low efficiencies of up to 0.15%. It is assumed that similar defects also occur with mixed low-dimensional germanium perovskites with 2D / 3D. However, due to the smaller and finer crystals, this could not be confirmed by SEM microscopy. The built solar cells showed almost no performance either when the annealing step was omitted nor annealed at a temperature of 100 °C. While germanium perovskite solar cells, both heated directly on a hot plate at 70 °C for 10 minutes, gave the best performance.

The germanium perovskite is very heat-sensitive and a negative influence on the material due to the heating of the halogen lamp was observed. The measured resistance showed that the glass substrate warmed to 29 °C at the start of the measurement and reached 42 °C after 100 minutes. Such heating of the germanium perovskite solar cell degrades the perovskite, and the solar cell stops working after a short time. If the light source were replaced and an LED lamp was used, it could be shown that the MPP tracking measurements showed an almost unchanged performance of the solar cell even after 90 minutes.

This work forms the basis for many possible ongoing and detailed studies for lead free germanium perovskite solar cells. Future work can be done in different directions. It is particularly important to further stabilize germanium perovskites and to improve their efficiencies. For this, the germanium perovskite layer could be produced with other techniques (such as vapor deposition) in order to obtain even better and homogeneous layers. Secondly, it would be of great importance for the photovoltaic community to better understand the aging process of germanium perovskite solar cells and thus improve their stability.

7 REFERENCES

[1]   https://data.giss.nasa.gov/gistemp/graphs/graph_data/Temperature_Anomalies_over_Land_and_over_Ocean/graph.pdf (accessed March 22nd, 2020).

[2]   IPCC (2007) climate change 2007: The physical science basis. IPCC working group I fourth assessment report: summary for policymakers, IPCC, Geneva, 2007, 5.

[3]   https://www.thomasnet.com/insights/imt/2012/05/07/the-damage-done-is-there-an-energy-future-that-doesnt-ruin-the-planet/ (accessed March 22nd, 2020).

[4]   H. Graßl, Klimawandel. Die wichtigsten Antworten. Freiburg im Breisgau, **2007**, *63*.

[5]   H. Washington, J. Cook, Climate Change Denial, Heads in the Sand, Earthscan **2011**, *34*.

[6]   IPCC. Global Warming of 1.5 ◦C: An IPCC Special Report on the Impacts of Global Warming of 1.5 ◦C Above Pre-Industrial Levels and Related Global Greenhouse Gas Emission Pathways, in the Context of Strengthening the Global Response to the Threat of Climate Change. Sustainable Development, and Efforts to Eradicate Poverty. Intergovernmental Panel on Climate Change, IPCC, 2018. Available online: https://www.ipcc.ch/sr15/download/ (accessed March 22nd, 2020).

[7]   https://citizensclimatelobby.uk/2019/03/the-hundred-tonne-diet/ (accessed March 22nd, 2020).

[8]   Lombardi, Pio & Arendarski, Bartlomiej & Suslov, Konstantin & Shamarova, Natalia & Sokolnikova, Polina & Pantaleo, Antonio & Komarnicki, P., A Net-Zero Energy System Solution for Russian Rural Communities. E3S Web of Conferences. 69. 01013. 10.1051/e3sconf/20186901013, 2018 (accessed March 22nd, 2020).

[9]   IEA. Solar Energy Perspectives. *OECD Publishing*, **2011**.

[10] IEA: Signs of stress must not be ignored, IEA warns in its new World Energy Outlook, Press Release, **2014** (accessed March 22nd, 2020).

[11] IAE *Key World Energy Statistics*, **2019**.

[12] Chinese PV producer Phono Solar to supply German system integrator Sybac Solar with 500 MW of PV modules. Solarserver.com, **2012** (accessed March 22nd, 2020).

[13] Solar PV Module Costs to Fall to 36 Cents per Watt by 2017. Greentechmedia.com, **2013** (accessed March 24, 2020).

[14] B. Beets, LCOE for Renewables Decreases, Fossil Fuels See Increase. Available online: https://www.pvmagazine.com/2015/10/06/lcoe-for-renewables-decreases-fossil-fuels-see-increase_100021404/ (accessed March 24, 2020).

[15] Global Wind and Solar Costs to Fall Even Faster, While Coal Fades Even in China and India. Available online: https://about.bnef.com/blog/global-wind-solar-costs-fall-even-faster-coal-fades-evenchina-india/ (accessed March 24, 2020).

[16] "Solar Photovoltaics Competing in the Energy Sector - On the road to competitiveness", European Photovoltaic Industry Association. **2011**, 18.

[17] https://www.wikiwand.com/en/Cost_of_electricity_by_source (accessed March 24, 2020).

[18] Fraunhofer Institute, Date between 2000-2010 by Navigant; Data from 2011 ff. IHS Markit; Graph: PSE GmbH **2018**.

[19] Q. Jiang, D. Rebollar, J. Gong, E.L. Piacentino, C. Zheng, T. Xu, *Angew. Chem. Int.* **2015**, *54*, 7617.

[20] K.-L. Hu, M. Kurmoo, Z. Wang, S. Gao, *Chem. Eur. J.* **2009**, *15*, 12050.

[21] A. H. Slavney, R. W. Smaha, I. C. Smith, A. Jaffe, D. Umeyama, H. I. Karunadasa, *Inorg. Chem.* **2017**, 56, 1, 46–55.

[22] V. M. Goldschmidt, Die Gesetze der Krystallochemie. In: Die Naturwissenschaften. Band 14, **1926**, 21, 477–485.

[23] D. B. Mitzi, D, B, S. Wang, C. A. Feild, C. A. Chess, A. M. Guloy, *A. M. Science* **1995**, *267*, 1473– 1476.

[24] J. Calabrese, N. L. Jones, R. L. Harlow, N. Herron, D. L. Thorn, Y. J. Wang, *Am. Chem. Soc.*, **1991**, *113*, 2328–2330.

[25] S. M. Wang, D. B. Mitzi, C. A. Field, A. J. Guloy, Am. Chem. Soc. **1995**, 117, 5297–5302.

[26] S. Shao, J. Liu, G. Portale, H. H. Fang, G. R. Blake, G. H. ten Brink, L. J. A. Koster, M. A. Loi, Adv. Energy Mater. **2018**, 8, 1702019 (1-10).

[27] A. Kojima, K. Teshima, Y. Shirai and T. Miyasaka, J. Am. Chem. Soc. **2009**, 131, 6050–6051.

[28] C. Wehrenfennig, M. Liu, H. J. Snaith et al., The journal of physical chemistry letters **2014**, 5, 1300.

[29] J. Albero, A. M. Asiri, H. García. Journal of Materials Chemistry **2016**, 4, 4353.

[30] W. Tress, Springer International Publishing **2016**, 53–77.

[31]   W. Shockley, Queisser, H. J. J. Appl. Phys. **1961**, 32, 510.

[32]   S. D. Stranks, G. E. Eperon, G. Grancini, C. Menelaou, M. J. P. Alcocer, T. Leijtens, L. M. Herz, A. Petrozza, H. J. Snaith, **2013**, 342-341.

[33]   Q. Dong, Y. Fang, Y. Shao, P. Mulligan, J. Qiu, L. Cao, J. Huang, **2015**, 347-967.

[34]   J.-H. Im, et al. Nanoscale **2011**, 3, 4088-4093.

[35]   H. S. Kim, C. R. Lee, J. H. Im, K. B. Lee, T. Moehl, A. Marchioro, S. J. Moon, R. Humphry-Baker, J. H. Yum, J. E. Moser, M. Graetzel N. G. Park, Sci. Rep. **2012**, 2, 591.

[36]   https://www.nrel.gov/pv/cell-efficiency.html (accessed March 25, 2020).

[37]   M.I. Asghar, J. Zhang, H. Wang, P.D. Lund, *Renew. Sust. Energ. Rev*. **2017**, *77*, 131.

[38]   J. Chen, N.-G. Park, *J. Phys. Chem. C*, **2018**, *25*, 14039–14063.

[39]   Y. Rong, Y. Hu, S. Ravishankar, H. Liu, X. Hou, Y. Sheng, A. Mei, Q. Wang, D. Li, M. Xu, J. Bisquert, H. Han, *Energy Environ. Sci.* **2017**, *10*, 2383.

[40]   G. A. Nemnes, C. Besleaga, V. Stancu, D. E. Dogaru, L. N. Leonat, L. Pintilie, K. Torfason, M. Ilkov, A. Manolescu, I. Pintilie, *J. Phys. Chem*. C **2017**, *121*, 11207.

[41]   W. Tress, N. Marinova, T. Moehl, S. M. Zakeeruddin, M. K. Nazeeruddin, M. Grätzel, *Energy Environ. Sci.* **2015**, *8*, 995.

[42]   B. Chen, M. Yang, S. Priya, K. Zhu, *J. Phys. Chem. Lett.* **2016**, *7*, 905.

[43]   A. Guerrero, A. Bou, G. Matt, O. Almora, T. Heumüller, G. Garcia-Belmonte, J. Bisquert, Y. Hou, C. Brabec, *Adv. Energy Mater.* **2018**, *8*, 1703376.

[44]   D. S. Albin, J. A. del Cueto, Proc. SPIE **2010**, *7773*, 77730N.

[45]   N.-G. Park, M. Grätzel, T. Miyasaka, K. Zhu, K. Emery, Nat. Energy **2016**, *1*, 16152.

[46]   H. J. Snaith, A. Abate, J. M. Ball, G. E. Eperon, T. Leijtens, N. K. Noel, S. D. Stranks, J. T.-W. Wang, K. Wojciechowski, W. Zhang, J. Phys. Chem. Lett. **2014**, *5*, 1511.

[47]   Y. Zhang, M. Liu, G. E. Eperon, T. C. Leijtens, D. McMeekin, M. Saliba, W. Zhang, M. de Bastiani, A. Petrozza, L. M. Herz, M. B. Johnston, H. Lin, H. J. Snaith, *Mater. Horiz.* **2015**, *2*, 315.

[48]   H. J. Snaith, A. Abate, J. M. Ball, G. E. Eperon, T. Leijtens, N. K. Noel, S. D. Stranks, J. T.-W. Wang, K. Wojciechowski, W. Zhang, *J. Phys. Chem. Lett*. **2014**, *5*, 1511.

[49]   Kang D, Park N, *Adv. Mater.* **2019**, *31* (34):1805214.

[50] National Renewable Energy Laboratory. Best research-cell efficiencies. https://www.nrel.gov/pv/assets/pdfs /pv-efficiency-chart.20181221.pdf. (accessed March 25, 2020).

[51] W. Ke, C. C. Stoumpos, M. G. Kanatzidis, Adv. Mater. **2018**, 1803230.

[52] L. Mao, C.C. Stoumpos, M. G. Kanatzidis, J. Am. Chem. Soc. **2019**, 141, 1171-1190.

[53] H. Tsai, Nature **2016**, 536, 312-316.

[54] A. Babayigit, A. Ethirajan, M. Muller, B. Conings, Nat. Mater. **2016**, 15, 247-251.

[55] E. T. McClure, M. R. Ball, W. Windl, P. M. Woodward, Chem. Mater. **2016**, 28, 1348-1354.

[56] S. F. Hoefler, G. Trimmel, T. Rath, Monatshefte für Chemie - Chem. Mon. **2017**, 148, 795-826.

[57] X. Wang, T. Zhang, Y. Lou, Y. Zhao, Mater. Chem. Front. **2019**, 3, 365-375.

[58] X. G. Zhao, J. H. Yang, Y. Fu, D. Yang, Q. Xu, L. Yu, S. H. Wie, L. Zhang, J. Am. Chem. Soc. **2017**, 139, 2630-2638.

[59] D. Yang, J.Lv, X.Zhao, Q. Xu, Y. Fu, Y. Zhan, A. Zunger and L. Zhang, Chem. Mater. **2017**, 29, 524-538.

[60] C. C. Stoumpos, C. D. Malliakas, M. G. Kanatzidis, Inorg. Chem. **2013**, 52, 9019.

[61] Z. Yang, A. Rajagopal, C. C. Chueh, S. B. Jo, B. Liu, T. Zhao, A. K. Jen, Adv. Mater. **2016**, 28, 8990.

[62]   F. Hao, C. C. Stoumpos, R. P. Chang, M. G. Kanatzidis, J. Am. Chem. Soc. **2014**, 136, 8094.

[63] S. Rühle, S. Solar Energy **2016**, 130, 139-147.

[64] N. K. Noel, S. D. Stranks, A. Abate, C. Wehrenfennig, S. Guarnera, A. A. Haghighirad, A. Sadhanala, G. E. Eperon, S. K. Pathak, M. B. Johnston, A. Petrozza, L. M. Herz, H. J. Snaith, Energy Environ Sci **2014**, 7, 3061.

[65] W. Ke, C. C. Stoumpos, I. Spanopoulos, L. Mao, M. Chen, M. R. Wasielewski, M. G. Kanatzidis, J. Am. Chem. Soc. **2017**, 139, 14800-14806.

[66] Z. Zhu, C. C. Chueh, N. Li, C. Mao, A. Jen, Adv. Mater. **2018**, 30, 1703800.

[67] K. Marshall, M. Walker, R.I. Walton, R. Hatton, Nat. Energy **2016**, 1, 16178.

[68] S. J. Lee, S. S. Shin, Y. C. Kim, D. Kim, T. K. Ahn, J. H. Noh, J. Seo, S. I. Seok, J. Am. Chem. Soc. **2016**, 138 (12), 3974-3977.

[69] M. H. Kumar, S. Dharani, W. L. Leong, P. P. Boix, R. R. Prabhakar, T. Baikie, C. Shi, H. Ding, R. Ramesh, M. Asta, M. Graetzel, S. G. Mhaisalkar, N. Mathews, *Adv. Mater.* **2014**, *26*, 7122-7127.

[70] F. Hao, C. C. Stoumpos, D. H. Cao, R. P. H. Chang, M. G. Kanatzidis, Nat. Photonics **2014**, 8, 489.

[71] J. Liu, M. Ozaki, S. Yakumaru, T. Handa, R. Nishikubo, Y. Kanemitsu, A. Saeki, Y. Murata, R. Murdey and A. Wakamiya, Angew. Chem., **2018**, 57, 13221-13225.

[72] Y. Liao, H. Liu, W. Zhou, D. Yang, Y. Shang, Z. Shi, B. Li, X. Jiang, L. Zhang, L. N. Quan, R. Quintero-Bermudez, B. R. Sutherland, Q. Mi, E. H. Sargent and Z. Ning, J. Am. Chem. Soc., **2017**, 139, 6693–6699.

[73] X Liu, Y. Wang, T. Wu *et al. Nat Commun* **2020**, *11***,** 2678.

[74] K. Nishimura, M. A. Kamarudin, D. Hirotani, K. Hamada K., Q. Shen, S. Iikubo, T. Minemoto, S. Hayase, **2020**, Nano Energy, *74*, 104858.

[75] J. M. Frost, K. T. Butler, F. Brivio, C. H. Hendon, M. van Schilfgaarde, A. Walsh, Nano Lett. **2014**, 14, 2584.

[76] A. Slikkerveer, F. A. Wolff, Med. Toxicol. Adverse Drug Exp. **1989**, 4, 303.

[77] L. A. Tillman, F. M. Drake, J. S. Dixon, J. R. Wood, Aliment. Pharmacol. Ther. **1996**, 10, 459.

[78] B.-W. Park, B. Philippe, X. Zhang, H. Rensmo, G. Boschloo, E. M. Johansson, *J. Adv. Mater.,* **2015**, *27*, 6806-6813.

[79] M. Lyu, J. H. Yun, M. Cai, Y. Jiao, P. V. Bernhardt, M. Zhang, Q. Wang, A. Du, H. Wang, G. Liu, L. Wang, *Nano Res.* **2016**, 9, 692-702.

[80] C. Ran, Z. Wu., J. Xi, F. Yuan, H. Dong, T. Lei, X. He, X. J. Hou, *Phys. Chem. Lett.* **2017**, 8, 394-400.

[81] B. W. Park, B. Philippe, X. Zhang, H. Rensmo, G. Boschloo and E. M. J. Johansson, *Adv. Mater.*, **2015**, 27, 6806-6813.

[82] E. Greul, M. L. Petrus, A. Binek, P. Docampo, T. Bein, *J. Mater. Chem.* A **2017**, 5, 19972.

[83] B. Fan, H. Yonghong, H. Yanqiang, Q. Ting, M. Xiaoliang, Z. Shufang, Solar Energy Materials and Solar Cells, **2018**, *184*, 15-21.

[84] C. C. Stoumpos, L. Frazer, D. J. Clark, Y. S. Kim, S. H. Rhim, A. J. Freeman, J. B. Ketterson, J. I. Jang, G. Kanatzidis, *J. Am. Chem. Soc*. **2015**, *137*, 6804-6819.

[85] P. P. Sun, Q. S. Li, L. N. Yang, Z. S. Li, *Nanoscale* **2016**, *8*, 1503-1512.

[86] W. Ming, H. Shi, M. H. Du, *J. Mater. Chem. A* **2016**, *4*, 13852-13858.

[87] A. Koliogiorgos, S. Baskoutas, I. Galanakis, *Comp. Mater. Sci.* **2017**, *138*, 92-98.

[88] I. Chung, J.-H. Song, J. Im, J. Androulakis, C. D. Malliakas, H. Li, A. J. Freeman, J. T. Kenney, M. G. Kanatzidis, *J. Am. Chem. Soc.* **2012**, *134,* 8579.

[89] T. Krishnamoorthy, H. Ding, C. Yan, W. L. Leong, T. Baikie, Z. Zhang, M. Sherburne, S. Li, M. Asta, N. Mathews, S. G. Mhaisalkar, *J. Mater. Chem. A* **2015**, *3*, 23829.

[90] T. Yokoyama, D. H. Cao, C. C. Stoumpos, T.-B. Song, Y. Sato, S. Aramaki, M. G. Kanatzidis, *J. Phys. Chem. Lett.* **2016**, *7*, 776.

[91] L. C. Tang, Y. C. Chang, J. Y. Huang, M. H. Lee, C. S. Chang, *Jpn J Appl Phys* **2009**, *48*, 112402.

[92] J. Qian, B. Xu, W. Tian, *Org Electron* **2016**, 37-61.

[93] G. Wang, D. Wang, X. Shi, *AIP Adv* **2015**, *5,*127224.

[94] L.-J. Chen, *RSC Adv.*, **2018**, *8*, 18396.

[95] S. Hayase, N. Ito, M. A. K. Kamarudin, Q. Shen, Y. Ogomi, S. Iikubo, K. Yoshino, T. Minemoto, and T. Toyoda, Proc. SPIE 10737, Organic, Hybrid, and Perovskite Photovoltaics XIX, 107371F, **2018**.

[96] P.-P. Sun, Q.-S.Li, L.-N. Yang, Z.-S. Li, J. Mater. Chem. **2014**, 2,303.

[97] X. Lu, Z. Zhao, K. Li, Z. Han, S. Wei, C. Guo, S. Zhou, Z. Wu, W. Guo, C. L. Wu, *RSC Adv*, **2016**, *6*, 86976.

[98] A. Kaltzoglou, M. Antoniadou, A. G. Kontos, C. C. Stoumpos, D. Perganti, E. Siranidi, V. Raptis, K. Trohidou, V. Psycharis, M. G. Kanatzidis, P. Falaras, *J. Phys. Chem. C.* **2016**, *120*, 11777.

[99] I. Kopacic, B. Friesenbichler, S. F. Hoefler, B. Kunert, H. Plank, T. Rath, G. Trimmel, *ACS Appl. Energy Mater.* **2018**, *1*, 343-347.

[100]L. Y. Huang, W. R. L. Lambrecht, *Phys. Rev. B. Condens Matter Mater Phys* **2016** *93*, 195211.

[101]M. Chen, M. Ju, H. F. Garces, et al. *Nat Commun* **2019**, *10*, 16.

[102]M. G. Ju, J. Dai, L. Ma, X. C. Zeng, *J. Am. Chem. Soc.* **2017**, *139*, 8038.

[103]C. Huang, X. C. Yan, G. Cui, Z. Liu, S. Pang, H. Xu, *CN Pat. App.* **2014**, CN 201410173750.

[104]Z. Song, et al. *Energy Environ. Sci.* **2017**, *10*, 1297-1305.

[105]G. Grancini, et al. *Nat. Commun.* **2017**, *8*, 15684.

[106] Y. G. Rong, et al. *Science 361*, **2018**, eaat8235.

[107] G. Niu, X. Guo, and L. Wang, *J. Mat. Chem. A*, **2015**, *17*, 8970-8980.

[108] A. Al Mamun, Y. Mohammed, T. T. Ava, G. Namkoong, and A. A. Elmustafa, *Mat. Lett.*, **2018**, *229*, 167-170.

[109] T. Ava, A. Al Mamun, S. Marsillac, and G. Namkoong, *App. Sci.*, **2019**, *9*, 188.

[110] Z. Messegee, A. Al Mamun, T. T. Ava, G. Namkoong, and T. M. Abdel-Fattah, *Mat. Lett.*, **2019**, *236*, 159-162.

[111] A. Rajagopal, K. Yao, A. K. - Y. Jen, Toward Perovskite Solar Cell Commercialization: A Perspective and Research Roadmap Based on Interfacial Engineering. Germany, **2018**.

[112] J. H. Noh, S. H. Im, J. H. Heo, T. N. Mandal, and S. I. Seok, *Nano Letters*, **2013**, *13*, 1764-1769.

[113] J. You, Y. Yang, Z. Hong, T.-B. Song, L. Meng, Y. Liu, C. Jiang, H. Zhou, W.-H. Chang, G. Li, and Y. Yang, *Applied Physics Letters*, **2014**, *105*, 183902.

[114] H. Zhou, Q. Chen, G. Li, S. Luo, T.-b. Song, H.-S. Duan, Z. Hong, J. You, Y. Liu, and Y. Yang, Interface engineering of highly e-cient perovskite solar cells. Science, 2014, 345, 542-546.

[115] G. E. Eperon, S. N. Habisreutinger, T. Leijtens, B. J. Bruijnaers, J. J., Franeker, D. W. DeQuilettes, S. Pathak, R. J. Sutton, G. Grancini, D. S. Ginger, R. A. J. Janssen, A. Petrozza, and H. J. Snaith, *ACS Nano*, **2015**, *9*, 9380-9393.

[116] G. Alagona, C. Ghio, and P. Kollman, *Journal of the American Chemical Society*, **1986**, *108*, 185-191.

[117] C.-G. Wu, C.-H. Chiang, Z.-L. Tseng, M. K. Nazeeruddin, A. Hagfeldt, and M. Grätzel, *Energy & Environmental Science*, **2015**, *8*, 2725-2733.

[118] A. M. A Leguy, Y. Hu, M. Campoy-Quiles, M. I. Alonso, O. J. Weber, P. Azarhoosh, M. Schilfgaarde, M. T. Weller, T. Bein, J. Nelson, P. Docampo and P. R. F.Barnes, *Chemistry of Materials*, **2015**, *27*, 3397-3407.

[119] J. Yang, B. D. Siempelkamp, D. Liu, and T. L. Kelly, *ACS Nano*, **2015**, *9*, 1955-1963.

[120] Z. Song, A. Abate, S. C. Watthage, G. K. Liyanage, A. B. Phillips, U. Steiner, M. Graetzel, and M. J. Heben, *Advanced Energy Materials*, **2016**, *6*, 1600846.

[121] N. Aristidou, I. Sanchez-Molina, T. Chotchuangchutchaval, M. Brown, L. Martinez, T. Rath, and S. A. Haque, *Angewandte Chemie International Edition*, **2015**, *54*, 8208-8212.

[122] D. Bryant, N. Aristidou, S. Pont, I. Sanchez-Molina, T. Chotchunangatchaval, S. Wheeler, J. R. Durrant, and S. A. Haque *Energy & Environmental Science*, **2016**, *9*, 1655-1660.

[123] N. Aristidou, C. Eames, I. Sanchez-Molina, X. Bu, J. Kosco, M. S. Islam, S. A. and Haque, *Nature Communications*, **2017**, *8*, 15218.

[124] A. Mei, X. Li, L. Liu, Z. Ku, T. Liu, Y. Rong, M. Xu, M. Hu, J. Chen, Y. Yang, M. Gratzel, and H. Han, *Science*, **2014**, *345*, 295-298.

[125] H. S. Kim, C. R. Lee, J. H. Im, K. B. Lee, T. Moehl, A. Marchioro, S. J. Moon, R. Humphry-Baker, R., J. H. Yum, J. E. Moser, M. Grätzel, M., and N. G. Park, *Scientific Reports*, **2012**, *2*.

[126] N. J. Jeon, N. J. et al. *Nature 517* **2015**, 476–480.

[127] J. W. Lee, et al. *Adv. Energy Mater.* **2015**, *5*, 1501310.

[128] M. Saliba, et al. *Energy Environ. Sci.* **2016**, 9, 1989–1997.

[129] F. Giustino, H. J. Snaith, *ACS Energy Lett.* **2016**, *1*, 1233-1240.

[130] Z. Zhao, F. Gu, Y. Li, W. Sun, S. Ye, H. Rao, Z. Liu, Z. Bian, C. Huang, *Adv. Sci.* **2017**, 1700204.

[131] M. G. Ju, J. Dai, L. Ma, X. C. Zeng, *J. Am. Chem. Soc.* **2017**, *139*, 8038-8043.

[132] U. Thakur, U. Kwon, M. M. Hasan, W. Yin, D. Kim, N. Y. Ha, S. Lee, T. K. Ahn, H. J. Park, *Sci. Rep.* **2016**, *6*, 35994.

[133] F. Hao, C. C. Stoumpos, D. H. Cao, R. P. H. Chang, M. G. Kanatzidis, *Nat. Photonics* **2014**, *8*, 489-494.

[134] J. H. Noh, S. H. Im, J. H. Heo, T. N. Mandal, S. I. Seok, *Nano Lett.* **2013**, *13*, 1764-1769.

[135] J. Yang, B. D. Siempelkamp, D. Liu, T. L. Kelly, *ACS Nano* **2015**, *9,* 1955−1963.

[136] Christians, J. A.; Miranda Herrera, P. A.; Kamat, P. V. J. Am. Chem. Soc. 2015, 137, 1530−1538.

[137] A. M. A. Leguy, Y. Hu, M. Campoy-Quiles, M. I. Alonso, O. J. Weber, P. Azarhoosh, M. Van Schilfgaarde, M. T. Weller, T. Bein, J. Nelson, P. Docampo, P. Barnes, R. F. *Chem. Mater.* **2015**, *27*, 3397−3407.

[138] L. Zhao, R. A. Kerner, Z. Xiao, Y. L. Lin, K. M. Lee, J. Schwartz, B. P. Rand, *ACS Energy Lett.* **2016**, 1, 595−602.

[139] Z. Liu, B. Sun, T. Shi, Z. Tang, G. Liao, *J. Mater. Chem. A* **2016**, *4*, 10700−10709.

[140] L. N. Quan, M. Yuan, R. Comin, O. Voznyy, E. M. Beauregard, S. Hoogland, A. Buin, A. R. Kirmani, K. Zhao, A. Amassian, D. H. Kim, E. H. Sargent, *J. Am. Chem. Soc.* **2016**, *138*, 2649−2655.

[141] D. H. Cao, C. C. Stoumpos, O. K. Farha, J. T. Hupp, M. G. Kanatzidis, *J. Am. Chem. Soc.* **2015**, *137*, 7843−7850.

[142] H. Tsai, W. Nie, J.-C. Blancon, C. C. Stoumpos, R. Asadpour, B. Harutyunyan, A. J. Neukirch, R. Verduzco, J. J. Crochet, S. Tretiak, *Nature* **2016**, *536*, 312−316.

[143] C. R. Kagan, D. B. Mitzi, C. D. Dimitrakopoulos, *Science* **1999**, *286*, 945−947.

[144] D. B. Mitzi, C. Feild, W. Harrison, A. Guloy, *Nature* **1994**, *369*, 467−469.

[145] S. Shao, J. Liu, G. Portale, H. H. Fang, G. R. Blake, G. H. Brink, L. J. A. Koster, M. A. Loi, *Adv. Energy Mater*, **2018**, *8*, 1702019.

[146] C. R. Kagan, D. B. Mitzi, C. D. Dimitrakopoulos, *Science*, **1999**, *286*, 945−947.

[147] K. Yao, X. Wang, F. Li, L. Zhou, *ChemComm*, *51,* **2015***, 15430–15433.

[148] D. H. Cao, C. C. Stoumpos, O. K. Farha, J. T. Hupp and M. G. Kanatzidis, *J. Am. Chem. Soc.*, **2015**, *137*, 7843.

8 APPENDIX

List of Publications

2019

Kopacic, Indira; Friesenbichler, Bastian; Höfler, Sebastian Franz; Rath, Thomas; Trimmel, Gregor. / **Structural, optical and electrical characterization of lead-free germanium halide perovskite solar cells**. Abstract from DocDays 2019, Graz, Austria.

Kopacic, Indira; Friesenbichler, Bastian; Höfler, Sebastian Franz; Rath, Thomas; Trimmel, Gregor. / **Structural, optical and electrical characterization of lead-free germanium halide perovskite solar cells**. Structural, optical and electrical characterization of lead-free germanium halide perovskite solar cells. 2019.

2018

Kopacic, Indira; Friesenbichler, Bastian; Höfler, Sebastian Franz; Kunert, Birgit; Plank, Harald; Rath, Thomas; Trimmel, Gregor. / **Enhanced Performance of Germanium Halide Perovskite Solar Cells through Compositional Engineering**. In: ACS Applied Energy Materials. 2018; Vol. 1, No. 2. pp. 343-347.

2017

Höfler, Sebastian Franz; Kopacic, Indira; Rath, Thomas; Fischer, Roland; Latal, Christine; Hippler, Dorothee; Trimmel, Gregor. / **Structural, optical and electrical characterization of solution-processable hybrid bismuth halide perovskite semiconductors**. Doc Days 2017: Book of Abstracts. 2017.

Höfler, Sebastian Franz; Kopacic, Indira; Rath, Thomas; Fischer, Roland; Latal, Christine; Trimmel, Gregor. / **Structural, Optical and Electrical Characterization of Solution-Processable Hybrid Bismuth Halide Perovskite Semiconductors**. Poster session presented at Doc Days 2017, Graz, Austria.

2016

Höfler, Sebastian Franz; Zahirovic, Indira; Rath, Thomas; Latal, Christine; Hippler, Dorothee; Trimmel, Gregor. / **Solution-Processed Bismuth(III)-Based Halide Perovskites as Absorber Materials for Photovoltaic Applications**. Poster session presented at International Conference on Hybrid and Organic Photovoltaics (HOPV16), Swansea, United Kingdom.

Zahirovic, Indira; Höfler, Sebastian Franz; Rath, Thomas; Buchmaier, Christine; Kunert, Birgit; Resel, Roland; Trimmel, Gregor. / **Influence of different annealing conditions in the preparation of metal halide perovskite films on their performance in solar cells**. Poster session presented at International Conference on Hybrid and Organic Photovoltaics (HOPV16), Swansea, United Kingdom.

Buchmaier, Christine; Zahirovic, Indira; Rath, Thomas; Kunert, Birgit; Resel, Roland; Trimmel, Gregor. / **Solution-processed Bi_2S_3 passivation layers for $CH_3NH_3PbX_3$ (X = Cl, Br, I) perovskite solar cells**. Poster session presented at International Conference on Hybrid and Organic Photovoltaics (HOPV16), Swansea, United Kingdom.

Höfler, Sebastian Franz; Zahirovic, Indira; Rath, Thomas; Latal, Christine; Hippler, Dorothee; Trimmel, Gregor. / **Fullerene-Based Passivation Layers in Solution-Processed Bismuth (III) Halide Perovskite Solar Cells**. European Materials Research Society (E-MRS) 2016 Fall Meeting, Warschau, Poland.

Zahirovic, Indira; Höfler, Sebastian Franz; Rath, Thomas; Kunert, Birgit; Resel, Roland; Trimmel, Gregor. / **Impact of different coating techniques and annealing conditions on the formation of metal halide perovskite films**. Poster session presented at European Materials Research Society (E-MRS) 2016 Fall Meeting, Warschau, Poland.

Höfler, Sebastian Franz; Zahirovic, Indira; Rath, Thomas; Latal, Christine; Hippler, Dorothee; Trimmel, Gregor. / **Hybrid Organic-Inorganic Bismuth (III) Halide Perovskites as Solution-Processed Absorber Materials for Photovoltaic Applications**. Poster session presented at Advanced Materials Day 2016, Graz, Austria.

Kopacic, Indira; Höfler, Sebastian Franz; Rath, Thomas; Kunert, Birgit; Resel, Roland; Trimmel, Gregor. / **Germanium (II) Iodide Perovskites as Solution-Processed Absorber Materials for Photovoltaic Applications**. Poster session presented at 14. Österreichische Photovoltaik-Tagung, Villach, Austria.

Höfler, Sebastian Franz; Kopacic, Indira; Rath, Thomas; Latal, Christine; Hippler, Dorothee; Trimmel, Gregor. / **Investigation of Hybrid Organic-Inorganic Bismuth Halide Perovskite Semiconductors for Photovoltaic Applications**. Poster session presented at 14. Österreichische Photovoltaik-Tagung, Villach, Austria.

2015

Buchmaier, Christine; Zahirovic, Indira; Rath, Thomas; Falk, Astrid; Reichmann, Angelika; Hofer, Ferdinand; Kunert, Birgit; Resel, Roland; Trimmel, Gregor. / **Impact of different alkali metal salts on morphological and structural properties of solution-processed Cu2ZnSnS4 thin films**. Poster session presented at 6th European Kesterite Workshop, Newcastle upon Tyne, UK.

Zahirovic, Indira; Buchmaier, Christine; Rath, Thomas; Falk, Astrid; Hofer, Ferdinand; Kunert, Birgit; Resel, Roland; Dimopoulos, Theodoros; Trimmel, Gregor. / **In-situ Dotierung von lösungsprozessierten Kesterit-Absorberschichten mit Alkalimetallen**. Poster session presented at 13. Österreichische Photovoltaik-Tagung, Schwaz, Österreich.

Zahirovic, Indira; Buchmaier, Christine; Rath, Thomas; Falk, Astrid; Reichmann, Angelika; Hofer, Ferdinand; Kunert, Birgit; Resel, Roland; Trimmel, Gregor. / **Investigation of the aging-process of the precursor solution for the solution-based preparation of kesterite absorbers**. Poster session presented at 6th European Kesterite Workshop, Newcastle upon Tyne, UK.

Buchmaier, Christine; Zahirovic, Indira; Rath, Thomas; Falk, Astrid; Reichmann, Angelika; Hofer, Ferdinand; Kunert, Birgit; Resel, Roland; Dimopoulos, Theodoros; Trimmel, Gregor. / **Optimierung und Charakterisierung von lösungsprozessierten Kesterit-Absorberschichten**. Poster session presented at 13. Österreichische Photovoltaik-Tagung, Schwaz, Österreich.

Curriculum Vitae

Name:	**Indira Kopacic**, MSc
Address:	Brucknerstrasse 74/3
	8010 Graz
	Austria
Mobile:	+43 680 2391722
E-mail:	indira.kopacic@gmail.com
Date of Birth:	18.09.1987

EDUCATION

02/2015 – 03/2020   **PhD Student**, TU Graz, Institute for Chemistry and Technology of Materials, Field of Research: New materials for lead-free perovskite solar cells (cooperating with Austrian Institute of Technology GmbH, the Joanneum Research Forschungsgesellschaft mbH, and the University of Patras)

10/2012 – 01/2015   **Master of Science** in Technical Chemistry, Graz University of Technology (in cooperation with the University of Graz as part of the NAWI-Graz program)

                                     Master's Thesis, TU Graz, Institute for Chemistry and Technology of Materials, Title: „Einfluss von Kobaltsalzen auf die Gummi-Messing Haftung sowie

deren thermische Alterung "(Prof. Gregor Trimmel)

10/2007 – 10/2012	**Bachelor of Science in Chemistry**, Graz University of Technology (in cooperation with the University of Graz as part of the NAWI-Graz program)

Bachelor's Thesis, TU Graz, Institute for Chemistry and Technology of Materials, Title: "Keramische Temperatursensoren NTC-Heißleiter" (Prof. Klaus Reichmann)

WORK EXPERIENCE

03/2019 – 02/2020	**PhD Project-Assistant**, cooperating with Austrian Institute of Technology GmbH, the Joanneum Research Forschungsgesellschaft mbH, and the University of Patras.
10/2017 – 02/2019	Maternity leave
02/2015 – 10/2017	**PhD Project-Assistant**, TU Graz, Institute for Chemistry and Technology of Materials, Topic of Research „Lead-free perovskite solar cells" (Prof. Gregor Trimmel)
04/2014 – 11/2014	**Semperit AG und Polymer Competence Center GmbH**, *Leoben*, Austria **Junior Researcher**, Topic of Research „Development and optimization of the adhesion processes / Rubber-metal adhesion "

09/2010 – 10/2010	**ACIB (Austrian Centre of Industrial Biotechnology)**, *Graz*, Austria
	Junior Researcher, Topic of Research "Synthesis of new active substances (organic chemistry)"

PUBLICATIONS

See APPENDIX (List of Publications)

ADDITIONAL INFORMATION

Workshops/Seminars:	Conflict Management
	Social Competences for Study Assistants
	Microscopy Training
Languages:	German (2. mother-tongue)
	Bosnian-Croatian-Serbian (mother-tongue)
	Slovenian
	English
IT- Skills:	MS Office, Origin, Sci-Finder, SciDex CLAKS, Chem-Draw